

Reduced order wind turbine aeroelastic modelling for condition monitoring & fault detection

Naunidh Singh Mangat



Reduced order wind turbine aeroelastic modelling for condition monitoring & fault detection

by

Naunidh Singh Mangat

in partial fulfillment of the requirements for the degree of Master of Science in Sustainable Energy
Technology at the Delft University of Technology

to be defended publicly on Wednesday February 27, 2019 at 10:00 AM.

Student number:	4623983	
Project duration:	Feb 15, 2018 – Feb 27, 2019	
Thesis committee:	Prof.dr. Simon Watson,	TU Delft, Chair
	Dr.ir. Jessica G. Holierhoek,	TU Delft, Supervisor
	Dr.ir. Alexander van Zuijlen,	TU Delft
	Dr.ir. Fanzhong Meng,	DTU/Fraunhofer IWES, Supervisor

An electronic version of this thesis is available at <http://repository.tudelft.nl/>.

Acknowledgement

Looking back at my journey working on this thesis project there are many people to thank and acknowledge. First and foremost I would like to thank Fanzhong Meng, my supervisor at Fraunhofer IWES, for showing faith in me and giving me the opportunity to work on this thesis project at Fraunhofer IWES. I thank him for being extremely understanding and appreciate the great amount of time he dedicated either holding technical discussions with me or reading through my codes. I am very grateful to Jessica Holierhoek, my supervisor in Delft, for being super-patient, and for always being there when I needed her help. Her technical insights into this challenging topic were instrumental at moments when I was stuck and running out of ideas. I am also very grateful to Karl Merz who was kind enough to provide the code used in this thesis, and was forever reachable to answer any questions I had.

During this thesis project I suffered the irreparable personal loss of my beloved father. Though he did not live to read this but I cannot thank him enough for being such a supportive dad and for the encouragement he gave me to pursue my passion at TU Delft. Then I must thank my fellow companions and former colleagues at IWES Fraunhofer, Shoaib and Shobhit, first for helping me adapt to life in Germany but also for their moral support in coping with this dark phase in my life. Finally, I wish to express love and gratitude for my mother who provided me that motivation to carry on when I felt all was lost.

*Naunidh Singh Mangat
Delft, February 2019*

Contents

List of Figures	xi
List of Tables	xiii
List of Symbols	xv
1 Introduction	1
1.1 Maintenance strategies for wind turbines	1
1.2 Need for reduced-order aeroelastic model	2
1.3 Report outline.	3
2 Background	5
2.1 Aeroelasticity	5
2.2 Dynamic systems	6
2.2.1 Feedback loop	7
2.2.2 Modelling of dynamic systems	7
2.3 Aerodynamics.	9
2.3.1 1-D Momentum Theory	9
2.3.2 2-D Blade Element Method	11
2.3.3 Blade Element Momentum (BEM)	12
2.3.4 Unsteady BEM	13
2.3.5 Vortex wake models	15
2.3.6 Computational Fluid Dynamics (CFD).	17
2.4 Structural Dynamics	17
2.4.1 Lagrange's Method	18
2.4.2 Structural models	18
2.4.3 Modal reduction technique : Craig-Bampton Method	20
2.4.4 Representation of rotations	21
2.5 State-of-the-art aeroelastic codes	24

3	Description of model	27
3.1	Limitations of state-of-the-art aeroelastic models.	27
3.2	Desired model characteristics.	28
3.3	Model selection	28
3.4	Structural Dynamics	29
3.4.1	Notation and coordinate system	29
3.4.2	Non-linear finite element representation	31
3.4.3	Non-Linear Equations of Motion.	37
3.4.4	Implementation of Constraints	40
3.4.5	Linearization of structural model	42
3.4.6	Modal reduction	44
3.5	Aerodynamics.	45
3.5.1	Coordinate system	45
3.5.2	Non-linear aerodynamics	46
3.5.3	Linearized aerodynamic model	48
3.5.4	Modal reduction of aerodynamic states	54
3.5.5	Aerodynamic state space.	54
3.6	Coupled aeroelastic equations	54
4	Verification of linearization	57
4.1	Methodology	57
4.1.1	Steady state point	57
4.1.2	Linearization.	59
4.1.3	Eigenvalue analysis	60
4.2	Parked wind turbine	60
4.2.1	Body modes	60
4.2.2	Full system modes	63
4.3	Campbell diagram	64
4.4	Aeroelastic damping	66
4.5	Modal reduction study	68
4.6	Stability analysis	72

5 Time marching simulation tool	75
5.1 Introduction	75
5.2 Methodology	76
5.3 Verification of time marching tool.	77
6 Conclusions & Recommendations	81
6.1 Conclusion	81
6.2 Recommendations	82
Bibliography	83

Abstract

Wind energy has emerged as a promising alternative to fossil fuel energy sources over the last two decades partly due to considerable reductions in the cost of power production. A common trend towards cost reduction has been to build larger and lighter wind turbines. These produce more power per unit and use less material. Another strategy for cost reduction could be to reduce the Operations & Maintenance (O&M) costs of wind turbines by using optimal O&M strategies. O&M costs account for approximately one-fourth of the overall energy cost for the full lifetime of a wind turbine. They assume even greater significance in the wake of growing interest in offshore wind farms since offshore wind turbines operate in harsher environments compared to their onshore counterparts and are more difficult to access.

Condition monitoring has been proposed as a novel preventive maintenance strategy wherein sensors are employed to collect data related to the functioning of an operational wind turbine. This data can be processed to get meaningful information about component health of the wind turbine. An aeroelastic model can be used to simulate the fault-free response of the wind turbine for given operating conditions. By comparing real-time information from the condition monitoring system and aeroelastic model, it may be possible to develop routines which can detect developing faults in the wind turbine components. This forms the basis of a model-based condition monitoring system (MODCMS).

For purposes of model-based condition monitoring it is required to have an aeroelastic model which is computationally fast to be capable of running real-time aeroelastic load simulations, and is highly accurate in order to detect faults. Furthermore, it is also desirable to have a linear aeroelastic model since this can also be used for controller and state observer design. A state observer can help estimate states of the wind turbine which are not easily measurable. This thesis reviews state-of-the-art aeroelastic tools to get a better understanding of their limitations. A reduced-order aeroelastic model is developed using the aeroelastic module in STAS WPP (State Space Analysis of Wind Power Plants) which is an open-source aero-hydro-servo-elastic tool in the Matlab/Octave environment. The linear reduced order aeroelastic model is verified by running test cases in the frequency domain for the NREL 5MW Baseline wind turbine. The accuracy of the linearized model is demonstrated by performing a stability analysis study for the NREL 5MW Baseline wind turbine.

Furthermore, different coupling and numerical integration schemes are studied to develop a time marching simulation tool. Two main approaches are proposed. The first involves time marching of the monolithic, strongly coupled non-linear aeroelastic model using a multistep predictor-corrector integration scheme. In the second approach, a partitioned, loosely coupled version of the linear aeroelastic model is implicitly integrated over time. In the present work a tool based on the first approach of integrating the non-linear aeroelastic model is developed and subsequently verified by running simple power production test cases.

In conclusion, this thesis discusses and implements a framework of strategies which can be implemented to reduce the order of a high-order aeroelastic model. It suggests coupling and numerical integration schemes to utilize this reduced-order model in a time marching simulation tool.

List of Figures

1.1	The flow diagram of a model based condition monitoring system. Adapted from [14].	2
2.2	Representation of aeroelastic system as a feedback system	7
2.3	Representation of actuator disk model. Adapted from [10].	10
2.4	Spanwise variation of power extraction with and without tip loss for a blade with uniform circulation on a three bladed turbine operating at a tip speed ratio of six. Adapted from [10].	13
2.5	Airfoil coordinate system	14
3.1	Skeletal sketch of general wind turbine system modelled in STAS Aeroelastic [46]. Note only one blade has been shown here.	29
3.2	Coordinate systems used in the wind turbine model of STAS Aeroelastic [48]. Structure is modelled as finite elements, and dots represent nodes. Note that white dots represent joints.	30
3.3	Illustration of deformed beam element with respect to undeformed orientation (dashed line). Adapted from [48].	35
4.1	1st tower side-to-side mode shape for NREL 5MW Baseline turbine	61
4.2	2nd tower side-to-side mode shapes for NREL 5MW Baseline turbine	61
4.3	1st fore-aft mode shape for NREL 5MW Baseline turbine	61
4.4	2nd tower fore-aft mode shape for NREL 5MW Baseline turbine	61
4.5	1st blade flapwise mode shape for NREL 5MW Baseline turbine	62
4.6	2nd blade flapwise mode shape for NREL 5MW Baseline turbine	62
4.7	1st blade edgewise mode shape for NREL 5MW Baseline turbine	62
4.8	2nd blade edgewise mode shape for NREL 5MW Baseline turbine	62
4.9	1st blade torsional mode shape for NREL 5MW Baseline turbine	63
4.10	Campbell diagram for NREL 5MW turbine using STAS Aeroelastic	65
4.11	Campbell diagram for NREL 5MW turbine using FAST v8.16	65
4.12	Tower fore-aft deflection for NREL 5MW Baseline turbine at 8m/s	70
4.13	Tower lateral deflections for NREL 5MW Baseline turbine at 8m/s	70
4.14	Blade flapwise deflections for NREL 5MW Baseline turbine at 8m/s	71

4.15	Blade edgewise deflections for NREL 5MW Baseline turbine at 8m/s	71
4.16	Natural frequency of modes relevant for stability analysis of NREL 5MW Baseline wind turbine .	73
4.17	Damping ratio of modes relevant for stability analysis of NREL 5MW Baseline wind turbine . . .	73
5.1	Comparison of time series for blade tip deflection in flapwise direction of NREL 5MW Baseline wind turbine at $V_\infty = 8\text{m/s}$	77
5.2	Comparison of time series for blade tip deflection in edgewise direction of NREL 5MW Baseline wind turbine at $V_\infty = 8\text{m/s}$	78

List of Tables

4.1	Natural frequencies of body modes (in Hz)	63
4.2	Natural frequencies (in Hz) of full wind turbine model	64
4.3	Comparison of centrifugal stiffening : Increase in natural frequency (Ω varies from 0 to 20 rpm).	66
4.4	Structural damping ratio of system modes	67
4.5	Aeroelastic damping ratio of system modes	67
4.6	Convergency analysis for blade structural modes	69
4.7	Overview of reduced model	69
4.8	Operating points for instability analysis [38]	72
5.1	Comparison of time marching results	78

List of Symbols

x	State vector	
y	Output vector	
u	Input vector	
m_e	Element mass matrix	
c_e	Element damping matrix	
k_e	Element stiffness matrix	
M	Global mass matrix	
C	Global damping matrix	
K	Global stiffness matrix	
F	Force vector	
q	Generalized degrees of freedom	
q̂	Retained degrees of freedom	
q_s	Slave degrees of freedom	
w	Vector of structural velocities of element	
<i>a</i>	Axial induction factor	[-]
<i>a'</i>	Tangential induction factor	[-]
<i>c</i>	Chord length	[m]
<i>f</i>	Prandtl tip-root loss correction factor	[-]
<i>a₁, a₂</i>	Circulation lag parameters	[-]
<i>A_r</i>	Area of rotor disk	[m ²]
<i>V_∞</i>	Freestream wind velocity	[ms ⁻¹]
<i>V_w</i>	Wind flow velocity far downstream	[ms ⁻¹]
<i>V_r</i>	Wind flow velocity at rotor	[ms ⁻¹]
<i>C_p</i>	Power coefficient	[-]
<i>C_T</i>	Thrust coefficient	[-]
<i>Q</i>	Torque	[Nm]
<i>T</i>	Thrust force	[N]
<i>W</i>	Relative flow velocity	[ms ⁻¹]
<i>L</i>	Lift force	[N]
<i>D</i>	Drag force	[N]
<i>R</i>	Rotor radius	[m]
<i>B</i>	Number of rotor blades	[-]
<i>U</i>	Local flow velocity	[ms ⁻¹]
<i>V_{i,q}</i>	Quasi-steady induced velocity	[ms ⁻¹]
<i>V_i</i>	Induced velocity corrected for dynamic inflow	[ms ⁻¹]
<i>Ŷ_i</i>	Intermediate variable in dynamic inflow model	[ms ⁻¹]
<i>C_l</i>	Lift coefficient	[-]
<i>C_d</i>	Drag coefficient	[-]
<i>C_m</i>	Moment coefficient	[-]
<i>E_K</i>	Kinetic energy	[J]
<i>E_P</i>	Potential energy	[J]
<i>E</i>	Young's modulus of Elasticity	[Nm ⁻²]
<i>N</i>	Rotor speed in rpm	[s ⁻¹]

η	Modal degree of freedom	
Φ	Shape matrix	
θ	Vector of exponential map parameters for elastic rotations at nodes	
ζ	Vector of elastic rotations at nodes	
ξ	Vector of exponential map parameters for undeformed orientations of beam sections at nodes	
ϕ	Inflow angle	[rad]
ϕ_c	Cone angle	[rad]
χ	Yaw angle	[rad]
δ	Driveshaft tilt angle	[rad]
α	Dynamic angle of attack	[rad]
α_q	Quasi-steady angle of attack	[rad]
α_z	Zero lift angle of attack	[rad]
τ_1, τ_2	Time constants in dynamic inflow model	[s]
τ	Dynamic stall model time constant	[s]
ρ	Air density	[kgm ⁻³]
β	Blade pitch angle	[rad]
ξ_a	Aerodynamic twist angle	[rad]
σ	Stress	[Nm ⁻²]
ζ_d	Rayleigh damping parameter	[-]
ϵ	Strain	[-]
Ψ	Blade azimuthal angle	[rad]
Γ	Circulation	[m ² s ⁻²]
Ω	Rotor speed	[rads ⁻¹]

Introduction

Over the last two decades, wind energy has emerged as a promising alternative to conventional power generation technologies based on fossil fuels. In 2001, the world had a cumulative installed wind capacity of 23.9 GW [25]. Due to exponential growth in the intervening period, the total installed wind capacity as of 2017 has reached 539.5 GW [25]. This growth has been made possible through a continuous reduction in the cost of electricity production from wind. For wind turbines, almost 70-75% of the total energy production cost is incurred upfront as capital cost [22]. For a 20 year lifetime, Operation and Maintenance (O&M) costs account for 25-30% of the overall energy generation cost [22]. One trend towards cost reduction has been to build larger and lighter wind turbines. These produce more power per unit and use less material. This in turn means designers must account for larger deflections of turbine blades for instance. Another strategy to further reduce the cost of wind energy is to bring down the O&M costs of wind turbines through optimal O&M strategies. The latter method assumes even greater significance in the wake of growing interest in offshore wind energy. Offshore wind turbines operate in harsher conditions compared to their onshore counterparts, and at the same time are more difficult to access. Both of these factors are expected to push up the O&M costs of offshore wind turbines in comparison to onshore wind turbines. As turbines grow in size, analysis of turbine data by Tavner et al. has shown that larger turbines in fact are more likely to fail and thus need more maintenance operations [63].

Development of a reduced-order aeroelastic model for one such novel O & M strategy, model based condition monitoring systems (MODCMS), is the broad motivation behind this thesis. This thesis project forms part of ongoing research into MODCMS at the Fraunhofer Institute for Wind Energy Systems (Fraunhofer IWES).

This chapter starts with a brief overview of different maintenance strategies and arrives at the idea behind condition monitoring systems (CMS). This is followed by a brief discussion on the motivation to develop a reduced-order aeroelastic model. The chapter concludes with an overview of the report structure.

1.1. Maintenance strategies for wind turbines

The main objective of any maintenance operation on a wind turbine is to ensure that the system components perform their intended functions properly with high reliability. The maintenance strategy aims to minimize downtime in case of a breakdown and ensure maximum availability of the wind turbine. In general, all wind turbine maintenance strategies fall into two main categories: corrective and preventive maintenance [22]. Under corrective maintenance, repair or replacement of components is conducted only in the event of occurrence of a fault or component failure [22]. This type of maintenance strategy is unscheduled and leads to long downtimes since machinery and personnel need to be deployed at short notice or even worse orders need to be placed to purchase components which are not readily available. Research has shown that this maintenance strategy is easily the most expensive one [22]. The other option is to go for a corrective main-

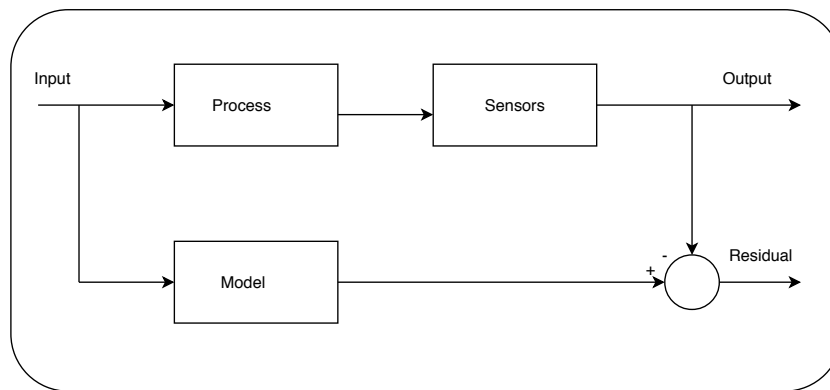


Figure 1.1: The flow diagram of a model based condition monitoring system. Adapted from [14].

tenance strategy wherein the objective is to repair or replace components before they fail [22]. One form of preventive maintenance is scheduled maintenance in which inspection of the wind turbine and replacement of components is carried out at regular intervals of time [22]. Thus, this type of maintenance is planned but the disadvantage is that maintenance may be carried out more frequently than is necessary and components may be replaced before they have served their full life [22]. Preventive maintenance is not fully optimized and thus there is scope for improvement.

To mitigate the problems related to corrective and preventive maintenance, condition based monitoring (CMS) has been proposed as a preventive maintenance strategy. Under this strategy, continuous monitoring and inspection techniques look for signs of faults and component failure [22]. Sensors are employed to collect data related to the functioning of the wind turbine. Monitoring can either be online or offline. With online monitoring, instantaneous feedback is available and this necessarily requires fast and efficient data handling and storage techniques. Offline monitoring on the other hand entails collection of data after regular time intervals. Consequently, there's a greater chance of missing out on detection of faults in time for optimal planning of maintenance actions. Several monitoring techniques such as vibration analysis, acoustic emissions, strain measurement, ultrasonic testing, oil analysis, electrical effects etc. are available [22]. The data obtained is then processed to get a meaningful measure of component health which is further used to detect and diagnose faults [50]. Based on the prognosis of the fault, maintenance action is accordingly planned. In this way, possible failures can be detected well in advance and maintenance costs can be lowered. This is an optimal way of carrying out maintenance, and O&M costs are expected to be lower in the long-run.

The fundamental idea behind CMS is to detect deviations from the normal operating behaviour of a wind turbine and indicate developing faults [13]. For this purpose, it is required to develop an accurate model which simulates the fault-free response of a wind turbine based on the given input conditions. One way of doing this is to use the data obtained at different input conditions from the monitoring systems on the turbine to develop models of processes taking place in the various components of the wind turbine. This can be done by acquiring data from a supervisory control and data acquisition (SCADA) system [14]. The other possibility is to develop a model of the wind turbine which is based on physical laws [14]. This is the fundamental approach in model-based condition monitoring systems (MODCMS). Such models contribute to a better understanding of functioning of wind turbine components and can also be used for design improvements but they are also known to be more computationally expensive. Fig. 1.1 gives a nice overview of MODCMS as described in this section.

1.2. Need for reduced-order aeroelastic model

An aeroelastic model is central to the idea of model-based condition monitoring. For one, the aeroelastic model can be used to design a state observer and controller for the wind turbine. This is important because not all states of the wind turbine are easy to measure. While the aeroelastic model can be used to design a controller for a wind turbine, the same controller can also be used in combination with the aeroelastic model to simulate the response of the wind turbine precisely. When online condition monitoring is applied, the

state observer and/or sensors provide the state of the operational wind turbine in real time. Now, the state of the operational turbine might be different from the expected fault-free state of the system for a given set of operating conditions. This is borne out by an aeroelastic model coupled with a controller which gives us the expected fault-free state of the wind turbine system. Comparison of the fault-free and real states of the system gives us a qualitative and quantitative indication of a developing fault.

Condition based monitoring applications require an aeroelastic model which is accurate, such that errors arising from modelling are minimized, as well as precise. In addition, it is essential for the aeroelastic model to simulate the state of the system and the relevant outputs in real time. This is necessary for making real-time comparisons with condition monitoring data from an operational wind turbine. While aeroelastic tools which can run time marching simulations in real time are available, they may be a bit simplified and do not capture structural or aerodynamic details essential for fault detection applications. In addition, these aeroelastic models are usually hard to comprehend which makes it difficult for users to implement changes in these models. In this context, it is desired to have an in-house aeroelastic tool for the Fraunhofer IWES which is easy to understand and adaptable according to the needs of the user.

Reduced-order aeroelastic models offer the promise of carrying out time domain simulations of wind turbine operations in real time for condition monitoring and fault detection. Besides this, such a reduced-order aeroelastic model can have several auxiliary applications. It can be used for 'Hardware in the Loop' tests whereby it can simulate the rotor and provide real time feedback to the component being tested such as the nacelle or tower. An aeroelastic model in Matlab environment would be an added advantage as it can easily be integrated with the test facility hardware at Fraunhofer IWES.

This leads to the objective of this Master thesis project:

To develop and verify a computationally efficient, accurate and stable reduced-order aeroelastic model for a wind turbine and demonstrate its capability for the specific application of model based condition monitoring and fault detection.

1.3. Report outline

This report is organized such that chapters build on previous knowledge to systematically drive towards achieving the main research objective. In Chapter 2, an extensive survey of the literature is carried out to give a background into various aspects of aerodynamic and structural dynamics modelling relevant to aeroelasticity. This chapter concludes with an overview of state-of-the-art aeroelastic tools. Chapter 3 builds upon the limitations of state-of-the-art aeroelastic tools to formulate a set of desired characteristics for a reduced-order aeroelastic model relevant to condition monitoring and fault detection. It then goes on to describe in some detail the aeroelastic tool developed in this thesis. The aerodynamics and structural dynamics are described separately. For both, first the non-linear model is described followed by the linearization. Chapter 4 describes the results of case studies performed in the frequency domain to verify the linearized aeroelastic model described in Chapter 3. It concludes with a stability analysis study to demonstrate that an accurate linearization has been achieved. In Chapter 5 a time marching aeroelastic simulation tool is developed. This chapter describes the procedure followed in developing such a tool and then goes on to discuss results for verification studies performed on this tool. Finally, this thesis concludes with a chapter summarizing the main conclusions of this thesis project, and provides some recommendations for future course of work.

2

Background

This chapter begins by giving a basic overview of aeroelasticity. It then moves on to briefly describe dynamic systems in general, and modelling approaches for dynamic systems. The main aim in doing this is to point out system characteristics and modelling approaches for dynamical systems which are relevant to aeroelastic modelling. The rest of the chapter is divided between aerodynamic and structural dynamic modelling of wind turbines. Under aerodynamics, the various aerodynamic modelling approaches for wind turbines are described, and their limitations pointed out. For the structural dynamics, a method to derive the non-linear equations of motion is first described. This is followed by a discussion of the various structural dynamics models applicable to wind turbines. The section on Craig-Bampton method gives an overview into how large finite element systems can be assembled and represented in terms of their modes. The different methods available in multibody dynamics for representation of rotations are also discussed as this information would be necessary later while describing the aeroelastic model in Chapter 3. Finally, the chapter concludes with an overview of the features of some state-of-the-art aeroelastic codes. Note that bold symbols are used to represent vectors and matrices in this chapter.

2.1. Aeroelasticity

The field of aeroelasticity originates from the interaction between aerodynamic flows, elastic structures and dynamic forces. Consider the simple case of the flexible wing of an aircraft. The aerodynamic forces on an airfoil of the wing are a dynamic function of the angle of attack. The angle of attack in turn is determined by the relative wind velocity perceived by the airfoil, aerodynamic twist and pitch angle of wing. Structural deformations such as torsional rotations will change the angle of attack. Similarly, longitudinal or lateral vibrations induced in the wing will also change the angle of attack by altering the perceived wind velocity. The aerodynamic forces on the wing are thus a function of structural deformations and velocities, and in turn the structural motion of the wing itself is a function of the aerodynamic forces. This is the type of fluid-structure interaction which forms the basis of aeroelasticity.

On a fundamental level, an aeroelastic analysis must consider three interlinked forces - aerodynamic, inertial and elastic forces. However, modern aeroelastic analysis can also include additional couplings besides these three forces in the form of hydrodynamic forces, thermal coupling and advanced controllers [32]. The resultant interdependencies are shown in Friedmann's Hexahedron in Fig. 2.1. These couplings lead to unexpected system behaviours and some interesting phenomena which can even cause the system to become unstable and fail. A simple example of instability due to the interaction between elastic and aerodynamic forces is the classical flutter instability of a wing leading to self-sustaining oscillations and ultimate destruction of the wing. The reason being that at a specific range of operating conditions, known as the flutter boundary, the aerodynamic forces and the structural motion of the wing interact such that during a cycle of oscillation net positive work is done on the wing by the aerodynamic forces. As a result, energy is continuously added to

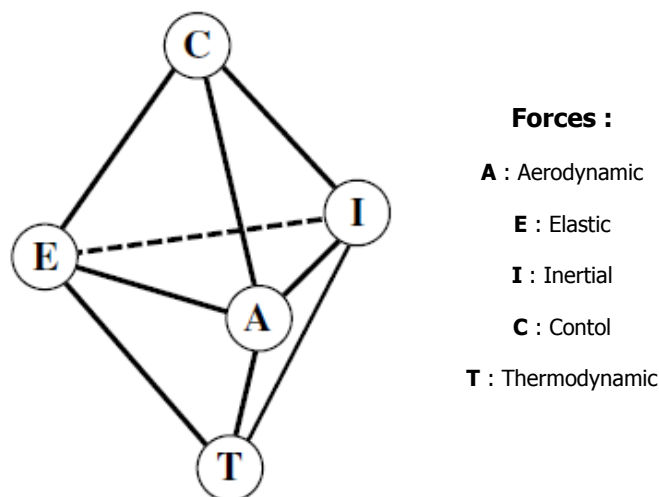


Figure 2.1: Friedmann's Hexahedron showing different possible couplings in an aeroelastic system [32]

the system and amplitude of oscillations exponentially increases leading to failure [32].

The wide range of problems to which aeroelastic analysis can be applied are broadly divided into two categories. The first are instability boundary problems in which the task is to determine the boundary at which a stable fluid-structure interaction becomes unstable. The other set of problems are called response problems where the aim of the aeroelastic analysis is to calculate the static or dynamic response of a system to a given excitation [32].

In the context of wind turbines, aeroelasticity is very important. Aeroelastic interactions must be included to accurately predict loads for designing wind turbines. For performance optimization and load alleviation, wind turbines have controllers, and these controllers can be designed using linear aeroelastic models. Traditionally, wind turbine design has involved mitigating loads with specific focus on fracture and fatigue failure. In recent times, there is an increasing trend towards larger and more flexible blades. Larger blades due to economies of scale, and flexible blades that use less material and hence reduce cost. A consequence of both these trends is increasing fluid-structure interactions, some of which were hitherto never observed on wind turbines while others were known but were not given due importance in the design process. These may lead to aeroelastic instabilities at certain ranges of operating conditions which can cause ultimate failure due to exponential growth of vibrations or fatigue failure due to limit cycle oscillations. Another possible application of aeroelasticity in wind turbines is for active load control in blades made up of advanced materials. A good example is materials with bending-torsion coupling which can help alleviate blade loads.

2.2. Dynamic systems

This section gives an overview of dynamic systems in the context of aeroelasticity. It attempts to explain how important characteristics of dynamic systems shape modelling approaches.

A dynamic system is any system whose response is time dependent [5]. In other words, the system does not instantaneously respond to an applied input, but in fact there is a time lag between the application of input and the attainment of a new steady state. An example of this is the dynamic inflow effect wherein the inflow velocity at an airfoil section does not immediately adjust to a sudden pitching motion or step change in freestream wind velocity.

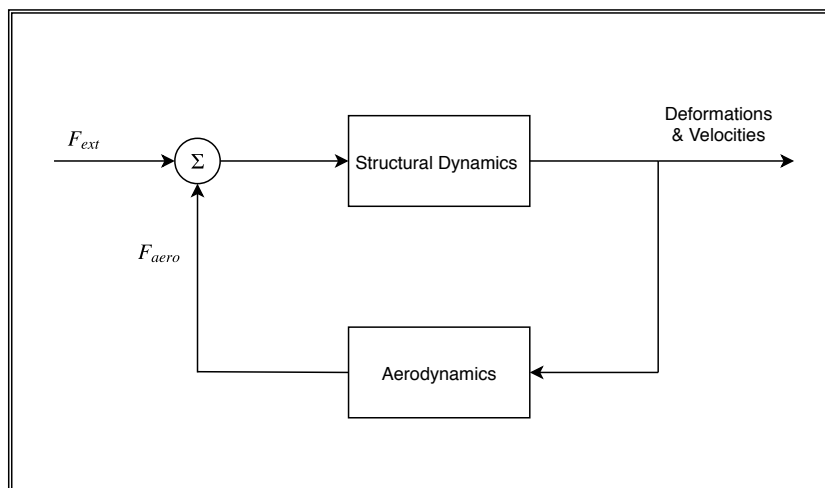


Figure 2.2: Representation of aeroelastic system as a feedback system

2.2.1. Feedback loop

Consider two (or more) dynamical systems which are connected together such that each system can influence the other and their dynamics are strongly coupled. This phenomena is called feedback [5]. Furthermore if the systems are connected in a cycle it is referred to as a closed feedback loop. An aeroelastic system is a classic example of a closed feedback loop if we were to consider the aerodynamic, elastic and inertial forces as representing three different sub-systems. Aström & Murray [5] have stated that such systems are not amenable to simple cause and effect reasoning, and as such we must resort to more formal mathematical methods to understand their behaviour.

Feedback systems have some important properties which are very relevant to aeroelastic modelling of wind turbine systems. Firstly, a set of non-linear components connected together in a feedback loop may actually cause the system to behave linearly [5]. This is counter-intuitive but is very useful in practice because one can design a control system for a wind turbine by using a simple linear aeroelastic model. Secondly, a closed loop feedback system is said to be less sensitive to external disturbances and to variations in properties of individual sub-systems as compared to individual sub-systems themselves [5]. This is clearly advantageous in the sense that low fidelity models can be applied to such systems or in cases when system properties are not precisely known. Lastly, feedback systems may also become dynamically unstable and show runaway behaviour at specific operating conditions [5]. This characteristic points to the possibility of aeroelastic instabilities in wind turbines which was briefly referred to in Section 2.1.

2.2.2. Modelling of dynamic systems

A model is defined as a mathematical representation of a system's dynamic behaviour based either on physical laws governing the system or experimental data [5]. It allows us to make predictions about the future behaviour of systems. In the context of a mechanical system, this has historically involved describing the behaviour of the system in terms of its state. The state of a dynamical system is the set of variables that completely determine the future behaviour of the system. For instance, consider the simple case of the planetary system. The future motion of any planet can be entirely determined by the current positions and velocities of all planets in the planetary system. This leads us to the concept of state space modelling. On the other hand, modelling of electrical systems such as the amplifier has historically used an input/output modelling approach. This implies a direct link between inputs and outputs as seen in the case of transfer functions [5]. The two main modelling approaches which are relevant for aeroelastic modelling: state space and transfer functions, are briefly discussed below.

State space representation The state of a system is a carefully chosen set of variables that completely describe the future response of the system. These are represented by a vector $\mathbf{x} \in \mathbb{R}^n$ called the state space. The input or control variables are represented as $\mathbf{u} \in \mathbb{R}^p$ and the output or measured variable as $\mathbf{y} \in \mathbb{R}^q$. A non-linear system described by a differential equation of any order, say m , can be represented by the following first-order differential equation [5]:

$$\begin{aligned}\frac{d\mathbf{x}}{dt} &= \mathcal{F}(\mathbf{x}, \mathbf{u}) \\ \mathbf{y} &= \mathcal{H}(\mathbf{x}, \mathbf{u})\end{aligned}\tag{2.1}$$

The system described above is also time-invariant, that is, for a given input the output response does not depend on the time at which input is applied. When the functions \mathcal{F} and \mathcal{H} are linear, then the system can be further represented as a linear time-invariant state space system [5]:

$$\begin{aligned}\frac{d\mathbf{x}}{dt} &= \mathbf{A}\mathbf{x} + \mathbf{B}\mathbf{u} \\ \mathbf{y} &= \mathbf{C}\mathbf{x} + \mathbf{D}\mathbf{u}\end{aligned}\tag{2.2}$$

where $\mathbf{A}, \mathbf{B}, \mathbf{C}$ and \mathbf{D} are constant matrices. \mathbf{A} represents the dynamics of the system, \mathbf{B} is the control matrix, \mathbf{C} is the sensor matrix and \mathbf{D} is the direct term [5].

The main advantage of this approach is that complex and large systems with multiple inputs and outputs can be represented by a pair of simple equations. Since the equations are standardized, general solution techniques can be developed and can be implemented through computer algorithms. The model not only shows how the inputs effect the outputs but also gives an inside view into the system by tracking the internal state variables [11]. State space has been applied to aeroelastic modelling by many authors, such as in [33] & [46].

Transfer function Most input signals can be expressed as exponentials or linear combinations of exponentials. Consider for instance an exponential input signal $u = \exp(st)$ which represents a damped sinusoidal input. Here $s = \sigma_d + i\omega_d$, where ω_d is the excitation frequency and σ_d represents the damping. It can be shown that the transient response of the system is given as [5]:

$$\mathbf{y} = \mathbf{G}(s)\mathbf{u}\tag{2.3}$$

For the linear system represented by Eqn. 2.2, the transfer function can be derived to be [5]:

$$\mathbf{G}(s) = \mathbf{C}(s\mathbf{I} - \mathbf{A})^{-1}\mathbf{B} + \mathbf{D}$$

The transfer function here represents a direct mapping between the inputs and the transient response in terms of the generalized frequency s . Hence it is also called frequency domain modelling. The total response can be found by superposition of transient response onto the steady state response of the system. It is important to understand that there is no intermediate state variable in Eqn. 2.3. Thus transfer functions only give a black box view of the system making it difficult to understand what is going on inside the system. It is primarily possible to derive transfer functions for linear feedback systems only, which means they are inapplicable to non-linear systems [5]. To give an example, Fransos et al. have numerically derived transfer functions to estimate the Theodorsen function for flow around a thin plate subjected to heave or pitching motion [19].

Modelling of complex systems presents its own set of problems. Often we are dealing with different sub-systems from different engineering domains. Solving for non-linear systems of equations can also be complicated.

Multi-domain modelling Multi-domain modelling of systems is problematic because different disciplines are suited to different modelling approaches as seen in the case of electrical and mechanical systems. This gives way to the idea of partitioning a large system into smaller sub-systems and modelling each of them individually [5]. The sub-systems are coupled together through transfer of data. For instance, in the case of an aeroelastic model this would involve matching the aerodynamic force at each element of the blade from the aerodynamic model with the external force at each structural element in the structural dynamics model.

Linearization A simplification that can be applied to non-linear systems is linearization if one is concerned about studying the behaviour of the system about an operating point. This despite the fact that most systems are non-linear in nature. The aerodynamics of wind turbines is essentially non-linear. However, if we stay close enough to the chosen operating point then the effect of small perturbations in input can be very well captured by a linear aerodynamic model. This simplification can greatly reduce the effort needed to solve and analyze the system for certain applications.

2.3. Aerodynamics

The principle of wind turbines is based on extracting mechanical energy from flowing air and converting it into electrical energy. Aerodynamic modelling is essentially interested in calculating the aerodynamic forces and moments acting on the wind turbine support structure and blades. The aerodynamic model is however not used in isolation. It is always coupled with a structural dynamics model of the wind turbine and a wind inflow model since the wind speed experienced by the wind turbine is stochastic in nature. This coupled aeroelastic model is then used to calculate the loads needed for design and optimization of wind turbines. The competing design objectives which influence the aerodynamic design include achieving a specified power for a given wind speed, load alleviation to get a lightweight structure and noise reduction. This section describes some of the commonly used aerodynamic models, especially for Horizontal axis wind turbines (HAWTs).

2.3.1. 1-D Momentum Theory

A simple 1-D method based on the principle of momentum conservation offers a simple explanation for the extraction of kinetic energy from the flow by the rotor. The rotor disc is assumed to be a frictionless, permeable disc encompassing the area A_r swept by the rotor blades [10]. Consider only the air particles which pass through this imaginary disk in a streamlined flow. The flow is assumed purely axial. The set of streamlines, representing the spatial distribution of velocities of air particles, form a streamtube. It is assumed that the particles in the streamtube do not interact in any way with air particles flowing outside, and that there is no lateral flow into the streamtube from outside. Additionally, the flow is considered to be irrotational [10].

Sufficiently upstream of the rotor, air flows axially at the uniform freestream velocity V_∞ and is at atmospheric pressure. Since the rotor extracts energy from air, the flow slows down and the streamtube expands as it approaches the rotor. Applying Bernoulli's equation to this steady incompressible flow case, the static pressure will increase while the total energy remains conserved upstream of the rotor. At the rotor, energy is extracted from the flow and it undergoes a sudden drop in static pressure while at the same time the velocity continues to decrease in a continuous manner. This leads to a pressure difference between the front and rear end of the rotor resulting in a thrust force on the rotor in the streamwise direction. Downstream of the rotor, the flow continues to slow down and expand. Far downstream of the rotor, the flow recovers to the atmospheric pressure but the velocity has been reduced. This implies that the energy extracted by the rotor can be obtained by the difference in kinetic energy of air between points far upstream and downstream of the rotor disk. The thrust force on the rotor is given by the rate of change of momentum of the flow through the rotor.

$$\text{Rate of change of axial momentum} = T = \rho A_r V_r (V_\infty - V_w) \quad (2.4)$$

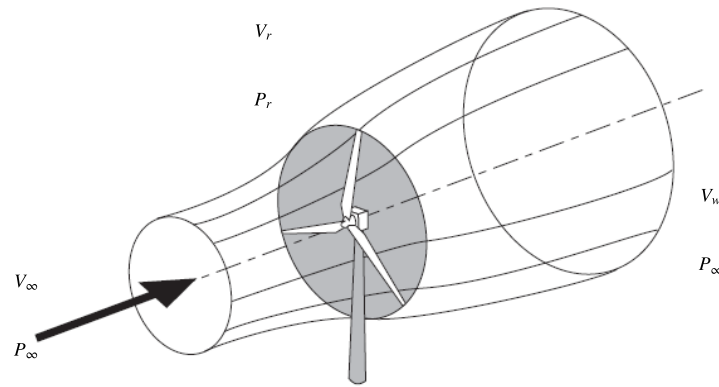


Figure 2.3: Representation of actuator disk model. Adapted from [10].

In Eqn. 2.4, V_r and V_w are the flow velocities at the rotor and at a far downstream location respectively. Furthermore, applying the Bernoulli equation separately to the flow upstream and downstream of the rotor we obtain that the pressure difference at the rotor disk is equal to the difference in kinetic energy of the flow far upstream and downstream of the rotor. This pressure difference multiplied by the area of the rotor disk can then be equated with the thrust force in Eqn. 2.4. It leads to the interesting finding that the flow velocity at the rotor is exactly half of the sum of the freestream and far wake velocity of the wind. We can use this fact to specify the axial velocity in the far wake using a non-dimensional axial induction factor a , ratio of the induced velocity and freestream air velocity, as follows:

$$V_w = (1 - 2a)V_\infty \quad (2.5)$$

The power extracted by the rotor can be further deduced as the product of the thrust force and the wind velocity at the rotor. Accordingly, a non-dimensional power coefficient C_p , and thrust coefficient C_T are defined as follows [10]:

$$C_p = \frac{P}{\frac{1}{2}V_\infty^3 A_r} = 4a(1 - a)^2 \quad (2.6)$$

$$C_T = \frac{T}{\frac{1}{2}V_\infty^2 A_r} = 4a(1 - a) \quad (2.7)$$

Differentiating C_p with respect to a we obtain the important result of the Lanchester-Betz limit which gives the maximum achievable value of the power coefficient as 16/27 for an axial induction factor of 1/3 [10]. This is a theoretical limit to the power coefficient without even considering any losses. This is because far upstream of the rotor the streamtube has a smaller diameter than the rotor disk and this in turn limits the mass flow and consequently the maximum amount of energy which is available for an ideal rotor to extract from the wind.

This simplified 1-D model has its fair share of shortcomings. Eqn. 2.7 is generally only valid for values of a less than 0.4. At values of a beyond 0.5 this theory predicts flow reversal in the wake. Experimentally however, it is observed that at high values of axial induction the wake actually becomes turbulent and interacts with the free shear layer at the edge of the streamtube leading to transfer of energy from the shear layer to the wake. This sustains the wake and provides it sufficient kinetic energy to achieve atmospheric pressure far downstream. As the rotor tip speed ratio (TSR) increases further, and the flow encounters increasing blockage the value of C_T predicted by Eqn. 2.7 is no longer valid. Since most of the flow can no longer permeate the fast rotating disk, it must flow around it. Air moves in the radial direction and at the edge of the disk it must have a sufficiently large velocity to follow the sharp curvature at the edge of the disk. The flow is likely to separate at this point and as a result a low pressure region develops at the rear side of the disk. This in turn

will lead to a much larger value of C_T than has been predicted by Eqn. 2.7. The parabolic curve prediction of C_T by momentum theory can be corrected in favour of a straight line through the experimentally determined points. An empirical relation for C_T can be derived, and is stated as follows [10]:

$$C_T = C_{T1} - 4(\sqrt{C_{T1}} - 1)(1 - a) \quad (2.8)$$

where C_{T1} represents the value of C_T when a is 1 and is usually taken to be 1.816 [10].

The 1-D model also fails to account for the rotational effect of the rotor and its geometry on the wake. While the rate of change of axial momentum gives an idea about the extraction of kinetic energy from the wind it gives no information regarding the conversion of that energy into useful work. For real turbines, the rotor geometry takes the form of a certain number of blades. As a result the air passing through the rotor also exerts a torque on the blades, and accordingly the blades exert a counter torque on the air particles causing them to rotate in the opposite direction. It is this torque on the blades which is eventually converted into electricity by an electrical generator. Remember that the flow was initially irrotational. The change in angular momentum of flow after interacting with the rotor can be described through a tangential induction factor a' , ratio of the tangential induced velocity to rotational speed. Also a' and a tend to vary radially so it is appropriate to write equations for an annular ring at radius r and differential area δA_r :

$$\text{Rate of change of angular momentum} = \delta Q = \rho \delta A_r V_\infty (1 - a) 2\Omega a' r^2 \quad (2.9)$$

where δQ is the differential torque acting on the radial element under consideration. The tangential velocity induced in the wake due to the given element is $2r\Omega a'$, where Ω represents the angular velocity of the rotor. This increase in rotational kinetic energy of the flow causes a radial pressure gradient in the flow which in turn balances the centrifugal force on the rotating fluid. Similarly the differential thrust force δT is,

$$\text{Rate of change of axial momentum} = \delta T = \rho \delta A_r V_\infty (1 - a) 2a V_\infty \quad (2.10)$$

Finally, while we do discretize the rotor disk into annuli to obtain radially varying values of a and a' this discretization inherently assumes a uniform value of a and a' in the azimuthal direction. This assumption is not valid simply because in practice a rotor disk is composed of a finite number of blades. At any given point of time some air particles will interact with the blades but many more will simply pass through the rotor disk without any interaction with the blades. This simplification is further dealt with in Section 2.3.3.

2.3.2. 2-D Blade Element Method

For long and slender structures such as wind turbine blades, the radial component of flow velocity is much smaller than the axial and tangential components. Hence it is possible to apply 2-D airfoil theory to wind turbine blades. The Blade Element Method when applied to radial elements of thickness δr located at radius r states that forces on an element can be calculated using 2-D airfoil characteristics such as the lift and drag coefficients. The elemental aerodynamic lift and drag forces are dependent on the relative flow velocity W and the angle of attack at that location [10].

$$W = \sqrt{V_\infty^2 (1 - a)^2 + r^2 \Omega^2 (1 + a')^2} \quad (2.11)$$

The lift and drag forces can be further resolved into the axial and tangential direction (torque) through rotation by the inflow angle ϕ , as follows:

$$\delta T = \delta L \cos \phi + \delta D \sin \phi \quad (2.12)$$

$$\delta Q = (\delta L \sin \phi - \delta D \cos \phi) r \quad (2.13)$$

where δL and δD represent the differential lift and drag forces acting on the radial element at radius r . These differential forces and torques can be integrated over the complete radius of the blade R , to get the total thrust force and torque acting on the rotor [10].

2.3.3. Blade Element Momentum (BEM)

The Blade Element Momentum method combines the two separate theories: Blade Element Method and 1-D Momentum theory of actuator discs, to determine the aerodynamic loading on a wind turbine rotor. The basic idea is that the lift and drag forces acting on the blade elements at a given radius r completely account for the rate of change of momentum in the axial and tangential directions for the flow passing through a rotor annulus of radius r and thickness δr as predicted by the momentum method. This theory also implies that the radial elements are independent of each other which means that the flow through one annulus does not affect the flow through another annulus. In reality, this assumption of radial independence is strictly only applicable for an infinitely long blade.

For a given radial element with area $A_r = 2\pi r \delta r$ and chord length c , the expressions for the differential thrust force (Eqns. 2.10 & 2.12) predicted by the momentum method and blade element method can be equated. The same applies for the torque (Eqns. 2.9 & 2.13). Substituting for the lift and drag forces in terms of the lift and drag coefficients, we get for a B -bladed rotor [10]:

$$\delta T = \frac{1}{2} \rho W^2 B c (C_l \cos \phi + C_d \sin \phi) \delta r = 2\pi r \delta r \rho V_\infty (1-a) 2a V_\infty \quad (2.14)$$

$$\delta Q = \frac{1}{2} \rho W^2 B c r (C_l \sin \phi - C_d \cos \phi) \delta r = 2\pi r \delta r \rho V_\infty (1-a) 2a' r^2 \Omega \quad (2.15)$$

The inflow angle ϕ is itself a function of a and a' (Eqn. 2.16) and so is the angle of attack. The lift and drag coefficients obtained from the airfoil polars data are non-linear functions of angle of attack.

$$\tan \phi = \frac{V_\infty (1-a)}{r \Omega (1+a)} \quad (2.16)$$

This implies that we have a pair of non-linear equations (Eqns. 2.14 & 2.15) which must be solved iteratively. One way of doing this is to assume an initial guess value for a and a' , and use these to calculate ϕ . The two rearranged equations for the axial thrust and torque given below are then solved for updated values of a and a' [10].

$$\frac{a}{1-a} = \frac{\sigma_r}{4 \sin^2 \phi} (C_l \cos \phi + C_d \sin \phi) \quad (2.17)$$

$$\frac{a'}{1+a'} = \frac{\sigma_r}{4 \sin \phi \cos \phi} (C_l \sin \phi - C_d \cos \phi) \quad (2.18)$$

where,

$$\sigma_r = \frac{Bc}{2\pi r} \quad (2.19)$$

is the chord solidity defined as the ratio of the total chord length and the rotor annulus circumference for a given element. The equations are solved iteratively till the values of a and a' show negligible variation over

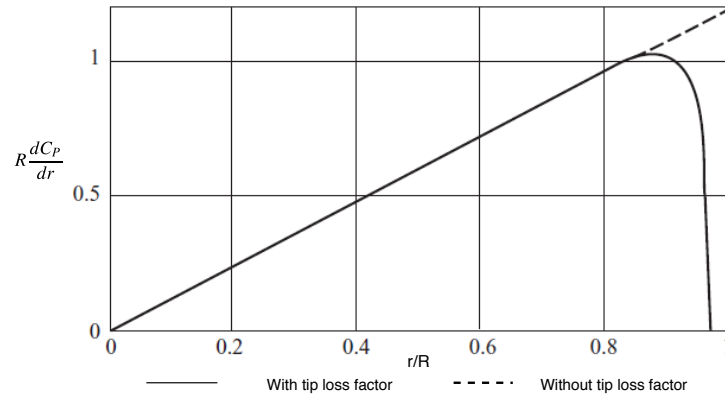


Figure 2.4: Spanwise variation of power extraction with and without tip loss for a blade with uniform circulation on a three-bladed turbine operating at a tip speed ratio of six. Adapted from [10].

successive iterations. Then the solution is said to be converged and the values of the induction factors can be used to determine the complete aerodynamic loading on the wind turbine.

The assumption of azimuthally uniform induction factors stemming from the 1-D Momentum theory also needs consideration. For optimum performance of rotors a uniform axial induction factor close to the value specified by the Betz-Lancaster limit is required. So $a = 0.3$ for all spanwise locations including the tip but for an air particle just outside the streamtube a must become zero. While BEM would predict a sudden drop in the value of a at the tip, physically it is observed that the induction factors will approach zero in a continuous fashion. This leads to the definition of a tip loss factor for blades. At the tip, close to the blade azimuthal position the induction factor will be large but becomes smaller away from the blade azimuthal position. This implies a lower inflow angle and angle of attack than predicted by the azimuthally averaged induction factors. If operating in the linear region of the $C_l - \alpha$ curve this would lead to a smaller lift force and hence a smaller contribution to the overall power coefficient. This phenomena is more pronounced near the blade tips as can be seen when the spanwise contribution to power extraction is plotted in Fig. 2.4. Similar to the blade tip loss, the induction factor at the root must also approach zero and this leads to the definition of a root loss factor. For BEM, tip and root loss factors as derived by Prandtl are commonly used [10]:

$$f_{tip} = \frac{2}{\pi} \cos^{-1} \left[\exp \left(-\frac{B(R-r)}{2r \sin \phi} \right) \right] \quad (2.20)$$

$$f_{root} = \frac{2}{\pi} \cos^{-1} \left[\exp \left(-\frac{B(r-R)}{2r \sin \phi} \right) \right] \quad (2.21)$$

Finally, the combined tip-root loss factor [10],

$$f = f_{tip} f_{root} \quad (2.22)$$

2.3.4. Unsteady BEM

The BEM theory developed so far is applicable for calculating steady state loads and for zero yaw angle. In reality, the wind velocity seen by the blade is unsteady due to a combination of factors including atmospheric turbulence, wind shear and the tower shadow effect. Moreover, we must also include the structural motion in calculating the relative velocity of the wind [28].

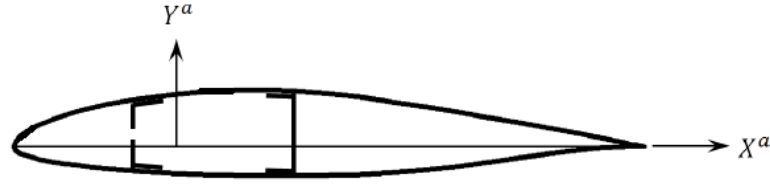


Figure 2.5: Airfoil coordinate system

Dynamic inflow First, we describe the dynamic effect of the inflow velocity to changes in the loading conditions on the rotor, commonly known as the dynamic inflow phenomena. Consider a sudden change in the blade pitch angle. The induced velocity does not respond instantaneously to such a change but in fact will gradually change to the new equilibrium value [60]. This phenomena is due to the influence of the time varying trailing wake vorticity on the inflow [59]. A time filter function, proposed by Øye [1], can be used to capture the time delay incurred by the induced velocity in adjusting to a sudden change in pitch angle or freestream velocity [28]. Here, V_i refers to the induced velocities after accounting for dynamic inflow, applicable in both axial and tangential directions, defined earlier through the induction factors. The dynamic inflow model describes the wake dynamics by using two successive first order differential equations [37]. First the quasi-steady induced velocity $V_{i,q}$ (no wake effects are included) is modified according to a first order dynamic of the wake and then the second radially dependent time filter modifies the inflow to ensure that tip elements react faster than root [37].

$$\frac{d}{dt} \begin{bmatrix} \hat{V}_i \\ V_i \end{bmatrix} = \begin{bmatrix} -\tau_1^{-1} & 0 \\ \tau_2^{-1} & -\tau_2^{-1} \end{bmatrix} \begin{bmatrix} \hat{V}_i \\ V_i \end{bmatrix} + \begin{bmatrix} 0.4\tau_1^{-1} \\ 0.6\tau_2^{-1} \end{bmatrix} V_{i,q} \quad (2.23)$$

where \hat{V}_i is an intermediate variable and the time constants are given as,

$$\begin{aligned} \tau_1 &= \frac{1.1}{1 - 0.3a} \left(\frac{R}{V_\infty} \right) \\ \tau_2 &= \left[0.39 - 0.26 \left(\frac{r}{R} \right)^2 \right] \tau_1 \end{aligned} \quad (2.24)$$

Circulation lag To begin with let us define an airfoil coordinate system as shown in Fig. 2.5. This is different from the rotor plane coordinates we have worked with so far because the new coordinates follow the airfoil profile.

The quasi-steady angle of attack α_q , which considers velocities arising from the vertical and/or pitching motion of the blade, but not the downwash induced by the unsteady wake, is expressed in terms of the components of the relative velocity in the airfoil attached coordinate system, V_x and V_y .

$$\tan \alpha_q = \frac{V_y}{V_x} \quad (2.25)$$

In unsteady aerodynamics, when an airfoil angle of attack changes, a time delay is incurred before the sectional aerodynamic loads reach the equilibrium values because of the shed vorticity. The time lag is given by the time it takes for the shed vortices to convect far downstream. This effect is captured by an empirical model for circulation lag as proposed by Leishman et al. [41]. A state space containing two parameters, a_1

and a_2 is defined for each airfoil section. This leads to an intermediate output, the so called "Theodorsen" angle of attack (α_T).

$$\begin{aligned} \frac{d}{dt} \begin{bmatrix} a_1 \\ a_2 \end{bmatrix} &= \begin{bmatrix} 0 & 1 \\ A_{21} & A_{22} \end{bmatrix} \begin{bmatrix} a_1 \\ a_2 \end{bmatrix} + \begin{bmatrix} 0 \\ 1 \end{bmatrix} \alpha_q \\ \alpha_T &= [K_1 \quad K_2] \begin{bmatrix} a_1 \\ a_2 \end{bmatrix} + K_3 \alpha_q \end{aligned} \quad (2.26)$$

The various parameters used in the empirical model of Eqn. 2.26 are defined as follows [41]:

$$\begin{aligned} b_1 &= 0.0455, \quad b_2 = 0.3, \quad A_1 = 0.165, \quad A_2 = 0.335 \\ A_{21} &= -b_1 b_2 \left(\frac{2W}{c} \right)^2, \quad A_{22} = -(b_1 + b_2) \left(\frac{2W}{c} \right) \\ K_1 &= (A_1 + A_2) b_1 b_2 \left(\frac{2W}{c} \right)^2, \quad K_2 = (A_1 b_1 + A_2 b_2) \left(\frac{2W}{c} \right), \quad K_3 = 1 - A_1 - A_2 \end{aligned} \quad (2.27)$$

where c is the chord length and W is the resultant planar velocity in the airfoil coordinate system, neglecting the spanwise component.

Dynamic stall For stalled flows another unsteady phenomena called dynamic stall becomes important. Hansen [28] states that for wind turbines trailing edge separation is assumed to be the most important effect. An increase in angle of attack will lead to the point of flow separation shifting upstream on the upper surface of the airfoil. The viscous boundary layer takes some time adjust to this change in angle of attack and this delay in turn leads to a lag in the aerodynamic response [28]. For dynamic stall, a linear model proposed by Merz [45] which is based on Øye's non-linear model [55] can be used to define a dynamic angle of attack α , which is the real angle of attack including unsteady effects.

$$\frac{d\alpha}{dt} = -\frac{1}{\tau} \alpha + \frac{1}{\tau} \alpha_T \quad (2.28)$$

where,

$$\tau = 4.3 \frac{c}{W} \quad (2.29)$$

Using α it is now possible to calculate the lift and drag coefficients.

$$\begin{aligned} C_l(\alpha, \alpha_q) &= C_l(\alpha) \left(1 + \frac{\alpha_q - \alpha}{\alpha - \alpha_z} \right) \\ \lim_{\alpha \rightarrow \alpha_z} C_l(\alpha, \alpha_q) &= \frac{dC_l}{d\alpha} (\alpha_q - \alpha_z) \\ C_d(\alpha) &= C_d(\alpha_q) \end{aligned} \quad (2.30)$$

In Eqn. 2.30, α_z represents the zero lift angle of attack in the linear part of the $C_l - \alpha$ curve.

2.3.5. Vortex wake models

The inherent shortcomings of BEM in accounting for 3-D effects at the tip/root as well as unsteady effects has been explained earlier. While empirical correction factors can somewhat alleviate those problems, they too

are approximate and may not perform well for all ranges of operating conditions. A more accurate approach to model wind turbine aerodynamics is to model the wake physics using vortices.

Consider an incoming flow field which is incompressible, inviscid and irrotational thus satisfying the conditions of potential flow. One way to model the wake of lift generating surfaces such as an airfoil is through a uniform flow field superimposed on a vortex of appropriate strength. Extending this concept to a complete blade we get a lifting line model wherein the blade is discretized and each blade section will have its own circulation strength, Γ . The circulation is constant over a blade element, and is related to the lift generated by that element through the Kutta-Joukowski theorem in Eqn. 2.31 [3]. An alternative is the vortex panel method where a finite number of straight panels, each having its own vorticity, are placed side by side covering the profile of the airfoil such that for each panel the flow is strictly tangential. A common simplification used for thin airfoils is to place vortex panels along the camber line [3].

$$L' = \rho_{\infty} V_{\infty} \Gamma \quad (2.31)$$

At steady state, the spanwise variation in circulation along the blade leads to the generation of trailing vortices at the boundary of two adjacent elements whose circulation does not match. These trailing vortices convect downstream in a helical path, and when seen in respect of the complete rotor a vortex tube is formed downstream. The velocity induced by these trailing vortices at the blade elements is responsible for slowing down the flow axially and accelerating it in the tangential direction. This induction can be calculated by using the Biot-Savart law [3], which states that the induced velocity by a wake element is given as:

$$d\mathbf{v}_i = \frac{\Gamma}{4\pi} \frac{d\mathbf{l} \times \mathbf{r}}{|\mathbf{r}|^3} \quad (2.32)$$

where \mathbf{r} in this formula represents the vector from wake element $d\mathbf{l}$ to the point at which induction is calculated.

An important issue for unsteady aerodynamics is knowledge about the spatial position of the wake in time and with respect to the blades. Two approaches: frozen and free wake modelling, are commonly used. In a frozen wake model it is assumed that the speed at which the wake travels downstream is known beforehand. A free vortex model differs from the frozen vortex one in the sense that the spatial position of the wake is not prescribed arbitrarily or from experiments but instead the wake is allowed to develop freely. The wake velocity is determined by the superposition of the freestream velocity, induced velocity due to the bound vorticity and self-induced velocity by the wake [29].

For implementation of a steady lifting line model, one starts with a guess value of the bound circulation on the blades. These vortices are generally placed at the quarter-chord position of each airfoil section. Since the expression for the velocity induced by a complete vortex tube is analytically difficult to obtain, the wake is discretized into linear elements. Now applying the Biot-Savart law for each wake element we can get the induced velocities at the different blade positions. Typically, the induced velocities are calculated at the three-quarter-chord position of each airfoil. The induced velocity in combination with the blade rotation and freestream velocity determines the inflow angle and angle of attack at a blade section. Subsequently it becomes possible to calculate the lift from the airfoil data and corresponding circulation using the Kutta-Joukowski Theorem (Eqn. 2.31). An iterative approach can be used to solve this problem wherein we start with an initial guess value of circulation and solve for the converged value of circulation. If the value of bound circulation at the start and end of an iteration (using Eqn. 2.31) match then we have a solution. Once the bound circulation on the blade is known then the aerodynamic lift force distribution can be determined [3].

In addition to trailing vortices, for unsteady aerodynamic problems one has to consider the vortices shed in time due to Kelvin's Theorem. Kelvin's theorem postulates that the total circulation in a closed contour consisting of the same fluid elements remains constant in time [32]. The procedure followed is similar to the one described for the steady state case but now must be implemented repeatedly for multiple time steps. Within each time step, the combined induced velocity due to bound vorticity, trailing vortices and shed vortices is now considered to get a converged solution at each time step. For any prescribed motion of an airfoil, the dif-

ference in bound vorticity between the beginning and end of a time step can be used to calculate the strength of the shed vortices for the given time step which in turn will influence induced velocity in the future time steps [40].

Both frozen and free vortex wake models are computationally expensive to model, but free vortex models are even more so since the wake position itself is unknown and needs to be calculated at each iteration. Therefore, their application to reduced-order aeroelastic modelling is problematic. Nevertheless, vortex wake models give great physical insight into the modelling of wakes and provide more realistic results as compared to BEM. For cases such as heavily loaded rotors operating in the vortex ring/turbulent wake state, vortex wake models are known to perform surprisingly well despite the inherent assumptions in these models [29].

2.3.6. Computational Fluid Dynamics (CFD)

Computational Fluid Dynamics (CFD) is the term used to describe numerical methods which solve for the fundamental Navier-Stokes system of equations describing the physics of fluid motion. There are two broad ways in which CFD can be applied to study wind turbine rotor aerodynamics.

The first approach involves combining the Navier-Stokes (or simplified Euler) equations with an actuator disc model (described in Section 2.3.1). In this approach the rotor is not modelled in the form of blades but as a swept disc. This swept disc is then represented in the form of a force field acting on the flow. The Navier-Stokes equations are generally discretized by a second-order finite difference/volume numerical scheme and solved along with the axisymmetric flow assumption [29]. The axisymmetric assumption simplifies the computation but similar to BEM it implies that the flow field is invariant in the azimuthal direction. Similar to the Blade Element Method, the force field can be calculated using 2-D airfoil characteristics with corrections for 3-D effects.

The general CFD approach involves solving the flow field around the actual rotor geometry. For this purpose, a mesh is constructed around the blade geometry. This mesh must accurately resolve the blade geometry especially at the leading and trailing edges, and must also finely discretize the region near the blade to capture boundary layer dynamics. Since the flow in a wind turbine is largely incompressible, it is possible to solve for the incompressible Navier Stokes equation. To get realistic results, phenomena such as flow transition and turbulence should also be included. A common method to include turbulence are the Reynolds Averaged Navier-Stokes equations (RANS). Typically, a second order implicit time marching scheme is used to obtain the solution such that accuracy remains independent of the time step size. A non-zero rotor yaw configuration can also be simulated but this necessarily requires doing away with the axisymmetric flow assumption and incurring additional computational cost [29].

The computational cost and memory requirements for a CFD analysis of the rotor wake are much greater than those for BEM and vortex wake models. However, besides the typical outputs of low-speed shaft torque, power and root flap moments, a CFD analysis provides a huge amount of detailed information which is particularly useful in studying different aerodynamic details of the rotor such as the blade tips, design of the root sections, etc. [29]. Thus CFD methods can be used in studying the detailed physics of the rotor wake including viscous effects, that is, applications of the kind not catered to by BEM and vortex wake methods. However, this approach is not suited for reduced-order aeroelastic modelling.

2.4. Structural Dynamics

Notwithstanding the current trend in the wind turbine industry to build larger wind turbines, these machines must be lightweight to reduce cost yet at the same time structurally reliable and stable. A lightweight design also makes the structure more flexible and consequently more dynamically active. Traditionally, the design methodology involved analyzing the dynamic response for extreme loading, fatigue loading and resonance stability [30]. However as turbines become increasingly flexible, there is increasing interaction and coupling of blade and tower motion with the aerodynamics. This leads us to the current state where aeroelastic instabilities must be studied and avoided at all cost.

An accurate structural dynamics model coupled with an aerodynamics model helps us achieve all the aforementioned design goals. A detailed structural model of the wind turbine incorporates the following main components - foundation, tower, nacelle, drivetrain and blades.

This section begins by describing a method to derive the equations of motion for a body, namely the Lagrange's method. Next we look at how the structural degrees of freedom are represented. Three commonly used approaches to model the structural dynamics of wind turbines: multibody, finite element and modal approach are briefly described. It is shown how these different approaches can also be combined. Then we give a background into the Craig Bampton method and methods to represent rotations in large, assembled structures. This knowledge is important in the context of aeroelastic modelling.

2.4.1. Lagrange's Method

The Lagrange method presents a generalized methodology to derive the equations of motion for any system based on its kinetic and potential energy. Unlike Newton's method, based on making free-body diagrams for each body, it does not require direct knowledge of forces and their directions. This makes it particularly suitable for complex systems with large number of degrees of freedom and for dealing with constraints [31].

For any system under consideration, the Lagrangian \mathcal{L} of the system is defined in terms of the kinetic (E_K) and potential energy (E_P) as follows [31]:

$$\mathcal{L}(q, \dot{q}) = E_K - E_P \quad (2.33)$$

We also define a quantity called the action S which is associated with the Lagrangian as follows [12]:

$$S = \int_{t_1}^{t_2} \mathcal{L}(q, \dot{q}) dt \quad (2.34)$$

The fundamental concept is that the system always follows a particular path which minimizes the action S [12]. This concept is encapsulated in the Hamilton's Principle and leads further to the Euler-Lagrange equation [31] given below for a conservative force field, which is captured in the potential energy term [12].

$$\frac{d}{dt} \left(\frac{\partial L}{\partial \dot{q}} \right) = \frac{\partial L}{\partial q} \quad (2.35)$$

Additional terms must be included in Eqn. 2.35 to account for generalized forces not included in the potential as well as the dissipating effect of non-conservative forces. The expanded Euler-Lagrange equation is given in terms of the rate of energy dissipation \dot{E}_D , and work done by the generalized forces W_g in Eqn. 2.36 [48].

$$\frac{d}{dt} \left(\frac{\partial E_K}{\partial \dot{q}} \right) - \frac{\partial E_K}{\partial q} + \frac{1}{2} \frac{\partial \dot{E}_D}{\partial \dot{q}} + \frac{\partial E_P}{\partial q} = \frac{\partial W_g}{\partial q} \quad (2.36)$$

2.4.2. Structural models

This section gives a background into three commonly used methods to model the structural dynamics of structures in the context of wind turbines. These are: multibody system method, finite element method and the modal representation approach. It is also shown that its possible to combine more than one of these three structural dynamics modelling approaches to represent large, assembled structures.

Multibody System In the Multibody System (MBS) method, each sub-structure of a complete assembly such as a wind turbine is treated as a rigid body and bodies are assumed to be connected together by inelastic

joints [49]. A floating reference frame is defined for each body and a fixed global reference frame for the entire configuration. Degrees of freedom will be defined for each body and differential equations can be derived to represent the body motion. Large rigid body displacements and rotations of each body can be captured by a finite number of differential equations which define the system [49]. However, the elastic deformations of the sub-structures as well as the joints are neglected [49]. This approach is suitable for applications such as control system design where a low-fidelity model can suffice [49].

The elastic motion of the components can be captured if instead each component were to be treated as a flexible body and the equations of motion will then have to account for this [49]. For instance, the flexible body can be approximated as a mass-spring-damper system. In this case, each component requires an extra reference frame attached to the body which captures the elastic motion with respect to the floating body reference frame. The cost of the flexible body assumption are additional degrees of freedom and extra computational cost [49].

Finite Element Method The structural dynamics of continuous flexible structures are analytically described by differential equations which are often times impossible to solve analytically. In the finite element method, a flexible structure is treated as an assembly of a large number of geometrically simple, discrete elements. Each of these elements is represented by two or more nodal points where the solution is computed. The element behaviour must be clearly defined, for instance the 1-D beam element allows 3 translational and 3 rotational degrees of freedom. This particular element is based on the Euler-Bernoulli beam assumption of planar bending, that is the bending axis is always perpendicular to the beam cross-section and all displacements are assumed to be small. The displacement in the sub-space, that is the space between the nodes within each element, must also be approximated with a shape function and is calculated based on the nodal displacements at adjacent nodes. The nature of the shape function is important. A linear shape function cannot be expected to capture non-linear phenomena such as buckling.

The equations of motion are derived for each element and are subsequently assembled to get a global equilibrium. In the final step, loads and constraints are applied. The finite element system can then be solved to get the structural response of the system. Since this method involves a large number of nodes and degrees of freedom, it also comes with a high computational cost as compared to the multibody approach. As a result, this method is considered suitable for static analysis but less so for dynamic analysis [49]. However, with application of suitable order reduction techniques this method is nowadays also being applied to time marching dynamic simulations but with the caveat of the small displacements and rotations assumption made for the simplified Euler-Bernoulli beam.

Modal representation The structural dynamics of a system can also be represented in terms of the modes of the system. This is generally an extension to the finite element model wherein the generalized eigenvalue problem is solved for the global equations of motion derived by the finite element method. The eigenvectors obtained are the global modes and are subsequently used to transform the equation of motion such that it is now in terms of the modal degrees of freedom instead of the generalized degrees of freedom defined in the finite element model. The complete displacement of a body for instance is now obtained as a superposition of the different modes weighted by the respective modal degrees of freedom.

It is generally found that as the frequency of a mode increases, its contribution to the dynamic response becomes smaller. This means higher order modes can be ignored while solving for the structural dynamics representing a great opportunity for order reduction. Consequently, a modal representation of the structural dynamics is less computationally intensive than a full finite element model but perhaps more costly than a multi-body dynamics approach. The downside is that a full finite element must be derived first to get the modes of the system [49]. The accuracy of the results depends on the quality of modes derived, that is, how accurately do the mode shapes represent the real deformations. The problematic part is that since the deformation of bodies are not known beforehand, the selection of modes is usually random. It is quite possible that some effects, for instance the centrifugal stiffening effect in wind turbine blades are not captured because the blade mode which represents the radial displacement of blade elements is one of the high order modes which was omitted [49].

Hybrid approach While three different structural modelling approaches have been briefly described above, these can also be applied in combination with one another. A Hybrid Multibody System (HBMS) represents a structural model composed of all the three approaches [49]. For instance, consider a complex system like a wind turbine composed of different sub-structures. For each sub-structure seen as part of an assembled structure, say the tower, we apply multi-body dynamics method to capture the large rigid body displacements and rotations. On the sub-structure level, each body is assumed flexible and is discretized into idealized beam elements. The elastic deformations and rotations of the body are thereby captured. Since this would make the system description very bulky indeed, a modal reduction can be applied to replace the nodal representation of FEM to reduce the order of the system. Finally, the large rigid body motion and small elastic deformations are superimposed for each body and constraints are applied at the joints to get the complete structural deformations for the wind turbine.

In practice, this combined approach can be implemented using the corotational finite element formulation which separates out the arbitrarily large rigid body displacements and rotations from the deformations due to internal strains in the element. To do this one defines a local element coordinate system which captures the rigid body displacements and rotations of the element [17]. Now all that remains is the local deformation of the element. A coordinate system which deforms along with the element can capture the actual spatial configuration of the element, and a comparison with the local element coordinate system then gives the deformations and rotations [17]. Since we often assume that pure deformations and rotations of the elements are small relative to the corotation configuration, some standard small-strain approximations can be applied. The small-strain assumption in turn makes the finite element library consisting of the elemental mass, stiffness and damping matrices re-usable because they need not be modified dramatically after each time step in a dynamic simulation [17]. The governing equations are simplified along with an accompanying reduction in computation time.

2.4.3. Modal reduction technique : Craig-Bampton Method

One of the most common ways used to implement modal reduction on a full-order finite element model is the Craig-Bampton Method. The idea is to transform large finite element models into a set of relatively small matrices which can be further used for dynamic analysis. It is often applied in modal synthesis where models of two or more sub-structures are coupled together to efficiently analyze the complete structure [67].

Consider the standard form of the equation of motion for a free, unconstrained structure given as [67]:

$$\mathbf{M}\ddot{\mathbf{q}} + \mathbf{C}\dot{\mathbf{q}} + \mathbf{K}\mathbf{q} = \mathbf{F} \quad (2.37)$$

The nodes representing the structure can be partitioned into fixed, interfaced or constrained boundary nodes denoted by subscript R , and independent elastic nodes represented by subscript L [67].

$$\mathbf{q} = \begin{bmatrix} \mathbf{q}_R \\ \mathbf{q}_L \end{bmatrix} \quad (2.38)$$

Accordingly, the mass, stiffness and damping matrices in Eqn. 2.37 can be transformed to get [67]:

$$\begin{bmatrix} \mathbf{M}_{RR} & \mathbf{M}_{RL} \\ \mathbf{M}_{LR} & \mathbf{M}_{LL} \end{bmatrix} \begin{bmatrix} \ddot{\mathbf{q}}_R \\ \ddot{\mathbf{q}}_L \end{bmatrix} + \begin{bmatrix} \mathbf{C}_{RR} & \mathbf{C}_{RL} \\ \mathbf{C}_{LR} & \mathbf{C}_{LL} \end{bmatrix} \begin{bmatrix} \dot{\mathbf{q}}_R \\ \dot{\mathbf{q}}_L \end{bmatrix} + \begin{bmatrix} \mathbf{K}_{RR} & \mathbf{K}_{RL} \\ \mathbf{K}_{LR} & \mathbf{K}_{LL} \end{bmatrix} \begin{bmatrix} \mathbf{q}_R \\ \mathbf{q}_L \end{bmatrix} = \begin{bmatrix} \mathbf{F}_R \\ \mathbf{F}_L \end{bmatrix} \quad (2.39)$$

There are two main steps in performing the Craig-Bampton transformation. First, the physical elastic coordinates \mathbf{q}_L are replaced by modal elastic coordinates \mathbf{Q}_L in Eqn. 2.39 [67]. The boundary nodes are still

represented by physical coordinates. Secondly, the modal coordinates \mathbf{Q}_L are truncated to m ($m < L$) low-frequency modal coordinates $\boldsymbol{\eta}_m$ [67]. This makes sense because the high-frequency modes have no significant contribution to the dynamic response and hence can be omitted. The physical coordinates $[\mathbf{q}_R \quad \mathbf{q}_L]^T$ can be represented in the form of the hybrid Craig-Bampton coordinates $[\mathbf{q}_R \quad \boldsymbol{\eta}_m]^T$ as follows [67]:

$$\begin{bmatrix} \mathbf{q}_R \\ \mathbf{q}_L \end{bmatrix} = [\mathbf{B} \quad \boldsymbol{\phi}] \begin{bmatrix} \mathbf{q}_R \\ \boldsymbol{\eta}_m \end{bmatrix} \quad (2.40)$$

Here, $\boldsymbol{\phi}$ is the shape function matrix. The Craig-Bampton method can be implemented by substituting Eqn. 2.40 in Eqn. 2.39. This will yield [67]:

$$\mathbf{M} [\mathbf{B} \quad \boldsymbol{\phi}] \begin{bmatrix} \ddot{\mathbf{q}}_R \\ \ddot{\boldsymbol{\eta}}_m \end{bmatrix} + \mathbf{C} [\mathbf{B} \quad \boldsymbol{\phi}] \begin{bmatrix} \dot{\mathbf{q}}_R \\ \dot{\boldsymbol{\eta}}_m \end{bmatrix} + [\mathbf{B} \quad \boldsymbol{\phi}] \begin{bmatrix} \mathbf{q}_R \\ \boldsymbol{\eta}_m \end{bmatrix} = \begin{bmatrix} \mathbf{F}_R \\ \mathbf{F}_L \end{bmatrix} \quad (2.41)$$

Now Eqn. 2.41 is multiplied with $[\mathbf{B} \quad \boldsymbol{\phi}]^T$ to get:

$$\begin{bmatrix} \mathbf{B}^T \mathbf{M} \mathbf{B} & \mathbf{B}^T \mathbf{M} \boldsymbol{\phi} \\ \boldsymbol{\phi}^T \mathbf{M} \mathbf{B} & \boldsymbol{\phi}^T \mathbf{M} \boldsymbol{\phi} \end{bmatrix} \begin{bmatrix} \ddot{\mathbf{q}}_R \\ \ddot{\boldsymbol{\eta}}_m \end{bmatrix} + \begin{bmatrix} \mathbf{B}^T \mathbf{C} & \mathbf{B}^T \mathbf{C} \boldsymbol{\phi} \\ \boldsymbol{\phi}^T \mathbf{C} \mathbf{B} & \boldsymbol{\phi}^T \mathbf{C} \boldsymbol{\phi} \end{bmatrix} \begin{bmatrix} \dot{\mathbf{q}}_R \\ \dot{\boldsymbol{\eta}}_m \end{bmatrix} + \begin{bmatrix} \mathbf{B}^T \mathbf{K} \mathbf{B} & \mathbf{B}^T \mathbf{K} \boldsymbol{\phi} \\ \boldsymbol{\phi}^T \mathbf{K} \mathbf{B} & \boldsymbol{\phi}^T \mathbf{K} \boldsymbol{\phi} \end{bmatrix} \begin{bmatrix} \mathbf{q}_R \\ \boldsymbol{\eta}_m \end{bmatrix} = [\mathbf{B} \quad \boldsymbol{\phi}]^T \begin{bmatrix} \mathbf{F}_R \\ \mathbf{F}_L \end{bmatrix} \quad (2.42)$$

2.4.4. Representation of rotations

When dealing with multibody systems, it is normal to operate with at least two types of coordinate systems. The first is the inertial or global coordinate frame which is fixed and acts as a reference for all bodies in the system. Secondly, a separate body reference coordinate system is fixed to each body in the system. This coordinate frame translates and rotates with the body, and hence its position and orientation with respect to the global frame changes with time.

In the study of structural dynamics, it becomes important to transform quantities measured in the body reference frame back to the global frame and vice versa. While the translation of rigid bodies is fairly straightforward, a lot of attention has been paid by mathematicians and engineers to the parameterization of 3-D rotations in space. The most popular and commonly used methods are briefly described below.

Euler angles This approach describes any 3D rotation as a sequence of three successive elementary rotations, where each elementary rotation is equivalent to a 2D rotation. Consider the basic rotation of a point about one of the axes of a Cartesian coordinate system which can be represented by a 3×3 rotation matrix. Lets consider the rotation of a point about the z-axis by angle θ_1 in the counter-clockwise direction. The matrix \mathbf{T} (Eqn. 2.43) when multiplied by a vector containing the coordinates of a point in the body reference frame gives the coordinates in the global reference frame as follows [58]:

$$\mathbf{T} = \begin{bmatrix} \cos \theta_1 & -\sin \theta_1 & 0 \\ \sin \theta_1 & \cos \theta_1 & 0 \\ 0 & 0 & 1 \end{bmatrix} \quad (2.43)$$

Similar rotations can be performed about the x and y axes as well. In general, the axes need not be orthogonal. However, since the Euler angles are not unique it is important to define a convention which is strictly adhered to. The Euler angle is a degree of freedom representing rotation about one axis. That makes it a total of three independent parameters to represent any rotation in space.

Three successive rotations about fixed axes, θ_1 followed by θ_2 followed by θ_3 can be represented by $\mathbf{T}_{\text{total}}$ given below:

$$\mathbf{T}_{\text{total}} = \mathbf{T}_3(\theta_3)\mathbf{T}_2(\theta_2)\mathbf{T}_1(\theta_1) \quad (2.44)$$

The general form of the rotation matrix is:

$$\mathbf{T}_{\text{total}} = \begin{bmatrix} \hat{u}_x & \hat{v}_x & \hat{w}_x \\ \hat{u}_y & \hat{v}_y & \hat{w}_y \\ \hat{u}_z & \hat{v}_z & \hat{w}_z \end{bmatrix} \quad (2.45)$$

The three independent angles which form this matrix can be stored to describe the complete rotation. This parameterization is simple to understand and derivatives of the rotation matrix are easy to calculate [24]. However it suffers from singularities at certain orientations of the body and interpolation of Euler angles leads to poor interpolation of rotations [24].

Rodriguez parameters Euler's Theorem of rotation states that it is possible to represent any 3-D rotation in terms of an axis-angle representation, that is any rotation in space is seen as a rotation by a single angle θ about an axis of rotation in space [58]. Let us represent this axis by the unit vector \mathbf{v} . Then the rotation matrix, given by the Rodrigue formula can be represented in terms of a unit vector along the axis of rotation and the angle of rotation [58].

$$\mathbf{T} = \mathbf{I}_3 + \tilde{\mathbf{v}}\sin\theta + 2(\tilde{\mathbf{v}}^2 \sin^2 \frac{\theta}{2}) \quad (2.46)$$

where $\tilde{\mathbf{v}}$ is a skew-symmetric matrix given in terms of components of \mathbf{v} by [58]:

$$\tilde{\mathbf{v}} = \begin{bmatrix} 0 & -v_3 & v_2 \\ v_3 & 0 & -v_1 \\ -v_2 & v_1 & 0 \end{bmatrix} \quad (2.47)$$

Since it is known that \mathbf{v} is a unit vector, the rotation can be represented by a set of three independent parameters known as the Rodrigue parameters, $\boldsymbol{\gamma}$ [58].

$$\mathbf{s} = [s_1 \quad s_2 \quad s_3]^T \quad (2.48)$$

where,

$$\begin{aligned} s_1 &= v_1 \tan \frac{\theta}{2} \\ s_2 &= v_2 \tan \frac{\theta}{2} \\ s_3 &= v_3 \tan \frac{\theta}{2} \end{aligned} \quad (2.49)$$

The disadvantage of this approach is the singularities which may occur at certain orientations of the body in space [24].

Quaternions This approach makes use of quaternions to give a four parameter representation of the rotations consisting of a vector part and a scalar part. The unit vector part indicates the direction of the axis of rotation $\hat{\mathbf{v}}$, and the scalar part indicates the angle of rotation θ . The rotations, represented by \mathbf{s} here, are as follows:

$$\mathbf{s} = [s_x \quad s_y \quad s_z \quad s_w]^T = [\hat{\mathbf{v}} \sin \frac{\theta}{2} \quad \cos \frac{\theta}{2}]^T = [\mathbf{s}_v \quad s_w]^T \quad (2.50)$$

Quaternions have their own definition of the basic mathematical operations. The conjugate ($\bar{\mathbf{s}}$) and multiplication operations ($\mathbf{s} \circ \mathbf{r}$) which are needed for defining the rotation matrix are defined as follows [15]:

$$\begin{aligned} \bar{\mathbf{s}} &= [-s_x \quad -s_y \quad -s_z \quad s_w]^T \\ \mathbf{p} = \mathbf{s} \circ \mathbf{r} &= \begin{bmatrix} (s_w)_r \mathbf{s}_v + s_w (\mathbf{s}_v)_r + \mathbf{s}_v \times (\mathbf{s}_v)_r \\ s_w (s_w)_r - \mathbf{s}_v \cdot (\mathbf{s}_v)_r \end{bmatrix} \end{aligned} \quad (2.51)$$

where $\mathbf{r} = [(s_x)_r \quad (s_y)_r \quad (s_z)_r \quad (s_w)_r]^T$ is a quaternion. The quaternion multiplication is a combination of vector dot and cross products [15]. Now the global coordinates \mathbf{x}' (which is the coordinate vector appended with a zero in the fourth row) can be obtained from the body frame coordinates $\tilde{\mathbf{x}}$ as follows [24]:

$$\mathbf{x}' = \mathbf{s} \circ \tilde{\mathbf{x}} \circ \bar{\mathbf{s}} \quad (2.52)$$

The unit-length quaternion approach avoids singularities and gives simple formulas to obtain the derivatives of the rotation matrix with respect to the rotation parameters [24]. It gives very good results when used for interpolating rotations [24]. However, adding an extra parameter is detrimental to computational efficiency. When used in applications such as control a constraint must be enforced to keep the quaternion at unit length [24]. This is because while there are three degrees of freedom but there are four directions in which a quaternion is free to change [24].

Exponential map The problems that arise in quaternion parameterization can be overcome to a large extent by using a three parameter representation known as the exponential map. It maps a vector in $\mathbf{s} \in \mathbb{R}^3$ describing the angle and axis of rotation. The formulation of the exponential map parameters for $|\mathbf{v}| \neq 0$ is as follows:

$$\mathbf{s} = [\theta \hat{\mathbf{v}}]^T \quad (2.53)$$

where $\theta = |\mathbf{s}|$ and $\hat{\mathbf{v}} = \frac{\mathbf{v}}{|\mathbf{v}|}$. The rotation matrix is defined to be the exponential of a skew-symmetric matrix Θ referred to as the spin of \mathbf{s} [48].

$$\Theta = \begin{bmatrix} 0 & -s_z & s_y \\ s_z & 0 & -s_x \\ -s_y & s_x & 0 \end{bmatrix} \quad (2.54)$$

Finally, we can obtain the rotation matrix by using a Taylor expansion to approximate the exponential [17].

$$\mathbf{T} = \exp(\Theta) \approx \mathbf{I} + \frac{\sin \theta}{\theta} \Theta + \frac{1 - \cos \theta}{\theta^2} \Theta^2 \quad (2.55)$$

The expression in Eqn. 2.55 can be evaluated even as $\theta \rightarrow 0$ since the limits of the terms in the RHS can still be evaluated. An alternative is that the rotation matrix can be calculated by converting the exponential map parameters to the quaternion form [24]. The derivatives can be calculated by simple formulas similar to ones used in the quaternion representation [24]. Overall, this parameterization is ideally suited for control and dynamic simulations as it avoids any explicit constraints, that is, it does not need re-normalization after every time step [24]. Another advantage is the computational efficiency of using three parameters to describe the rotation [24].

2.5. State-of-the-art aeroelastic codes

Having looked at a variety of aerodynamic and structural dynamics modelling methods in previous sections, it is now possible to combine the two. A variety of aeroelastic codes for wind turbines are available, some as open-source and others through commercial licenses. They can have two main modes of operation: dynamic simulation to study the time response, and linearization about a point to study the frequency response. Most modern codes include both operational modes, but some codes do not perform linearization and run only a non-linear time marching simulation to study the load response [30]. The codes are modular in nature, with the different modules coupled together for an integrated aeroelastic response study. Apart from the aerodynamic and structural dynamics, there are other modules to describe the inflow conditions, controller, hydrodynamics, icing conditions etc. The number of modules usually varies from code to code. The codes are implemented in a general-purpose programming language for which a vast library of built functions already exists. Most modern aeroelastic codes come with a Graphical User Interface (GUI) such that the focus of the user remains on design rather than handling the model [49]. This ofcourse leads to general purpose tools which may not be easily adapted to specific user requirements.

The aerodynamics of most codes is described by the BEM theory corrected with a blade tip/root loss factor and an empirical relation for calculating the thrust coefficient of heavily loaded rotors [49]. The velocity induction given by the algebraic equations of BEM are passed through a first order filter to capture the dynamic inflow effect. Semi-empirical models are used for the dynamic stall effect. Lastly, some codes utilize semi-empirical relations to correct 2-D airfoil data for 3-D effects [49].

There are simplified aeroelastic codes based on the multibody approach which are particularly useful for control system design [49]. More detailed aeroelastic codes however use a finite element model followed by modal reduction to study the structure. The rotor modes usually represented are the 1st edgewise along with the 1st and 2nd flapwise modes. Torsion modes are usually omitted because blades were till recently stiff in torsion [49].

Below an overview of three commonly used aeroelastic codes for wind turbines is provided to give a flavour of the current state-of-the-art in this field.

FAST FAST (Fatigue, Aerodynamics, Structures and Turbulence) is a non-linear, integrated, dynamic aero-hydro-servo-elastic simulation tool for design applications originally conceived as a confluence of three distinct codes - FAST2 Code for two-bladed HAWTs, FAST3 for three-bladed HAWTs and the AeroDyn program for HAWTs at National Renewable Energy Laboratory (NREL), USA [49]. It originated as an aeroelastic code but has evolved over time to append new modules for including hydrodynamics of offshore structures, control logic and electrical system (servo) dynamics [35]. The latest version available is an open-source version appropriately named OpenFAST which is a modular code written mostly in Fortran [54]. The FAST Code is applicable to a wide variety of HAWTs such as both two or three bladed rotors, land based or offshore, pitch or stall-regulated control, upwind or downwind rotor, yawed rotor, lattice or tubular tower, and fixed-bottom or floating sub-structures. Apart from the dynamic simulations, it is also possible to obtain linearized matrices about an operating point for frequency domain analysis [35].

The aerodynamic module AeroDyn describes the rotor-wake aerodynamics using a quasi-steady BEM based induction model. It includes the standard Prandtl tip/root loss correction and Glauert's empirical correction as modified by Buhl for heavily loaded rotors [36][8]. Additionally, a correction for skewed wake as developed

by Pitt and Peters can also be applied by the user for yawing [36][51]. The latest versions of AeroDyn (v15.03 & v15.04) do not have a dynamic inflow model which accounts for induction dynamics. Unsteady airfoil aerodynamic effects such as dynamic stall are included through an extended Beddoes-Leishman type model [36]. The tower effect on the blade flow is modelled using a potential flow and/or tower shadow model based on the work of Powles [36][56]. The structural dynamics is modelled by a combined modal and multibody dynamics formulation. When applied to three-bladed rotors, a maximum of 24 degrees of freedom can be simulated. These include among others a mode for drivetrain torsion, six representing 1st & 2nd blade flapwise modes and three for the 1st blade edgewise modes. The blade torsion modes are not included however [35].

FAST has also upgraded from the earlier structural dynamics model ElastoDyn to the new one called BeamDyn. BeamDyn allows for full geometric non-linearity and large deflections [54]. It makes possible to capture torsion, shear and axial deformations and includes effects of anisotropic composite material couplings (such as bending-torsion coupling) [54]. This is a significant upgrade over the Euler-Bernoulli beam used in ElastoDyn with no torsion, shear and axial deformations and only able to capture small deformations. One drawback however is that it is not possible to linearize using BeamDyn thus limiting its applicability to frequency domain analysis.

HAWCStab HAWCStab is an aero-servo-elastic stability simulation tool for design of HAWTs which has the capability to linearize about a steady state operating point. HAWCStab was originally developed at the Risø National Laboratory, and later evolved into HAWCStab2 at the Department of Wind Energy of the Technical University of Denmark [26][49]. The main upgrade is that the new version is based on a non-linear co-rotational formulation for the kinetics [27].

An unsteady BEM model with four states per node is used to model the aerodynamics [27]. The states represent the unsteady effect of shed vorticity on the wake through Jones's approximation to Wagner's function [20], dynamic stall using a Beddoes-Leishman type dynamic stall model and dynamic inflow [27]. A parabolic distribution of airfoil forces is assumed for each element requiring three nodes per element [27]. The structure which is divided into three sub-structures : the tower, nacelle (including the driveshaft) and blades is modelled using a finite element discretization of non-linear two-node Timoshenko beam elements [27]. This code can model large deformations and includes bending-torsion coupling as well [27].

FOCUS6 FOCUS6 is an integrated, modular tool for rotor design of HAWTs with a user friendly GUI and post processing functionality developed by Knowledge Center WMC in the Netherlands [66]. It comprises two main programs - Program for Horizontal Axis Wind Turbine Analysis and Simulation (PHATAS) for non-linear time domain analysis and load calculations, and Blademode (developed by ECN) for frequency domain analysis of an individual blade [30]. In PHATAS wave loading on the tower can be added thus extending its applicability to both onshore and offshore wind turbines [43].

PHATAS uses a BEM model with standard semi-empirical corrections for heavily loaded rotors and blade tip/root loss. There are modifications for rotor yaw and blade-tower interaction, extensions for unsteady phenomena of dynamic inflow and dynamic stall based on the heuristic model of Snel [61]. The wind turbine structure is modelled as finite beam elements including torsional and bending degrees of freedoms [43]. Craig-Bampton sub-structuring is implemented for the tower [43]. Blademode models a single blade using a finite element beam model with torsional and transverse shear flexibility [42]. Bending-torsion coupling terms are included but coriolis acceleration terms are excluded [42]. The user has a choice of aerodynamic model between BEM and a vortex wake model [42]. A limitation of this program is that only the collective modes can be obtained by specifying the tower fore-aft flexibility and shaft torsion as edge constraints [42]. The asymmetric modes cannot be obtained [42].

3

Description of model

This chapter provides a concise description of the aeroelastic model used in this thesis. Based on the study of state-of-the-art aeroelastic models in Chapter 2, a brief overview of the limitations of existing codes is presented followed by a list of desired characteristics for an aeroelastic model developed for application to MOD-CMS. The structural dynamics and aerodynamics models which form the backbone of this aeroelastic model are described in some detail. Finally we conclude with a mathematical formulation for the unified aeroelastic model.

3.1. Limitations of state-of-the-art aeroelastic models

The advantages and limitations of the available aerodynamic and structural models were presented in Chapter 2. We have also obtained an overview into the defining features of state-of-the-art aeroelastic tools for wind turbines. Some of the limitations encountered in these tools are:

- While all aeroelastic codes are built to capture large rigid body motions, most are not adapted to capture large deformations and rotations. The small deformation assumption commonly utilized is suspect in the wake of increasingly large, flexible wind turbine blades [57]. It could possibly lead to inaccuracies in prediction of aerodynamic power, loads and aeroelastic instabilities [2].
- Another drawback, somewhat originating from the small deformation assumption, is that many codes apply the aerodynamic forces to the undeformed structure and do not update the aerodynamic coordinate systems as the blade deforms again leading to inaccurate results particularly for large, flexible wind turbine blades [57].
- Structural models of aeroelastic codes do not necessarily include anisotropic composite material coupling terms such as bend-twist coupling in the equations of motion. This has an effect on aeroelastic instability prediction. For instance, blade edgewise bending and torsion coupling, which causes the blade to twist and has effect on the flutter limits [2].
- Many aeroelastic codes do not allow for specifying the location of elastic axis and center of mass offset from the reference line of a beam element. This detail is especially relevant in the context of codes which include torsional degrees of freedom for blades [9].
- Some linearized codes may also exclude non-linear effects such as centrifugal stiffening and coriolis forces from the loading on the blades.
- Aeroelastic codes, with sufficient level of detail, are not always computationally efficient and fast enough for running time-domain simulations in real time as required for application such as MOD-CMS.

3.2. Desired model characteristics

A model required for application to MOD-CMS, in order to run time-domain simulations in real time and to design a controller and state observer for wind turbines being monitored, shares some general characteristics with other state-of-the-art models but also has some specific requirements.

A linear state space formulation is preferred because this is mathematically suited to control design applications. The state space is modular in nature making it ideal for dealing with multi-physics problems like aeroelasticity. It offers the possibility of appending other physics models such as a controller, electric or hydrodynamic model to the main aeroelastic model without having to modify it drastically. It also reduces the order of the system to a first-order differential equation, making it simpler to handle and time-integrate the system. A linear model has the added advantage of performing reasonably accurate and fast frequency domain calculations for aeroelastic stability analysis and stochastic load response analysis. Cross & Ma [14] have underscored the importance of an accurate linear model for model-based condition monitoring since the whole approach depends on detecting differences between model-predicted outputs and measured outputs from an operational wind turbine [14]. Errors due to modelling as well as sensor measurements ought to be minimized.

Based on the discussion in Chapter 2 we can conclude that a quasi-steady BEM model combined with semi-empirical models for dynamic inflow, circulation lag, dynamic stall and yawed flow gives a good trade-off between computational speed and accuracy of prediction of loads. For the structural dynamics, it is necessary to superimpose the large rigid body motion at the joints (multi-body dynamics) with the possibly large elastic deformations and rotations of the corresponding sub-structures of the wind turbine (FEM). For purposes of aeroelastic stability analysis, the model must include degrees of freedom for both bending and torsion of the blades and the relevant coupling terms. Additionally, different blade loadings such as centrifugal, coriolis and gyroscopic forces must be accounted for in the equations of motion. The Craig-Bampton method can be implemented to partition the system in terms of its constrained and independent degrees of freedom. Thereafter, modal reduction can be applied to achieve a reduced-order system. A suitable kinematic formulation should be chosen such that the body and aerodynamic reference coordinate frames follow the deformations of the sub-structures and blades respectively.

3.3. Model selection

A summary of specific characteristics that are required to be present in an aeroelastic code to be employed in MOD-CMS has been presented in Section 3.2. While it is possible to develop an entirely new model based on these characteristics, it was felt more appropriate to choose an existing (or perhaps under development) aeroelastic code, and adapt it to our specific needs.

STAS WPP (State Space Analysis of Wind Power Plants) is an open-source aero-hydro-servo-elastic tool in the Matlab/Octave environment for design and optimization of wind turbines developed by Karl Merz for SINTEF Energy Research, Norway [48]. Since this is a modular tool, it is possible to isolate and analyze only the aeroelastic module in detail. The aeroelastic model is a linear, state space representation specifically developed for frequency-domain analysis of HAWTs [48]. A special feature of this code is the high-precision linearization which is appropriate for applications such as optimization, Newton-Raphson method to calculate steady state point, aeroelastic stability analysis and also for other applications of linear systems such as controller design [48]. To this end it uses complex step derivatives and a corotational kinematic formulation which updates the body reference frames as the wind turbine deforms [48]. The code, however, is not optimized for running time-domain simulations so this thesis builds upon the aeroelastic module of the STAS WPP to implement computationally efficient time marching simulations. The following sections explain in greater detail the general features of this aeroelastic model, first for the structural dynamics and then for the aerodynamics.

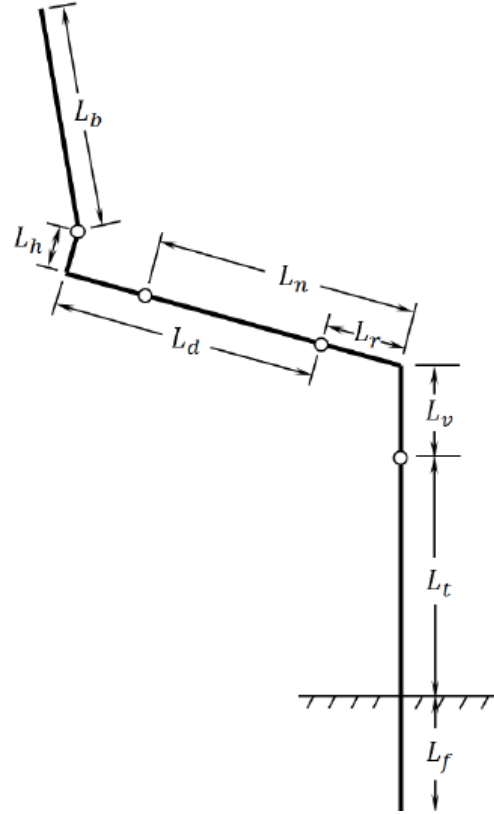


Figure 3.1: Skeletal sketch of general wind turbine system modelled in STAS Aeroelastic [46]. Note only one blade has been shown here.

3.4. Structural Dynamics

The structural dynamics model employs a combined multi-body, finite element beam representation with a corotational formulation for the kinetics [48]. The wind turbine itself is divided into the following structural components: foundation, tower, nacelle, driveshaft and blades [48]. Each of these components is modelled as a body. Each body in turn is composed of 1-D beam finite elements with two nodes per element and six degrees of freedom per node. The bodies in turn are linked together through joints. The large rigid body rotations of the joints are combined with the elastic deformations of the elements to yield the structural motion and displacements. Note that in this formulation large elastic deformations are also allowed. A skeletal sketch of the wind turbine system of interest here is shown in Figure 3.1. All joints in the system are represented by white dots in Figure 3.1. These include the yaw bearing, nacelle and driveshaft joints (front and rear bearing) and the pitch bearings. It is worth noting that the nacelle and driveshaft overlap between the front and rear bearing.

3.4.1. Notation and coordinate system

It is important to define a convention for the notations used while describing the structural model. Firstly, all vectors and matrices are represented in boldface. As we shall see, a multiplicity of coordinate systems are defined so it is also important to specify in which reference frame vectors are defined and how they are measured. To illustrate this notation consider the vector $\mathbf{r}_{/g}^B$. Here the superscript refers to the local body coordinate system (B) with respect to which $\mathbf{r}_{/g}^B$ is defined while the subscript, which necessarily contains a backslash, denotes the global coordinate system (g) with respect to which $\mathbf{r}_{/g}^B$ is actually measured. At times we deal with spatial components of vectors. These are represented by a subscript outside a parentheses.

Coming to the coordinate systems, a number of different frames are used in the structural dynamics. These are identical to the ones defined by Merz [48]. Broadly speaking, there is a global reference frame, local body

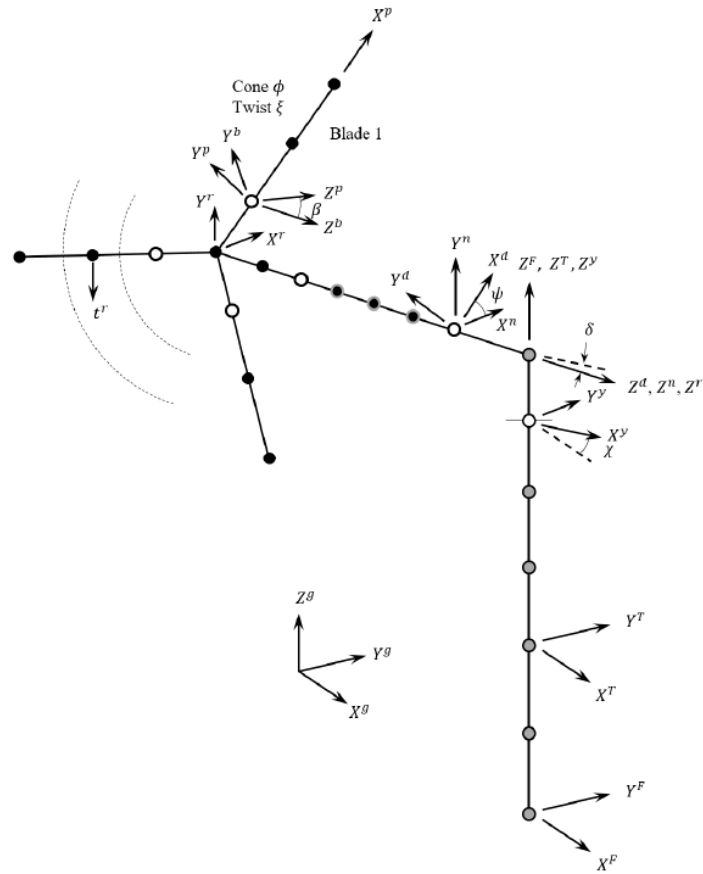


Figure 3.2: Coordinate systems used in the wind turbine model of STAS Aeroelastic [48]. Structure is modelled as finite elements, and dots represent nodes. Note that white dots represent joints.

reference frames, and element section and nodal reference frames. With the exception of the element coordinate systems, the global and body reference frames are shown in Figure 3.2. The global coordinate system will be located at the level of the tower-foundation rigid joint with the X^g pointing downwind in the direction of the undisturbed ocean surface and the Z^g pointing upwards towards the sky through the centre of the undeformed tower. Aligned identically to the global coordinate system for the undeformed state, we have the foundation and tower coordinate systems located at the base of the foundation and base of the tower respectively. The yaw coordinate system, located appropriately at the yaw bearing, points in the same direction as the global coordinate system for zero yaw but is rotated about the $Z^g = Z^y$ by the yaw angle when the rotor yaws. For the nacelle coordinate system, attached to the rear bearing, Z^n axis points in the direction of the driveshaft, or in other words it points in the direction of the X^y axis rotated by the driveshaft tilt angle (δ) about the X^n axis. Then you have the driveshaft coordinate system which is oriented with the nacelle coordinate system for zero azimuthal angle, but will follow the rotation of the driveshaft. There is a rotor plane coordinate system aligned with the nacelle coordinate system but with its origin at the center of the rotor hub. Related to the rotor plane coordinate system are the three hub coordinate systems (one for each blade). It is identical to the rotor plane coordinate system for the 1st blade, but is offset by angles of 120° and 240° about Z^d axis for the 2nd and 3rd blades respectively. Rotate the hub coordinate systems about $Y^h = Y^b$ axis by the cone angle (ϕ_c) we get the blade coordinate system. Similarly, the blade pitch coordinate systems originate from the hub coordinate systems by simply rotating it by the negative of the pitch angle (β) about the $X^h = X^p$ axis.

3.4.2. Non-linear finite element representation

A 1-D beam element with two nodes is associated with twelve degrees of freedom \mathbf{w} , that is, six for each node (three displacements and three rotations) [48]. The whole essence of the finite element method is to describe each element through its mass (\mathbf{m}_e) and stiffness matrices (\mathbf{k}_e). Note we do not deal with the damping matrices (\mathbf{c}_e) at this point. They will be described later in terms of the modal damping. So the kinetic energy of an element with volume \mathcal{V} , can be defined in terms of the volume integral of the particle velocities and mass distribution [47].

$$E_K = \frac{1}{2} \int_{\mathcal{V}} \rho \frac{d\mathbf{r}^T}{dt} \frac{d\mathbf{r}}{dt} d\mathcal{V} \quad (3.1)$$

Here, $\mathbf{r} = [r_x \ r_y \ r_z]^T$ is the elemental position vector from the the origin of the element coordinate system to a point mass belonging to the element [47]. One way to obtain \mathbf{m}_e is to manipulate the expression for kinetic energy to the following form [47]:

$$E_K = \frac{1}{2} \rho \frac{d\mathbf{g}^T}{dt} \mathbf{m}_e \frac{d\mathbf{g}}{dt} \quad (3.2)$$

Now, the finite element discretization calculates the values of the displacements and rotations at the node points but to calculate the beam reference line displacements and rotations within the element subspace shape functions which approximate the deformations and rotations must be employed. For standard beam elements undergoing planar bending we write the components of the beam reference line displacements \mathbf{W} and rotations $\boldsymbol{\theta}$ in terms of the nodal displacements and rotations \mathbf{g} , denoted componentwise with a reference to the node in the subscript (such as $w_{x,1}$) [47].

$$\begin{aligned}
W_x &= \left(1 - \frac{x}{L}\right) g_{x,1} + \frac{x}{L} g_{x,2} \\
W_y &= \left(1 - 3\frac{x^2}{L^2} + 2\frac{x^3}{L^3}\right) g_{y,1} + \left(x - 2\frac{x^2}{L} + \frac{x^3}{L^2}\right) \theta_{z,1} + \left(3\frac{x^2}{L^2} - 2\frac{x^3}{L^3}\right) g_{y,2} + \left(-\frac{x^2}{L} + \frac{x^3}{L^2}\right) \theta_{z,2} \\
W_z &= \left(1 - 3\frac{x^2}{L^2} + 2\frac{x^3}{L^3}\right) g_{z,1} - \left(x - 2\frac{x^2}{L} + \frac{x^3}{L^2}\right) \theta_{y,1} + \left(3\frac{x^2}{L^2} - 2\frac{x^3}{L^3}\right) g_{z,2} + \left(\frac{x^2}{L} - \frac{x^3}{L^2}\right) \theta_{y,2} \\
\vartheta_x &= \left(1 - \frac{x}{L}\right) \theta_{x,1} + \frac{x}{L} \theta_{x,2} \\
\vartheta_y &= -\frac{\partial W_z}{\partial x} = \left(6\frac{x}{L^2} - 6\frac{x^2}{L^3}\right) g_{z,1} + \left(1 - 4\frac{x}{L} + 3\frac{x^2}{L^2}\right) \theta_{y,1} + \left(-6\frac{x}{L^2} + 6\frac{x^2}{L^3}\right) g_{z,2} + \left(-2\frac{x}{L} + 3\frac{x^2}{L^2}\right) \theta_{y,2} \\
\vartheta_z &= \frac{\partial W_y}{\partial x} = -\left(6\frac{x}{L^2} - 6\frac{x^2}{L^3}\right) g_{y,1} + \left(1 - 4\frac{x}{L} + 3\frac{x^2}{L^2}\right) \theta_{z,1} - \left(-6\frac{x}{L^2} + 6\frac{x^2}{L^3}\right) g_{y,2} + \left(-2\frac{x}{L} + 3\frac{x^2}{L^2}\right) \theta_{z,2}
\end{aligned} \tag{3.3}$$

Now representing the beam reference line displacements and rotations in terms of the shape function $S(x)$ we simply get [47],

$$\mathbf{W}(x, t) = \mathbf{S}(x)\mathbf{g}(t) \tag{3.4}$$

The Euler-Bernoulli beam assumption then leads us to express the velocity of points lying on the beam element in terms of the beam reference line displacements and rotations as follows [47]:

$$\begin{aligned}
\frac{dr_x}{dt} &= \frac{dW_x}{dt} + r_z \frac{d\vartheta_y}{dt} - r_y \frac{d\vartheta_z}{dt} \\
\frac{dr_y}{dt} &= \frac{dW_y}{dt} - r_z \frac{d\vartheta_x}{dt} \\
\frac{dr_z}{dt} &= \frac{dW_z}{dt} + r_y \frac{d\vartheta_x}{dt}
\end{aligned} \tag{3.5}$$

This can, for uniform beam elements, be expressed in terms of a vector $\mathbf{R}(y, z)$ containing the y & z components of the local position vector [47].

$$\frac{d\mathbf{r}}{dt} = \mathbf{R}(y, z) \frac{d\mathbf{W}}{dt}(x, t) \tag{3.6}$$

Substituting Eqn. 3.6 and Eqn. 3.4 into Eqn. 3.1 we get an updated expression for the kinetic energy of the element in terms of the nodal displacements cum rotations and shape function [47].

$$E_K = \frac{1}{2} \frac{d\mathbf{g}^T}{dt} \int_L \mathbf{S}^T \left(\int_A \rho \mathbf{R}^T \mathbf{R} dA \right) \mathbf{S} dx \frac{d\mathbf{g}}{dt} \tag{3.7}$$

Comparing Eqn. 3.7 with Eqn. 3.2 we get [47],

$$\mathbf{m}_e = \int_L \mathbf{S}^T \left(\int_A \rho \mathbf{R}^T \mathbf{R} dA \right) \mathbf{S} dx \tag{3.8}$$

The mass matrix is 12×12 , with the integral in the parentheses describing the inertia terms so we call it the inertia matrix. When the beam reference line passes through the center of mass, then the inertia matrix is

purely diagonal with the torsional inertia and rotational inertia in bending being the important terms lying on this diagonal. The off-diagonal terms come into play when the beam reference line and centre of mass are offset. This offset can be thought to manifest in the form of an additional 12×12 matrix dependent on the offset distance y_c , which is added to the original mass matrix with no offset [47].

A similar procedure is adopted to derive \mathbf{k}_e by manipulating the potential energy into the form given below [47]:

$$E_P = \frac{1}{2} \mathbf{g}^T \mathbf{k}_e \mathbf{g} \quad (3.9)$$

The potential energy stored in an element of volume \mathcal{V} , expressed in terms of the vector of stress $\boldsymbol{\sigma}$ and vector of strains $\boldsymbol{\epsilon}$, is generally defined as [47]:

$$E_P = \int \int_{\mathcal{V}} \boldsymbol{\sigma}^T d\boldsymbol{\epsilon} dV \quad (3.10)$$

For an elastic material satisfying $\boldsymbol{\sigma} = \mathbf{E}\boldsymbol{\epsilon}$ and when \mathbf{E} is symmetric, this can be rewritten as [47]:

$$E_P = \frac{1}{2} \int_{\mathcal{V}} \boldsymbol{\epsilon}^T \mathbf{E} d\boldsymbol{\epsilon} dV \quad (3.11)$$

Let $\mathbf{u} = [u_x \ u_y \ u_z]^T$ represent the displacements of points in an element. For elastic materials, the relationship between stress and strain is given as [47]:

$$\begin{aligned} \epsilon_x &= \frac{\partial u_x}{\partial x}, \epsilon_y = \frac{\partial u_y}{\partial y}, \epsilon_z = \frac{\partial u_z}{\partial z} \\ \gamma_{xy} &= \frac{\partial u_x}{\partial y} + \frac{\partial u_y}{\partial x}, \gamma_{xz} = \frac{\partial u_x}{\partial z} + \frac{\partial u_z}{\partial x}, \gamma_{yz} = \frac{\partial u_y}{\partial z} + \frac{\partial u_z}{\partial y} \end{aligned} \quad (3.12)$$

The material point displacements can be related to the reference line displacements and rotations \mathbf{W} and $\boldsymbol{\Theta}$ in a similar way to Eqn. 3.6, so we have [47]:

$$\mathbf{u} = \mathbf{R}(y, z) \mathbf{W}(x, t) \quad (3.13)$$

Substituting in Eqn. 3.12 we get a direct relation between the strains and the beam reference line displacements [47],

$$\begin{aligned} \epsilon_x &= \frac{\partial W_x}{\partial x} + r_z \frac{\partial \vartheta_y}{\partial x} - r_y \frac{\partial \vartheta_z}{\partial x}, \epsilon_y = 0, \epsilon_z = 0 \\ \gamma_{xy} &= -\vartheta_z + \frac{\partial W_y}{\partial x} - r_z \frac{\partial \vartheta_x}{\partial x} = -r_z \frac{\partial \vartheta_x}{\partial x} \\ \gamma_{xz} &= \vartheta_y + \frac{\partial W_z}{\partial x} + r_y \frac{\partial \vartheta_x}{\partial x} = r_y \frac{\partial \vartheta_x}{\partial x} \\ \gamma_{yz} &= 0 \end{aligned} \quad (3.14)$$

In general, the strains can be written as follows after applying Eqn. 3.4:

$$\boldsymbol{\epsilon} = \begin{Bmatrix} \epsilon_x \\ \gamma_{xy} \\ \gamma_{xz} \end{Bmatrix} = \mathbf{D}(y, z) \frac{\partial \mathbf{W}}{\partial x}(x, t) = \mathbf{D}(y, z) \frac{\partial \mathbf{S}}{\partial x} \mathbf{g}(t) \quad (3.15)$$

Substituting Eqn. 3.15 into Eqn. 3.11 we can get an expression for the potential energy in terms of the shape function, and the nodal displacements and rotation [47]:

$$E_P = \frac{1}{2} \mathbf{g}^T \int_L \frac{\partial \mathbf{S}^T}{\partial x} \left(\int_A \mathbf{D}^T \mathbf{E} \mathbf{D} dA \right) \frac{\partial \mathbf{S}}{\partial x} dx \mathbf{g} \quad (3.16)$$

Comparing Eqn. 3.16 with Eqn. 3.9 we can get the stiffness matrix as follows [47]:

$$\mathbf{k}_e = \int_L \frac{\partial \mathbf{S}^T}{\partial x} \left(\int_A \mathbf{D}^T \mathbf{E} \mathbf{D} dA \right) \frac{\partial \mathbf{S}}{\partial x} dx \quad (3.17)$$

The stiffness matrix is 12×12 . Again the stiffness terms are basically contained in the integral in the parentheses which is 6×6 . On the diagonal it contains terms related to the axial, torsional and bending stiffness. Off-diagonal terms are zero for symmetric, isotropic sections. If the material involves axial-shear deformation coupling, then the corresponding off-diagonal terms are activated [47].

A corotational formulation, as briefly discussed in Chapter 2, is used to describe the kinematics and to update the mass and stiffness matrices to the deformed positions and orientations [48]. Three rotational parameters in the exponential map convention, as discussed in Chapter 2, describe the orientation of a node [48]. These parameters $(\theta_b^a)_x, (\theta_b^a)_y, (\theta_b^a)_z$ encode an axis of rotation, expressed in the "a" frame, and an angle of rotation $\theta = \sqrt{[(\theta_b^a)_x]^2 + [(\theta_b^a)_y]^2 + [(\theta_b^a)_z]^2}$ about this axis [48]. A rotation of coordinate system "a" by angle θ to give the orientation of coordinate system "b", in coordinates of "a" frame, is represented by \mathbf{T}_b^a [48]. Furthermore, the relationship between exponential map parameters θ_b^a , and transformation matrix \mathbf{T}_b^a is given as [48]:

$$\mathbf{T}_b^a = \exp(\Theta_b^a) \quad (3.18)$$

where Θ_b^a (Eqn. 2.54), is defined as the spin of θ_b^a [48].

$$\Theta_b^a = \ln \mathbf{T}_b^a = \begin{bmatrix} 0 & -(\theta_b^a)_z & (\theta_b^a)_y \\ (\theta_b^a)_z & 0 & -(\theta_b^a)_x \\ -(\theta_b^a)_y & (\theta_b^a)_x & 0 \end{bmatrix} \quad (3.19)$$

Restating Eqn. 2.55 we get,

$$\mathbf{T}_b^a = \exp \Theta_b^a = \mathbf{I}_{3 \times 3} + \frac{\sin \theta}{\theta} \Theta_b^a + \frac{1 - \cos \theta}{\theta^2} (\Theta_b^a)^2 \quad (3.20)$$

The above equation leads to a singularity when $\theta \rightarrow 0$. An alternative equation is then utilized [48].

$$\mathbf{T}_b^a \approx \mathbf{I}_{3 \times 3} + \left(1 - \frac{\theta^2}{6} + \frac{\theta^4}{120}\right) \Theta_b^a + \left(\frac{1}{2} - \frac{\theta^2}{24} + \frac{\theta^4}{720}\right) (\Theta_b^a)^2 \quad (3.21)$$

A general formula for the partial derivative $\frac{\partial \mathbf{T}_b^a}{\partial \theta_i}$, obtained from [21], is as follows:

$$\frac{\partial \mathbf{T}_b^a}{\partial \theta_i} = \frac{\theta_i \Theta_b^a + \text{spin}[\boldsymbol{\theta} \times (\mathbf{I}_{3 \times 3} - \mathbf{T}_b^a) \mathbf{e}_i]}{\boldsymbol{\theta}^T \boldsymbol{\theta}} \mathbf{T}_b^a \quad (3.22)$$

where, \mathbf{e}_i is the i^{th} vector of the standard basis of \mathbb{R}^3 . The second order derivative $\frac{\partial^2 \mathbf{T}_b^a}{\partial \theta_i \partial \theta_j}$ and third order

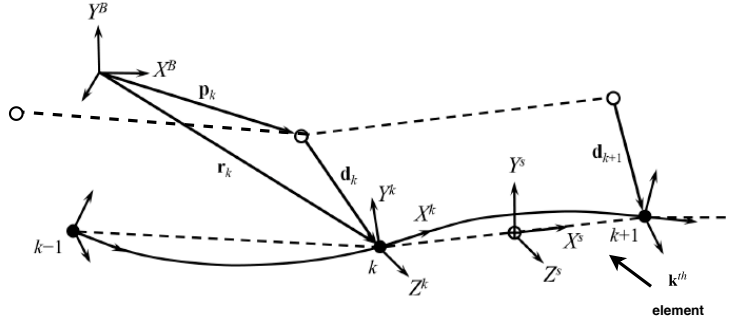


Figure 3.3: Illustration of deformed beam element with respect to undeformed orientation (dashed line). Adapted from [48].

derivative $\frac{\partial^3 \mathbf{T}_b^a}{\partial \theta_i \partial \theta_j \partial \theta_k}$ can be calculated using the chain rule of differentiation. For sake of brevity, the equations are left out of this report, but can be found in [48].

The above information is utilized to first define an element section coordinate system which determines the rigid body motion. The origin of this coordinate system is situated midway of the line connecting the nodes which also happens to be the direction of the X^s axis. The orientation of the Y^s and Z^s axes is required to be a best fit of the corresponding axes of the nodal coordinate systems situated on the adjacent nodes. For the undeformed structure, it is assumed that the undeformed nodal coordinate system, denoted as $n0$, for the $(k+1)^{\text{th}}$ node is aligned with the undeformed element section coordinate system, denoted as $s0$, of the k^{th} element. This leads to [48]:

$$\mathbf{T}_{n0,k+1}^{s0,k} = \mathbf{I}_{3 \times 3}, \quad \mathbf{T}_{n0,k}^{s0,k} = \mathbf{T}_{s0,k-1}^{s0,k} = \mathbf{T}_B^{s0,i} \mathbf{T}_{s0,i-1}^B \quad (3.23)$$

Looking at Fig. 3.3, we can define the deformed element section coordinate system knowing that the element origin is given by $(\mathbf{r}_k^B + \mathbf{r}_{k+1}^B)/2$. The unit vector along the x-axis is then given as [48]:

$$\mathbf{x}_s^B = \frac{\mathbf{r}_{k+1}^B - \mathbf{r}_k^B}{|\mathbf{r}_{k+1}^B - \mathbf{r}_k^B|} \quad (3.24)$$

An intermediate unit vector $\mathbf{y}_{s'}^B$ is defined as the average of the second columns (denoted by a subscript outside parentheses in transform) of the transforms from the deformed nodal coordinate systems to the undeformed element section coordinate system.

$$\mathbf{y}_{s'}^B = \frac{1}{2} \mathbf{T}_{s0,k}^B \left[\left(\mathbf{T}_{n,k}^{s0,k} \right)_2 + \left(\mathbf{T}_{n,k+1}^{s0,k} \right)_2 \right] \quad (3.25)$$

Accordingly, the Y^s and Z^s axes are defined as follows through the vectors, \mathbf{y}_s^B and \mathbf{z}_s^B [48]:

$$\mathbf{z}_s^B = \frac{\mathbf{x}_s^B \times \mathbf{y}_{s'}^B}{|\mathbf{x}_s^B \times \mathbf{y}_{s'}^B|}, \quad \mathbf{y}_s^B = \frac{\mathbf{z}_s^B \times \mathbf{x}_s^B}{|\mathbf{z}_s^B \times \mathbf{x}_s^B|} \quad (3.26)$$

Having chosen a rotation parameterization convention and defined the element coordinate system, it is now possible to define the undeformed position and orientation of an element node as follows:

$$\mathbf{P}_k = \begin{bmatrix} \mathbf{p}_{k0/B0}^{B0} \\ \boldsymbol{\xi}_{s0}^{B0} \end{bmatrix} \quad (3.27)$$

where $\mathbf{p}_{k0/B0}^{B0}$ stands for the undeformed nodal position of the k^{th} node relative to the body coordinate system origin. ξ_{s0}^{B0} defines through \mathbf{T}_{s0}^{B0} the orientations of the beam section at each node [48]. The position and orientation are defined by the input turbine geometry and do not change with time. For a deformed structure, the nodal position and orientation of an element node (henceforth called the pose) is additionally defined by the displacement vector relative to the undeformed nodal position named $\mathbf{d}_{k/k0}^B$, and the rotation parameter θ_k^{k0} coding from the undeformed to the deformed nodal orientation. The pose also constitutes the degrees of freedom for the node as shown below[48].

$$\mathbf{q}_k = \begin{bmatrix} \mathbf{d}_{k/k0}^B \\ \theta_k^{k0} \end{bmatrix} \quad (3.28)$$

Also, for each body a reference node is defined which is basically the node closest to the ground. The coordinates for this node are defined relative to the global coordinate system, and the pose relative to the undeformed body coordinate system. For the reference node of a body B we have [48]:

$$\mathbf{p}_B = \begin{bmatrix} \mathbf{O}_{B0/g}^g \\ \Phi_{B0}^g \end{bmatrix}, \quad \mathbf{q}_B = \begin{bmatrix} \mathbf{O}_{B/B0}^g \\ \phi_B^{B0} \end{bmatrix} \quad (3.29)$$

Note that in the non-linear corotational formulation, the combined rigid body and elastic displacements and rotations are stored. The rigid and elastic parts are separated out when the need arises. The elastic rotations, denoted by ζ , are extracted from \mathbf{T}_n^s as follows [48]:

$$\zeta_{n/s}^n = \frac{1}{2} \begin{bmatrix} (\mathbf{T}_{n,k}^s)_{32} - (\mathbf{T}_{n,k}^s)_{23} \\ (\mathbf{T}_{n,k}^s)_{13} - (\mathbf{T}_{n,k}^s)_{31} \\ (\mathbf{T}_{n,k}^s)_{21} - (\mathbf{T}_{n,k}^s)_{12} \end{bmatrix} \quad (3.30)$$

where [48] gives,

$$\mathbf{T}_n^s = \mathbf{T}_B^s \mathbf{T}_{s0}^B \mathbf{T}_{n0}^{s0} \mathbf{T}_n^{n0} \quad (3.31)$$

Now, the definition of the element section coordinate system restricts the elastic deformation (denoted as δ) only to the axial direction and this is extracted as follows:

$$\delta_x = L - L_0 = (r_{k+1}^s)_x - (r_k^s)_x - L_0 \quad (3.32)$$

$$\delta_x = [1 \quad 0 \quad 0] [\mathbf{T}_B^s (\mathbf{p}_2^B + \mathbf{d}_2^B - \mathbf{p}_1^B - \mathbf{d}_1^B) - \mathbf{T}_B^{s0} (\mathbf{p}_2^B - \mathbf{p}_1^B)]$$

Additionally, the time derivate of the elastic rotation is needed in the equation of motion. This is calculated as follows [48]:

$$\frac{d\zeta_{n/s}^n}{dt} = \frac{\partial \zeta_{n/s}^n}{\partial (\mathbf{T}_n^s)_{ij}} \frac{\partial (\mathbf{T}_n^s)_{ij}}{\partial q_k} \frac{dq_k}{dt} \quad (3.33)$$

where [48],

$$\frac{\partial \mathbf{T}_n^s}{\partial q_k} = \frac{\partial \mathbf{T}_s^B}{\partial q_k} \mathbf{T}_{s0}^B \mathbf{T}_{n0}^{s0} \mathbf{T}_n^{n0} + \mathbf{T}_B^s \mathbf{T}_{s0}^B \mathbf{T}_{n0}^{s0} \frac{\partial \mathbf{T}_n^{n0}}{\partial \theta_k} \quad (3.34)$$

For further details on how the derivatives of \mathbf{T}_s^B are calculated please refer to [48].

3.4.3. Non-Linear Equations of Motion

The non-linear equations of motion have been derived in terms of the degrees of freedom using the general Euler-Lagrange equation (Eqn. 2.36) described earlier. For the detailed derivation please refer to [48]. This section provides a concise derivation for sake of completeness. The procedure is to first define the kinetic and potential energy for a single element, and then obtain the derivatives stated in Eqn. 2.36. The general equation thus obtained for one element can be extended to the entire structure.

The position of a node, with respect to the global coordinate system, is given as:

$$\mathbf{r}_{n/g}^g = \mathbf{O}_{B0/g}^g + \mathbf{O}_{B/B0}^g + \mathbf{T}_B^g (\mathbf{p}_{n0/B}^B + \mathbf{d}_{n/n0}^B) \quad (3.35)$$

This can be represented, in terms of the full set of \mathbf{P} and \mathbf{q} , as follows:

$$\mathbf{r}_{n/g}^g = \begin{bmatrix} \mathbf{I}_{3 \times 3} & 0 & \mathbf{I}_{3 \times 3} & 0 \\ 0 & \mathbf{I}_{3 \times 3} & \mathbf{T}_B^g & 0 \\ 0 & 0 & 0 & \mathbf{I}_{3 \times 3} \end{bmatrix} \left(\begin{bmatrix} \mathbf{O}_{B/B0}^g \\ \Phi_{B0}^B \\ \mathbf{d}_{n/n0}^B \\ \theta_n^{n0} \end{bmatrix} + \begin{bmatrix} \mathbf{O}_{B0/g}^g \\ \Phi_{B0}^g \\ \mathbf{p}_{n0/B}^B \\ \xi_{n0}^B \end{bmatrix} \right) \quad (3.36)$$

The above equation can be rewritten concisely in terms of $\mathbf{q} = \begin{bmatrix} \mathbf{q}_B \\ \mathbf{q}_n \end{bmatrix}$ and $\mathbf{P} = \begin{bmatrix} \mathbf{P}_B \\ \mathbf{P}_n \end{bmatrix}$ [48]:

$$\mathbf{r}_{n/g}^g = \mathbf{A}_n \tilde{\mathbf{T}}_B^g (\mathbf{q} + \mathbf{P}) \quad (3.37)$$

Taking the time derivative of Eqn. 3.37 we get the global linear velocity as follows [48]:

$$\mathbf{v}_{n/g}^g = \frac{d\mathbf{r}_{n/g}^g}{dt} = \mathbf{A}_n \tilde{\mathbf{T}}_B^g \frac{d\mathbf{q}}{dt} + \mathbf{A}_n \frac{d\tilde{\mathbf{T}}_B^g}{dt} (\mathbf{q} + \mathbf{P}) \quad (3.38)$$

Now for obtaining the global angular velocity of a node, the transform \mathbf{T}_n^g is utilized. Taking the derivative of Eqn. 3.19 we get [48],

$$\mathbf{S}_{n/g}^g = \begin{bmatrix} 0 & -(\omega_{n/g}^g)_z & (\omega_{n/g}^g)_y \\ (\omega_{n/g}^g)_z & 0 & -(\omega_{n/g}^g)_x \\ -(\omega_{n/g}^g)_y & (\omega_{n/g}^g)_x & 0 \end{bmatrix} = \frac{d\mathbf{T}_n^g}{dt} \mathbf{T}_n^g \quad (3.39)$$

where $\mathbf{T}_n^g = \mathbf{T}_{B0}^g \mathbf{T}_B^{B0} \mathbf{T}_{n0}^B \mathbf{T}_n^{n0}$.

Writing Eqn. 3.39 in terms of the rotation matrices that make up \mathbf{T}_n^g and the corresponding angles that encode these matrices we obtain [48],

$$\mathbf{S}_{n/g}^g = \sum_{j=1}^3 \left[\left(\mathbf{T}_{B0}^g \frac{\partial \mathbf{T}_B^{B0}}{\partial (\Phi_B^{B0})_j} \mathbf{T}_B^{B0} \mathbf{T}_g^g \frac{d(\Phi_B^{B0})_j}{dt} \right) + \left(\mathbf{T}_{B0}^g \mathbf{T}_B^{B0} \mathbf{T}_{n0}^B \frac{\partial \mathbf{T}_n^{n0}}{\partial (\theta_n^{n0})_j} \mathbf{T}_{n0}^B \mathbf{T}_B^{B0} \mathbf{T}_g^g \frac{d(\theta_n^{n0})_j}{dt} \right) \right] \quad (3.40)$$

Using the following notation to simplify the above equation [48],

$$\begin{aligned} \mathbf{J}_j &= \mathbf{T}_{B0}^g \frac{\partial \mathbf{T}_B^{B0}}{\partial (\Phi_B^{B0})_j} \mathbf{T}_B^{B0} \mathbf{T}_g^{B0} \\ \mathbf{N}_j &= \mathbf{T}_{B0}^g \mathbf{T}_B^{B0} \mathbf{T}_{n0}^B \frac{\partial \mathbf{T}_n^{n0}}{\partial (\theta_n^{n0})_j} \mathbf{T}_{n0}^n \mathbf{T}_B^{n0} \mathbf{T}_{B0}^B \mathbf{T}_g^{B0} \end{aligned} \quad (3.41)$$

A relation between the spin of the rotational parameters and the angular velocity is given as follows:

$$\begin{aligned} \boldsymbol{\omega}_{n/g}^g &= \begin{bmatrix} -J_{x,23} & -J_{y,23} & -J_{z,23} \\ J_{x,13} & J_{y,13} & J_{z,13} \\ -J_{x,12} & -J_{y,12} & -J_{z,12} \end{bmatrix} \frac{d\boldsymbol{\Phi}_B^{B0}}{dt} + \begin{bmatrix} -N_{x,23} & -N_{y,23} & -N_{z,23} \\ N_{x,13} & N_{y,13} & N_{z,13} \\ -N_{x,12} & -N_{y,12} & -N_{z,12} \end{bmatrix} \frac{d\boldsymbol{\theta}_n^{n0}}{dt} \\ \boldsymbol{\omega}_{n/g}^g &= \tilde{\mathbf{J}} \frac{d\boldsymbol{\Phi}_B^{B0}}{dt} + \tilde{\mathbf{N}} \frac{d\boldsymbol{\theta}_n^{n0}}{dt} \end{aligned} \quad (3.42)$$

The above equation can be combined with Eqn. 3.38 to yield the following shorthand form [48]:

$$\begin{aligned} \begin{bmatrix} \mathbf{v}_{n/g}^B \\ \boldsymbol{\omega}_{n/g}^B \end{bmatrix} &= \mathbf{T}_{B0}^B \mathbf{T}_g^{B0} \left(\tilde{\mathbf{A}}_n \tilde{\mathbf{T}}_{B0}^g \tilde{\mathbf{T}}_B^{B0} + \mathbf{A}_n \tilde{\mathbf{T}}_{B0}^g \frac{\partial \tilde{\mathbf{T}}_B^{B0}}{\partial \mathbf{q}} (\mathbf{q} + \mathbf{P}) \right) \frac{d\mathbf{q}}{dt} \\ &= \mathbf{Q}_v(\mathbf{q}) \frac{d\mathbf{q}}{dt} \end{aligned} \quad (3.43)$$

The first derivative of \mathbf{Q}_v with respect to q_j can be obtained by using the usual chain rule of differentiation, and can be found in [48].

The velocities of the nodes of an element can now be summarized in a vector, $\mathbf{u}_e = [\mathbf{v}_{1/g}^B \quad \boldsymbol{\omega}_{1/g}^B \quad \mathbf{v}_{2/g}^B \quad \boldsymbol{\omega}_{2/g}^B]$, and subsequently the kinetic energy of the element is shown to be [48]:

$$E_K = \frac{1}{2} \mathbf{u}_e^T \mathbf{T}_s^B \mathbf{m}_e^s \mathbf{T}_B^s \mathbf{u}_e \quad (3.44)$$

Referring to the general Euler-Lagrange equation given in Eqn. 2.36, the first LHS term for the i^{th} equation of an element is computed as follows [48]:

$$\frac{\partial E_K}{\partial \dot{q}_i} = \frac{\partial \mathbf{u}_e^T}{\partial \dot{q}_i} \mathbf{m}_e^B \mathbf{u}_e \quad (3.45)$$

Taking the time derivative of $\partial E_K / \partial \dot{q}_i$ and representing in shorthand tensor notation leads to [48],

$$\begin{aligned} \frac{d}{dt} \frac{\partial E_K}{\partial \dot{q}_i} &= \left(\frac{\partial \mathbf{u}_e^T}{\partial \dot{q}_i} \mathbf{T}_s^B \mathbf{m}_e^s \mathbf{T}_B^s \frac{\partial \mathbf{u}_e}{\partial \dot{q}_j} \right) \frac{d^2 q_j}{dt^2} + \\ &\left[\frac{\partial^2 \mathbf{u}_e^T}{\partial \dot{q}_i \partial \dot{q}_j} \mathbf{T}_s^B \mathbf{m}_e^s \mathbf{T}_B^s \mathbf{u}_e + \frac{\partial \mathbf{u}_e^T}{\partial \dot{q}_i} \mathbf{T}_s^B \mathbf{m}_e^s \mathbf{T}_B^s \frac{\partial \mathbf{u}_e}{\partial q_j} + \frac{\partial \mathbf{u}_e^T}{\partial \dot{q}_i} \left(\frac{\partial \mathbf{T}_s^B}{\partial q_j} \mathbf{m}_e^s \mathbf{T}_B^s + \mathbf{T}_s^B \mathbf{m}_e^s \frac{\partial \mathbf{T}_B^s}{\partial q_j} \right) \mathbf{u}_e \right] \frac{dq_j}{dt} \end{aligned} \quad (3.46)$$

Note that the motion of each node depends on its two connected nodes and the body reference node so $\dot{\mathbf{q}}$ for a given element is a 18×1 vector. Here the notation depicts that for every i, j in q_j varies from 1 to 18. Also for any node, it is seen from Eqn. 3.43 that the derivatives in the above equation can be represented as [48]:

$$\frac{\partial \mathbf{u}_e}{\partial \dot{q}_i} = (\mathbf{Q}_v)_i, \quad \frac{\partial^2 \mathbf{u}_e}{\partial \dot{q}_i \partial q_j} = \frac{(\partial \mathbf{Q}_v)_i}{\partial q_j}, \quad \frac{\partial \mathbf{u}_e}{\partial q_i} = \frac{(\partial \mathbf{Q}_v)_i}{\partial q_i} \frac{dq}{dt} \quad (3.47)$$

The second LHS term in Eqn. 2.36 is derived to be [48]:

$$\frac{\partial E_K}{\partial q_i} = \frac{\partial \mathbf{u}_e^T}{\partial \dot{q}_i} \mathbf{T}_s^B \mathbf{m}_e^s \mathbf{T}_B^s \mathbf{u}_e + \mathbf{u}_e^T \frac{\partial \mathbf{T}_s^B}{\partial q_i} \mathbf{m}_e^s \mathbf{T}_B^s \mathbf{u}_e \quad (3.48)$$

The potential energy of the element can be expressed in terms of the elastic deformations $\boldsymbol{\mu}_e = [\delta_{x,1}^s \ 0 \ 0 \ \zeta_1^s \ \delta_{x,2}^s \ 0 \ 0 \ \zeta_2^s]$, where the total elastic extension of the element δ_x is split equally between the two nodes [48].

$$E_P = \frac{1}{2} \boldsymbol{\mu}_e^T \mathbf{k}_e^s \boldsymbol{\mu}_e \quad (3.49)$$

The term related to the potential energy in Eqn. 2.36 is then given as [48]:

$$\frac{\partial E_P}{\partial q_i} = \frac{\partial \boldsymbol{\mu}_e^T}{\partial q_i} \mathbf{k}_e^s \boldsymbol{\mu}_e \quad (3.50)$$

The energy dissipation term in the Euler-Lagrange equation comes out to be [48]:

$$\frac{\partial \dot{E}_D}{\partial \dot{q}_i} = \left(\frac{\partial \boldsymbol{\mu}_e^T}{\partial q_i} \mathbf{c}_e^s \frac{\partial \boldsymbol{\mu}_e}{\partial q_j} \right) \frac{dq_j}{dt} \quad (3.51)$$

The structural damping matrix \mathbf{c}_e^s can be specified here as some linear combination of the mass and stiffness matrices, or alternatively using modal damping [48]. The weighting coefficients, α_c and β_c , are chosen such that high frequencies in the response are selectively damped out. This leaves behind a response which can largely be determined by the low frequencies.

$$\mathbf{c}_e^s = \alpha_c \mathbf{m}_e^s + \beta_c \mathbf{k}_e^s \quad (3.52)$$

The work done by the external force \mathbf{F}_g for an infinitesimal displacement or rotation of the nodes $\delta x_{/g}^g$ is given as:

$$\delta W_g = \left(\delta x_{/g}^g \right)^T \mathbf{F}_g \quad (3.53)$$

This leads to the RHS term in Eqn. 2.36 [48],

$$\frac{\partial W_g}{\partial q_i} = \frac{\partial W_g}{\partial x_{/g}^g} \frac{\partial x_{/g}^g}{\partial q_i} = \frac{\partial (x_{/g}^g)^T}{\partial q_i} \mathbf{T}_{B0}^g \mathbf{T}_B^{B0} \mathbf{F}^B \quad (3.54)$$

Here the RHS of 3.54 is determined as the transpose of $(Q_v)_i$ (given in Eqn.3.43) multiplied by the force vector in body coordinates [48].

Having individually obtained all the terms of the Euler-Lagrange it is now possible to write the non-linear equation of motion for the entire wind turbine structure in shorthand tensor notation as follows [48]:

$$\tilde{M}_{ij} \frac{d^2 q_j}{dt^2} + (\tilde{C}_{ij} + \tilde{G}_{ij}) \frac{dq_j}{dt} - \tilde{H}_i + \tilde{K}_i = \tilde{Q}_{ij} F_j^B \quad (3.55)$$

where the individual terms, given below, are to be summed over all elements [48].

$$\begin{aligned} \tilde{M}_{ij} &= \sum \frac{\partial \mathbf{u}_e^T}{\partial \dot{q}_i} \mathbf{T}_s^B \mathbf{m}_e^s \mathbf{T}_B^s \frac{\partial \mathbf{u}_e}{\partial \dot{q}_j} \\ \tilde{G}_{ij} &= \sum \left[\frac{\partial^2 \mathbf{u}_e^T}{\partial \dot{q}_i \partial \dot{q}_j} \mathbf{T}_s^B \mathbf{m}_e^s \mathbf{T}_B^s \mathbf{u}_e + \frac{\partial \mathbf{u}_e^T}{\partial \dot{q}_i} \mathbf{T}_s^B \mathbf{m}_e^s \mathbf{T}_B^s \frac{\partial \mathbf{u}_e}{\partial \dot{q}_j} + \frac{\partial \mathbf{u}_e^T}{\partial \dot{q}_i} \left(\frac{\partial \mathbf{T}_s^B}{\partial \dot{q}_j} \mathbf{m}_e^s \mathbf{T}_B^s + \mathbf{T}_s^B \mathbf{m}_e^s \frac{\partial \mathbf{T}_B^s}{\partial \dot{q}_j} \right) \mathbf{u}_e \right] \\ \tilde{H}_i &= \sum \frac{\partial \mathbf{u}_e^T}{\partial q_i} \mathbf{T}_s^B \mathbf{m}_e^s \mathbf{T}_B^s \mathbf{u}_e + \mathbf{u}_e^T \frac{\partial \mathbf{T}_s^B}{\partial q_i} \mathbf{m}_e^s \mathbf{T}_B^s \mathbf{u}_e \\ \tilde{C}_{ij} &= \sum \frac{\partial \boldsymbol{\mu}_e^T}{\partial q_i} \mathbf{c}_e^s \frac{\partial \boldsymbol{\mu}_e}{\partial q_j} \\ \tilde{K}_i &= \sum \frac{\partial \boldsymbol{\mu}_e^T}{\partial q_i} \mathbf{k}_e^s \boldsymbol{\mu}_e \\ \tilde{Q}_i &= \sum (Q_v)_i^T \end{aligned} \quad (3.56)$$

3.4.4. Implementation of Constraints

In multibody systems such as wind turbines, the bodies are interconnected through joints to make up the system. The bodies may also undergo some relative motion at these joints depending on the type of joint. The interconnections between bodies can be described through constraint equations.

A master-slave notation is used for describing the constraints. At a joint, the body nearest to the ground is the master body and the adjoining body is called the slave body. The slave body is oriented along its axis of rotation, and this axis of rotation is defined by the nodal coordinate system attached to the outermost node on the master body which is accordingly called the master node [48]. The relative motion is depicted as a rotation of the nodal coordinate system attached to the innermost node on the slave body, called the slave node, about the axis of rotation by the joint angle [48]. The constraint equations can be expressed as a non-linear function of the pose of the bodies, and are in general given as [48]:

$$\mathbf{C}(\mathbf{q}) = 0 \quad (3.57)$$

Since the motion of the master and slave nodes is not independent, the full set of degrees of freedom \mathbf{q} can be partitioned in terms of the slave and retained degrees of freedom denoted respectively as \mathbf{q}_s and $\hat{\mathbf{q}}$. The equations of motion can fundamentally be written in terms of $\hat{\mathbf{q}}$, and \mathbf{q}_s may be obtained by solving the constraint equations.

Now for deriving the constraint equation for the tower-nacelle joint we start by recognizing that the global position of the master and slave nodes should match. So we get,

$$\mathbf{r}_{m/g}^g = \mathbf{r}_{s/g}^g \Rightarrow \mathbf{O}_{T0/g}^g + \mathbf{O}_{T/T0}^g + \mathbf{T}_{T0}^g \mathbf{T}_T^{T0} (\mathbf{p}_{m0/T}^T + \mathbf{d}_{m/m0}^T) = \mathbf{O}_{y0/g}^g + \mathbf{O}_{y/y0}^g \quad (3.58)$$

Taking the first variation with respect to the deformational degrees of freedom, and writing the slave degrees of freedom on the RHS we obtain [48],

$$\delta \mathbf{O}_{T/T0}^g + \mathbf{T}_{T0}^g \mathbf{T}_T^{T0} \delta \mathbf{d}_{m/m0}^T + \mathbf{T}_{T0}^g \frac{\partial \mathbf{T}_T^{T0}}{\partial \Phi_{T,k}^{T0}} (\mathbf{p}_{m0/T}^T + \mathbf{d}_{m/m0}^T) \delta \Phi_{T,k}^{T0} = \delta \mathbf{O}_{y/y0}^g \quad (3.59)$$

The tower and nacelle are offset by the yaw angle χ , and this leads to the rotational constraint given below [48]:

$$\begin{aligned} \mathbf{T}_{y0}^g \mathbf{T}_y^{y0} &= \mathbf{T}_{T0}^g \mathbf{T}_T^{T0} \mathbf{T}_{m0}^T \mathbf{T}_m^{m0} \mathbf{T}_y^m, \text{ or} \\ \mathbf{T}_y^g (\boldsymbol{\Phi}_T^{T0}, \boldsymbol{\theta}_m^{m0}) \mathbf{T}_y^y (\boldsymbol{\Phi}_y^{y0}) &= \mathbf{I}_{3 \times 3} \end{aligned} \quad (3.60)$$

where [48],

$$\mathbf{T}_y^m = \begin{bmatrix} 0 & 0 & 1 \\ 1 & 0 & 0 \\ 0 & 1 & 0 \end{bmatrix} \begin{bmatrix} \cos \chi & -\sin \chi & 0 \\ \sin \chi & \cos \chi & 0 \\ 0 & 0 & 1 \end{bmatrix} \quad (3.61)$$

Again, a variational form of Eqn. 3.60 is obtained as follows [48]:

$$\frac{\partial \mathbf{T}_y^g}{\partial \boldsymbol{\Phi}_{T,k}^{T0}} \mathbf{T}_y^y \delta \boldsymbol{\Phi}_{T,k}^{T0} + \frac{\partial \mathbf{T}_y^g}{\partial \boldsymbol{\theta}_{m,k}^{m0}} \mathbf{T}_y^y \delta \boldsymbol{\theta}_{m,k}^{m0} + \mathbf{T}_y^g \frac{\partial \mathbf{T}_y^y}{\partial \boldsymbol{\Phi}_{y,k}^{y0}} \delta \boldsymbol{\Phi}_{y,k}^{y0} = 0 \quad (3.62)$$

Similar constraint equations can be obtained for the other joints - foundation-tower, nacelle-driveshaft (rear bearing), driveshaft-nacelle (front bearing), driveshaft-blade (pitch bearing). Finally, the constraint equations can be summarized as [48]:

$$\mathbf{L} \delta \mathbf{q} = 0 \quad (3.63)$$

The above equation can be partitioned into \mathbf{q}_s and $\hat{\mathbf{q}}$ [48], as per the procedure developed in the Craig-Bampton method (Section 2.4.3).

$$\mathbf{L}_s \delta \mathbf{q}_s + \hat{\mathbf{L}} \delta \hat{\mathbf{q}} = 0 \Rightarrow \delta \mathbf{q}_s = -\mathbf{L}_s^{-1} \hat{\mathbf{L}} \delta \hat{\mathbf{q}} \quad (3.64)$$

In matrix form, this can be rewritten as [48]:

$$\delta \mathbf{q} = \boldsymbol{\Lambda} \delta \hat{\mathbf{q}}, \text{ such that } \boldsymbol{\Lambda} = \begin{bmatrix} \mathbf{I} \\ -\mathbf{L}_s^{-1} \hat{\mathbf{L}} \end{bmatrix} \quad (3.65)$$

Taking the first and second derivatives of Eqn. 3.63 in order to write the equations of motion purely in terms of $\hat{\mathbf{q}}$ [48],

$$\begin{aligned} \mathbf{L} \frac{d\mathbf{q}}{dt} &= 0 \\ \frac{dq_k}{dt} \frac{\partial \mathbf{L}}{\partial q_k} \frac{d\mathbf{q}}{dt} + \mathbf{L} \frac{d^2\mathbf{q}}{dt^2} &= 0 \Rightarrow \frac{dq_k}{dt} \frac{\partial \mathbf{L}}{\partial q_k} \frac{d\mathbf{q}}{dt} + \mathbf{L}_s \frac{d^2\mathbf{q}_s}{dt^2} + \hat{\mathbf{L}} \frac{d^2\hat{\mathbf{q}}}{dt^2} = 0 \end{aligned} \quad (3.66)$$

This eventually leads to the following expression for the second time derivative of \mathbf{q}_s [48]:

$$\frac{d^2\mathbf{q}_s}{dt^2} = -\mathbf{L}_s^{-1} \hat{\mathbf{L}} \frac{d^2\hat{\mathbf{q}}}{dt^2} - \mathbf{L}_s^{-1} \frac{dq_k}{dt} \frac{\partial \mathbf{L}}{\partial q_k} \frac{d\mathbf{q}}{dt} \quad (3.67)$$

It is now possible to write the non-linear equations of motion entirely in terms of the retained degrees of freedom. The vectors and matrices need to be partitioned in term of the retained and slave degrees of freedom.

The rows and/or columns representing the slave degrees of freedom are excluded, and we end up with the following equation [48]:

$$\Lambda^T \tilde{\mathbf{M}} \Lambda \frac{d^2 \hat{\mathbf{q}}}{dt^2} + (\Lambda^T \tilde{\mathbf{M}} \Gamma + \Lambda^T \tilde{\mathbf{G}} \Lambda) \frac{d \hat{\mathbf{q}}}{dt} - \Lambda^T (\tilde{\mathbf{H}} + \tilde{\mathbf{C}} + \tilde{\mathbf{K}}) = \Lambda^T \tilde{\mathbf{Q}} \mathbf{F}^B \quad (3.68)$$

where Γ absorbs the second term in Eqn. 3.67.

$$\Gamma = \begin{bmatrix} 0 \\ \mathbf{I}_s^{-1} \frac{dq_k}{dt} \frac{\partial \mathbf{L}}{\partial q_k} \Lambda \end{bmatrix} \quad (3.69)$$

This can be further written in state space form given below [48]. Note that Γ and Λ have been absorbed within the new symbols, and the new variables can be found by establishing a direct equivalence with Eqn. 3.68.

$$\begin{bmatrix} \mathbf{I} & 0 \\ 0 & \mathbf{M}(\mathbf{q}) \end{bmatrix} \frac{d}{dt} \begin{bmatrix} \hat{\mathbf{q}} \\ \dot{\hat{\mathbf{q}}} \end{bmatrix} = \begin{bmatrix} 0 & \mathbf{I} \\ 0 & -\mathbf{G}(\mathbf{q}, \dot{\mathbf{q}}) \end{bmatrix} \begin{bmatrix} \hat{\mathbf{q}} \\ \dot{\hat{\mathbf{q}}} \end{bmatrix} + \begin{bmatrix} 0 \\ \mathbf{H}(\mathbf{q}, \dot{\mathbf{q}}) - \mathbf{C}(\mathbf{q}, \dot{\mathbf{q}}) - \mathbf{K}(\mathbf{q}) - \tilde{\Gamma}(\mathbf{q}, \dot{\mathbf{q}}) \end{bmatrix} + \begin{bmatrix} 0 \\ \mathbf{Q}(\mathbf{q}) \mathbf{F} \end{bmatrix} \quad (3.70)$$

3.4.5. Linearization of structural model

The first step in the linearization is to specify an initial condition or to obtain a steady state point about which the non-linear equations can be linearized. Referring to the unconstrained equation of motion derived in Eqn. 3.55, we can apply Taylor's series expansion about a steady state point to get the linearized equation given below [48].

$$\begin{aligned} \tilde{\mathbf{M}}_0 \left. \frac{d^2 \mathbf{q}}{dt^2} \right|_0 + \tilde{\mathbf{G}}_0 \left. \frac{d \mathbf{q}}{dt} \right|_0 - \tilde{\mathbf{H}}_0 + \tilde{\mathbf{C}}_0 + \tilde{\mathbf{K}}_0 \\ + \left. \frac{\partial \tilde{\mathbf{M}}}{\partial q_i} \right|_0 \frac{d^2 \mathbf{q}}{dt^2} \Big|_0 \Delta q_i + \tilde{\mathbf{M}}_0 \frac{d^2 \Delta q_i}{dt^2} + \left. \frac{\partial \tilde{\mathbf{G}}}{\partial q_i} \right|_0 \left. \frac{d \mathbf{q}}{dt} \right|_0 \Delta q_i \\ + \left. \frac{\partial \tilde{\mathbf{G}}}{\partial \dot{q}_i} \right|_0 \left. \frac{d \mathbf{q}}{dt} \right|_0 \frac{d \Delta q_i}{dt} + \tilde{\mathbf{G}}_0 \frac{d \Delta q_i}{dt} \\ - \left. \frac{\partial \tilde{\mathbf{H}}}{\partial q_i} \right|_0 \Delta q_i - \left. \frac{\partial \tilde{\mathbf{H}}}{\partial \dot{q}_i} \right|_0 \frac{d \Delta q_i}{dt} + \left. \frac{\partial \tilde{\mathbf{C}}}{\partial q_i} \right|_0 \Delta q_i + \left. \frac{\partial \tilde{\mathbf{C}}}{\partial \dot{q}_i} \right|_0 \frac{d \Delta q_i}{dt} + \left. \frac{\partial \tilde{\mathbf{K}}}{\partial q_i} \right|_0 \frac{d \Delta q_i}{dt} \\ = \tilde{\mathbf{Q}}_0 \mathbf{F}_0^B + \tilde{\mathbf{Q}}_0 \Delta \mathbf{F}^B + \left. \frac{\partial \tilde{\mathbf{Q}}}{\partial q_i} \right|_0 \mathbf{F}_0^B \Delta q_i \end{aligned} \quad (3.71)$$

Now the steady state point or initial condition will satisfy [48],

$$\tilde{\mathbf{M}}_0 \left. \frac{d^2 \mathbf{q}}{dt^2} \right|_0 + \tilde{\mathbf{G}}_0 \left. \frac{d \mathbf{q}}{dt} \right|_0 - \tilde{\mathbf{H}}_0 + \tilde{\mathbf{C}}_0 + \tilde{\mathbf{K}}_0 = \tilde{\mathbf{Q}}_0 \mathbf{F}_0^B \quad (3.72)$$

This leaves us with the perturbation equation about the steady state point which comes out to be [48]:

$$\begin{aligned} \tilde{\mathbf{M}}_0 \frac{d^2 \Delta q_i}{dt^2} + \left(\tilde{\mathbf{G}}_0 + \left. \frac{\partial \tilde{\mathbf{G}}}{\partial \dot{q}_i} \right|_0 \frac{d\mathbf{q}}{dt} \right. & \left. - \left. \frac{\partial \tilde{\mathbf{H}}}{\partial \dot{q}_i} \right|_0 + \left. \frac{\partial \tilde{\mathbf{C}}}{\partial \dot{q}_i} \right|_0 \right) \frac{d\Delta q_i}{dt} \\ + \left(\left. \frac{\partial \tilde{\mathbf{M}}}{\partial q_i} \right|_0 \frac{d^2 \mathbf{q}}{dt^2} \right. & \left. + \left. \frac{\partial \tilde{\mathbf{G}}}{\partial q_i} \right|_0 \frac{d\mathbf{q}}{dt} - \left. \frac{\partial \tilde{\mathbf{H}}}{\partial q_i} \right|_0 + \left. \frac{\partial \tilde{\mathbf{C}}}{\partial q_i} \right|_0 + \left. \frac{\partial \tilde{\mathbf{K}}}{\partial q_i} \right|_0 - \left. \frac{\partial \tilde{\mathbf{Q}}}{\partial q_i} \right|_0 \mathbf{F}_0^B \right) \Delta q_i \\ & = \tilde{\mathbf{Q}}_0 \Delta \mathbf{F}_B \quad (3.73) \end{aligned}$$

The mass, stiffness and damping terms are respectively combined to yield the simplified unconstrained linear equation of motion as follows [48]:

$$\mathbf{M}_0 \frac{d^2 \Delta \mathbf{q}}{dt^2} + \mathbf{C}_0 \frac{d\Delta \mathbf{q}}{dt} + \mathbf{K}_0 \Delta \mathbf{q} = \mathbf{Q}_0 \Delta \mathbf{F}_B \quad (3.74)$$

The required derivatives in the linearized equation of motion are skipped for the sake of brevity. They can be found in [48].

Now, we are especially interested in finding the linearized constrained equations of motion for the wind turbine structure but instead of absorbing the constraints directly in Eqn. 3.73, which complicates the equation, we can preferably go back to the unconstrained non-linear equation of motion in Eqn. 3.55 and write it in the following form [48]:

$$\tilde{\mathbf{M}}(\mathbf{q}) \frac{d^2 \mathbf{q}}{dt^2} = \mathbf{R}(\mathbf{q}, \dot{\mathbf{q}}) + \tilde{\mathbf{Q}}(\mathbf{q}) \mathbf{F}_B \quad (3.75)$$

Note that \mathbf{R} basically absorbs the stiffness, damping, gyroscopic and centrifugal terms. Applying the constraints we get,

$$\tilde{\mathbf{M}}(\mathbf{q}) \left(\Lambda \frac{d^2 \hat{\mathbf{q}}}{dt^2} + \Gamma \frac{d\hat{\mathbf{q}}}{dt} \right) = \mathbf{R}(\mathbf{q}, \dot{\mathbf{q}}) + \tilde{\mathbf{Q}}(\mathbf{q}) \mathbf{F}_B \quad (3.76)$$

Premultiplying by Λ^T and linearizing, as shown above, we get the equation representing the perturbations. A substitution for \mathbf{q} in terms of $\hat{\mathbf{q}}$, given in Eqn. 3.65, is needed. Making this substitution, we get [48]:

$$\begin{aligned} \Lambda_0^T \tilde{\mathbf{M}}_0 \Lambda_0 \frac{d^2 \Delta \hat{\mathbf{q}}}{dt^2} &= -\Lambda_0^T \tilde{\mathbf{M}}_0 \Gamma_0 \frac{d\Delta \hat{\mathbf{q}}}{dt} + \Lambda_0^T \left(-\tilde{\mathbf{M}}_0 \left. \frac{\partial \tilde{\Gamma}}{\partial \dot{q}_k} \right|_0 \frac{d\hat{\mathbf{q}}}{dt} + \left. \frac{\partial \mathbf{R}}{\partial \dot{q}_k} \right|_0 \right) \Lambda_{kp} \frac{d\Delta \hat{q}_p}{dt} \\ + \Lambda_0^T \left[\left(-\tilde{\mathbf{M}}_0 \left. \frac{\partial \tilde{\Lambda}}{\partial q_k} \right|_0 \frac{d^2 \hat{\mathbf{q}}}{dt^2} \right. \right. & \left. \left. - \tilde{\mathbf{M}}_0 \left. \frac{\partial \tilde{\Gamma}}{\partial q_k} \right|_0 \frac{d\hat{\mathbf{q}}}{dt} - \left. \frac{\partial \tilde{\mathbf{M}}}{\partial q_k} \frac{d^2 \hat{\mathbf{q}}}{dt^2} \right. + \left. \frac{\partial \mathbf{R}}{\partial q_k} \right|_0 + \left. \frac{\partial \tilde{\mathbf{Q}}}{\partial q_k} \right|_0 \mathbf{F}_0^B \right) \Lambda_{kp} + \left(-\tilde{\mathbf{M}}_0 \left. \frac{\partial \tilde{\Gamma}}{\partial \dot{q}_k} \right|_0 \frac{d\hat{\mathbf{q}}}{dt} + \left. \frac{\partial \mathbf{R}}{\partial \dot{q}_k} \right|_0 \right) \Gamma_{kp} \right] \Delta q_k \\ &+ \Lambda_0^T \tilde{\mathbf{Q}}_0 \Delta \mathbf{F}_B \quad (3.77) \end{aligned}$$

where the first derivative of Λ with respect to q_k is obtained by some mathematical manipulation which involves pre-multiplication of Λ by a chosen matrix and then taking the derivative. It proceeds as follows [48]:

$$\begin{bmatrix} \mathbf{I} & \mathbf{0} \\ \mathbf{0} & \mathbf{L}_s \end{bmatrix} \Lambda = \begin{bmatrix} \mathbf{I} & \mathbf{0} \\ \mathbf{0} & \mathbf{L}_s \end{bmatrix} \begin{bmatrix} \mathbf{I} \\ -\mathbf{L}_s^{-1} \hat{\mathbf{L}} \end{bmatrix} \quad (3.78)$$

Taking the derivative we obtain [48]:

$$\begin{aligned} & \begin{bmatrix} 0 & 0 \\ 0 & \frac{\partial \mathbf{L}_s}{\partial q_k} \end{bmatrix} \Lambda + \begin{bmatrix} \mathbf{I} & 0 \\ 0 & \mathbf{L}_s \end{bmatrix} \frac{\partial \Lambda}{\partial q_k} = \begin{bmatrix} 0 \\ -\frac{\partial \dot{\mathbf{L}}}{\partial q_k} \end{bmatrix} \\ \Rightarrow \frac{\partial \Lambda}{\partial q_k} &= \begin{bmatrix} \mathbf{I} & 0 \\ 0 & \mathbf{L}_s \end{bmatrix}^{-1} \left(\begin{bmatrix} 0 \\ -\frac{\partial \dot{\mathbf{L}}}{\partial q_k} \end{bmatrix} - \begin{bmatrix} 0 & 0 \\ 0 & \frac{\partial \mathbf{L}_s}{\partial q_k} \end{bmatrix} \Lambda \right) \end{aligned} \quad (3.79)$$

Similarly, its possible to obtain the following derivatives [48] :

$$\begin{aligned} \frac{\partial \Gamma}{\partial q_k} &= \begin{bmatrix} \mathbf{I} & 0 \\ 0 & \mathbf{L}_s \end{bmatrix}^{-1} \left(\begin{bmatrix} 0 \\ -\frac{dq_j}{dt} \frac{\partial^2 \mathbf{L}}{\partial q_j \partial q_k} \Lambda - \frac{dq_j}{dt} \frac{\partial \mathbf{L}}{\partial q_j} \frac{\partial \Lambda}{\partial q_k} \end{bmatrix} - \begin{bmatrix} 0 & 0 \\ 0 & \frac{\partial \mathbf{L}_s}{\partial q_k} \end{bmatrix} \Gamma \right) \\ \frac{\partial \Gamma}{\partial \dot{q}_k} &= \begin{bmatrix} 0 \\ -\mathbf{L}_s^{-1} \frac{\partial \mathbf{L}}{\partial \dot{q}_k} \Gamma \end{bmatrix} \end{aligned} \quad (3.80)$$

Finally, a more concise form of the constrained linearized equations of motion can be written as follows [48]:

$$\mathbf{M}_\lambda \frac{d^2 \Delta \hat{\mathbf{q}}}{dt^2} + \mathbf{C}_\lambda \frac{d \Delta \hat{\mathbf{q}}}{dt} + \mathbf{K}_\lambda \Delta \hat{\mathbf{q}} = \mathbf{Q}_\lambda \Delta \mathbf{F}_B \quad (3.81)$$

3.4.6. Modal reduction

As already discussed, modal reduction is one way to reduce the order of large, complex systems. Here, the local modes of each body are calculated separately and used for reduction. This gives a more intuitive interpretation of the modes as compared to the global modes of the assembled system which may include strong couplings between motions of different sub-structures. The elastic degrees of freedom associated with each body are partitioned and separated out, and then composed into an undamped eigenvalue problem of the form given below, where ν represents an eigenvector.

$$(-\omega^2 \mathbf{M}_0 + \mathbf{K}_0) \nu = 0 \quad (3.82)$$

Here the subscript λ is meant to signify that constraints have been applied to the body. The eigenvectors are assembled columnwise into a matrix Φ such that,

$$\Delta \hat{\mathbf{q}} = \Phi \Delta \boldsymbol{\eta} \quad (3.83)$$

where, $\Delta \boldsymbol{\eta}$ represents the vector of modal amplitudes. The constrained equations of motion are accordingly transformed to [48]:

$$\begin{aligned} \Phi^T \mathbf{M}_\lambda \Phi \frac{d^2 \Delta \boldsymbol{\eta}}{dt^2} + \Phi^T \mathbf{C}_\lambda \Phi \frac{d \Delta \boldsymbol{\eta}}{dt} + \Phi^T \mathbf{K}_\lambda \Phi \Delta \boldsymbol{\eta} &= \Phi^T \mathbf{Q}_\lambda \Delta \mathbf{F}_B \\ \Rightarrow \mathbf{M} \frac{d^2 \Delta \boldsymbol{\eta}}{dt^2} + \mathbf{C} \frac{d \Delta \boldsymbol{\eta}}{dt} + \mathbf{K} \Delta \boldsymbol{\eta} &= \mathbf{Q} \Delta \mathbf{F}_B \end{aligned} \quad (3.84)$$

This process of modal reduction diagonalizes the mass and stiffness matrices which leads to a way of specifying the damping in terms of the modes known as Rayleigh damping. Here, the diagonal terms of \mathbf{C} can be computed in terms of the corresponding diagonal terms of \mathbf{M} and \mathbf{K} , and the damping ratio ζ_d [48].

$$C_\eta = 2\zeta_d \sqrt{M_\eta K_\eta} \quad (3.85)$$

Finally, we obtain the linear state space form given below [48] :

$$\begin{bmatrix} \mathbf{I} & \mathbf{0} \\ \mathbf{0} & \mathbf{M} \end{bmatrix} \frac{d}{dt} \begin{bmatrix} \Delta \boldsymbol{\eta} \\ \Delta \dot{\boldsymbol{\eta}} \end{bmatrix} = \begin{bmatrix} \mathbf{0} & \mathbf{I} \\ -\mathbf{K} & -\mathbf{C} \end{bmatrix} \begin{bmatrix} \Delta \boldsymbol{\eta} \\ \Delta \dot{\boldsymbol{\eta}} \end{bmatrix} + \begin{bmatrix} \mathbf{0} \\ \mathbf{Q} \Delta \mathbf{F}_B \end{bmatrix} \quad (3.86)$$

In shorthand notation, used later for coupling with the aerodynamic state space, we can now write :

$$\begin{aligned} \mathbf{N}_s \frac{d\mathbf{x}_s}{dt} &= \mathbf{A}_s \mathbf{x}_s + \mathbf{B}_{u,s} \mathbf{u} \\ \mathbf{y}_s &= \mathbf{C}_s \mathbf{x}_s \end{aligned} \quad (3.87)$$

The symbols have their usual meanings in context of state space modelling. Subscripts s and a denote variables and matrices belonging to the structural and aerodynamic state spaces respectively. \mathbf{u} is the input matrix containing both the global as well as aerodynamic inputs.

3.5. Aerodynamics

The aerodynamics model in STAS WPP is based on the Blade Element Momentum (BEM) method for steady state, but empirical models have been added to incorporate unsteady effects similar to the approach in Section 2.3.4. The included unsteady effects are dynamic inflow, circulation lag and dynamic stall. A correction to the quasi-steady induced velocity for yawed flow is also applied. As for the structural part, the aerodynamic model is also linearized about a steady state point or initial point.

3.5.1. Coordinate system

The aerodynamic analysis employs certain coordinate systems which must be defined at this point. The rotorplane coordinate system, as defined for the structure, is a reference frame common to all blade elements (Section 3.4.1). There are other coordinate systems which are associated with each element. The section coordinate system, situated at the midpoint of each blade element, is basically the blade pitch coordinate system rotated about $X^s = X^p$ by the element aerodynamic twist angle. Then there is the airfoil coordinate system, used to represent the thrust and tangential forces, which originates at the quarter-chord point aft of the leading edge of the blade element. The X^a axis lies along the chord pointing towards the trailing edge, while axis Y^a is oriented along Z^s axis (Fig. 2.5).

Now, the airfoil and section coordinate system will follow the deformation of the blades but not the pitch coordinate system. So the transform from the blade pitch to section coordinate system can be defined in the following way [48] :

$$\mathbf{T}_p^s = \begin{bmatrix} 1 & 0 & 0 \\ 0 & \cos \theta_1 & \sin \theta_1 \\ 0 & -\sin \theta_1 & \cos \theta_1 \end{bmatrix} \begin{bmatrix} \cos \theta_2 & 0 & -\sin \theta_2 \\ 0 & 1 & 0 \\ \sin \theta_2 & 0 & \cos \theta_2 \end{bmatrix} \begin{bmatrix} \cos \theta_3 & \sin \theta_3 & 0 \\ -\sin \theta_3 & \cos \theta_3 & 0 \\ 0 & 0 & 1 \end{bmatrix} \quad (3.88)$$

Here, θ_1 is the combined effect of the twist angle and blade torsion, θ_2 combines a possible prebend angle and elastic rotation about Y^p , and θ_3 is the sum of a possible sweep angle and elastic rotation about Z^p . Alternatively, the transform from the airfoil to the section coordinate system is only dependent on the structural twist angle since deformations are common for both [48].

Now, the momentum equations are expressed in the rotorplane coordinates whereas the forces based on blade element theory are in airfoil coordinates. A transformation between rotorplane and the airfoil coordinates in the key link in BEM. It is expressed as a series of sequential transformations [48].

$$\mathbf{T}_a^r = \mathbf{T}_y^r \mathbf{T}_{y0}^y (\Phi_{y0}^y) \mathbf{T}_g^{y0} \mathbf{T}_{p0}^g \mathbf{T}_p^{p0} (\Phi_p^{p0}) \mathbf{T}_{s0}^p \mathbf{T}_s^{s0} (\theta_s^{s0}) \mathbf{T}_a^s \quad (3.89)$$

The transform \mathbf{T}_a^s is determined by the structural twist, \mathbf{T}_p^s is given in Eqn. 3.88, \mathbf{T}_{p0}^p is primarily dependent on the change in blade pitch angle and \mathbf{T}_{y0}^{y0} on the yaw angle. The rest of the transforms are based on the undeformed wind turbine geometry.

For the purpose of describing the aerodynamic model in STAS WPP, the notation convention used for the structural dynamics is adopted in totality. Please note that unlike the description of aerodynamics in Chapter 2, a formal convention is now necessary to enable the constant switching from one reference frame to another.

3.5.2. Non-linear aerodynamics

The local flow velocity vector in airfoil coordinates, measured with respect to the global coordinates, is given as [48]:

$$\mathbf{U}_{/g}^a = \mathbf{V}_\infty^a + \mathbf{V}_i^a - \mathbf{w}_{/g}^a \quad (3.90)$$

where \mathbf{V}_∞^a is the freestream incoming wind velocity vector including turbulence, \mathbf{V}_i^a is the induced velocity vector and $\mathbf{w}_{/g}^a$ is the structural velocity including blade rotation (see Eqn. 3.43), all expressed in the airfoil coordinate system. The structural velocity of a blade element is taken as average of the nodal structural velocities.

The quasi-steady angle of attack can be computed using Eqn.2.25 to be [48]:

$$\alpha_q = \tan^{-1} \frac{(\mathbf{U}^a)_y}{(\mathbf{U}^a)_x} \quad (3.91)$$

A dynamic angle of attack, α which is used to calculate the aerodynamic forces is obtained using the empirical models of Eqn. 2.26 and Eqn. 2.28. The circulation lag and dynamic stall models are combined and written in state space as follows [48]:

$$\frac{d}{dt} \begin{bmatrix} \alpha \\ a_1 \\ a_2 \end{bmatrix} = \begin{bmatrix} -\tau^{-1} & \tau^{-1}K_1 & \tau^{-1}K_2 \\ 0 & 0 & 1 \\ 0 & A_{32} & A_{33} \end{bmatrix} \begin{bmatrix} \alpha \\ a_1 \\ a_2 \end{bmatrix} + \begin{bmatrix} \tau^{-1}K_3 \\ 0 \\ 1 \end{bmatrix} \alpha_q \quad (3.92)$$

Refer to Eqn. 2.27 and Eqn. 2.29 for definition of parameters. Note that A_{21} and A_{22} from 2.27 are now renamed A_{32} and A_{33} . The resultant velocity used in the calculation of the circulation lag parameters and the dynamic stall time constant is now given as U , such that [48]:

$$U = \sqrt{(\mathbf{U}_{/g}^a)_x^2 + (\mathbf{U}_{/g}^a)_y^2} \quad (3.93)$$

Once the local flow velocity vector and dynamic angle of attack are known, we can proceed to find out the aerodynamic forces [48].

$$\begin{aligned} F_l &= C_l(\alpha, \alpha_q) \frac{1}{2} \rho c L U^2 \\ F_d &= C_d(\alpha_q) \frac{1}{2} \rho c L U^2 \end{aligned} \quad (3.94)$$

where, C_l and C_d are determined using Eqn. 2.30.

Expressing the lift and drag forces in the airfoil coordinates we get [48],

$$\mathbf{F}^a = \frac{1}{2}\rho cLU^2 \begin{bmatrix} -\sin\alpha_q & \cos\alpha_q & 0 \\ \cos\alpha_q & \sin\alpha_q & 0 \\ 0 & 0 & 0 \\ 0 & 0 & 0 \\ 0 & 0 & 0 \\ -\cos\alpha_q x - \sin\alpha_q y & -\sin\alpha_q x + \cos\alpha_q y & -c \end{bmatrix} \begin{bmatrix} C_l \\ C_d \\ C_m \end{bmatrix} \Rightarrow \mathbf{F}^a = \frac{1}{2}\rho cLU^2 \mathbf{TC} \quad (3.95)$$

Note that the coordinates x and y refer to the in-plane coordinates of the section coordinate system origin relative to the aerodynamic center, normally taken to be the quarter-chord point. Here, \mathbf{T} and \mathbf{C} are the transform from the coordinates in which lift and drag forces are conventionally defined (related to direction of relative velocity) to the airfoil coordinates and the airfoil coefficient matrices respectively [48].

For writing the momentum balance equations we shift back to the rotor plane coordinate system. The general form of the momentum balance for a rotor annulus of area A located at a given radius r is [48]:

$$\begin{aligned} (F^r)_z &= -2\rho AfW(V_{i,q}^r)_a \\ (F^r)_t &= -2\rho AfW(V_{i,q}^r)_t \end{aligned} \quad (3.96)$$

where f is the Prandtl root-tip loss factor defined in Eqn. 2.22, $\mathbf{V}_{i,q}^r$ is the quasi-steady induced velocity in rotor plane coordinates, and W is the resultant incoming wind velocity given as:

$$W = \sqrt{[(\mathbf{V}_{i,q}^r)_z + f(\mathbf{V}_{i,q}^r)_z]^2 + (\mathbf{V}_{i,q}^r)_t^2 + (\mathbf{V}_{i,q}^r)_s^2} \quad (3.97)$$

where the spanwise component is neglected in calculations, and

$$\mathbf{V}_{i,q}^r = \mathbf{V}_{\infty/g}^r - \mathbf{w}_{r/g}^r \quad (3.98)$$

The relation between induced velocity and the thrust force is corrected for heavily loaded rotors using the Glauert correction (Eqn. 2.8). So if [48],

$$(V_{i,q}^r)_z < -\frac{(V_{i,q}^r)_a}{f} a_1 \quad (3.99)$$

Then the axial component of induced velocity is given by [48] :

$$(V_{i,q}^r)_z = -\frac{(V_{i,q}^r)_z}{f} \left[\left(\frac{(F^r)_a}{0.5(C_{T2} - C_{T1})\rho A |\mathbf{V}_{i,q}^r|^2} - \frac{C_{T1}}{C_{T2} - C_{T1}} \right) (1 - a_1) + a_1 \right] \quad (3.100)$$

where the parameters C_{T1} , C_{T2} and a_1 assume the usual values given in Eqn. 2.8.

The dynamic inflow filter, given in Eqn. 2.23, is next applied to the quasi-steady induced velocity, $\mathbf{V}_{i,q}$ to yield the dynamic induced velocity, \mathbf{V}_i . For that, we must first determine $\mathbf{V}_{i,q}$ using Eqn. 3.96. It is important to note that W itself is dependent on $\mathbf{V}_{i,q}$. To overcome this problem, an approximation is used such that W is replaced by \tilde{W} in Eqn. 3.96, where [48]:

$$\tilde{W} = \sqrt{[(\mathbf{V}_{/r}^r)_z + f(\mathbf{V}_i^r)_z]^2 + (\mathbf{V}_{/r}^r)_t^2 + (\mathbf{V}_{/r}^r)_s^2} \quad (3.101)$$

Now, \tilde{W} is dependent on the known value of \mathbf{V}_i^r from the previous time step.

For yawed conditions, $\mathbf{V}_{i,q}$ is modified to $\tilde{\mathbf{V}}_{i,q}$, before applying the dynamic inflow filter, using the following relation [48]:

$$\tilde{\mathbf{V}}_{i,q}^r = \left[1 + \frac{r}{R} \tan \left(0.5 \cos^{-1} \left(\frac{\mathbf{V}_{/r}^r + f(\mathbf{V}_i^r)_a}{\tilde{W}} \right) \right) \cos(\Psi_b - \Psi_0) \right] \mathbf{V}_i^r \quad (3.102)$$

where Ψ_b is the blade azimuth angle and Ψ_0 is the blade azimuth angle when the blade is deepest into the wake [48].

3.5.3. Linearized aerodynamic model

The linearized aerodynamic model is developed as a series of linked sub-modules which are individually represented as follows:

$$\begin{aligned} \frac{d\mathbf{x}_a}{dt} &= \mathbf{A}_a \mathbf{x}_a + \mathbf{B}_{u,a} \mathbf{u} + \mathbf{B}_{y,a} \mathbf{y}_a \\ \mathbf{y}_a &= \mathbf{C}_a \mathbf{x}_a + \mathbf{D}_{u,a} \mathbf{u} + \mathbf{D}_{y,a} \mathbf{y}_a \end{aligned} \quad (3.103)$$

Here \mathbf{u} represents the global inputs as well as the structural inputs. It is important to note that \mathbf{y}_a in the LHS of the output equation represents the local outputs. The \mathbf{y}_a in the RHS of both equations depicts the local inputs. The basic essence of the above equations is that if we were to look at the aerodynamic module in terms of a set of sub-modules then the local outputs of one sub-module are the local inputs of the next sub-module. Note that the diagonals of \mathbf{D}_y are zero [46].

Structural velocity The structural velocity of a node in global coordinates is obtained using Eqn. 3.43. This can be transformed to airfoil coordinates as follows [48]:

$$\mathbf{w}_{n/g}^a = \mathbf{T}_s^a \mathbf{T}_B^s \mathbf{T}_{B0}^B \mathbf{T}_g^{B0} \mathbf{w}_{n/g}^g \quad (3.104)$$

Linearizing the above equation using a first order Taylor series expansion, where \mathbf{Q}_w is the part of \mathbf{Q}_v Eqn. 3.43 which gives linear structural velocities of a node, we get [48]:

$$\begin{aligned} \Delta \mathbf{w}_{n/g}^a &= \left[\mathbf{T}_s^a \mathbf{T}_B^s \mathbf{T}_{B0}^B \frac{\partial \mathbf{Q}_w}{\partial q_i} \bigg|_0 \frac{dq}{dt} \bigg|_0 + \left(\mathbf{T}_s^a \frac{\partial \mathbf{T}_B^s}{\partial q_i} \mathbf{T}_{B0}^B \mathbf{T}_g^{B0} + \mathbf{T}_s^a \mathbf{T}_B^s \frac{\partial \mathbf{T}_{B0}^B}{\partial q_i} \mathbf{T}_g^{B0} \right) \mathbf{w}_{n/g}^g \bigg|_0 \right] \Delta q_i + \\ &\quad \mathbf{T}_s^a \mathbf{T}_B^s \mathbf{T}_{B0}^B \mathbf{Q}_w^g \frac{d\Delta \mathbf{q}}{dt} \end{aligned} \quad (3.105)$$

Local flow velocity Referring to the local flow velocity given in Eqn. 3.90 and linearizing [48],

$$\Delta \mathbf{U}_{/g}^a = \mathbf{T}_g^a \Delta \mathbf{V}_\infty^g + \mathbf{T}_r^a \Delta \mathbf{V}_i^r + \left(\frac{\partial \mathbf{T}_g^a}{\partial q_i} \mathbf{V}_\infty^g + \frac{\partial \mathbf{T}_r^a}{\partial q_i} \mathbf{V}_i^r \right) \Delta q_i - \Delta \mathbf{w}_{n/g}^a \quad (3.106)$$

The magnitude of the local flow velocity is linearized as follows [48]:

$$\Delta U = \frac{(U^a)_x}{\sqrt{(U^a)_x^2 + (U^a)_y^2}} \Delta(U^a)_x + \frac{(U^a)_y}{\sqrt{(U^a)_x^2 + (U^a)_y^2}} \Delta(U^a)_y \quad (3.107)$$

The local flow velocity can also be expressed in rotorplane coordinates [48]. This may be used later in calculating the inflow angle to determine the Prandtl factor.

$$\mathbf{U}_{/r}^r = \mathbf{T}_a^r \mathbf{U}_{/g}^a \quad (3.108)$$

On linearizing we get [48],

$$\Delta \mathbf{U}_{/r}^r = \frac{\partial \mathbf{T}_a^r}{\partial q_i} \mathbf{U}_{/g}^a \Delta q_i + \mathbf{T}_a^r \Delta \mathbf{U}_{/g} \quad (3.109)$$

Quasi-steady angle of attack Linearizing α_q in terms of the local flow velocity vector components we get [48],

$$\Delta \alpha_q = -\frac{(U^a)_y}{\sqrt{(U^a)_x^2 + (U^a)_y^2}} \Delta(U^a)_x + \frac{(U^a)_x}{\sqrt{(U^a)_x^2 + (U^a)_y^2}} \Delta(U^a)_y \quad (3.110)$$

Dynamic angle of attack Referring to Eqn. 3.92 which is of the form,

$$\frac{d\mathbf{x}}{dt} = \mathbf{A}\mathbf{x} + \mathbf{B}\mathbf{u} \quad (3.111)$$

And linearizing, we get [48]:

$$\frac{d\Delta\mathbf{x}}{dt} = \mathbf{A}\Delta\mathbf{x} + \mathbf{B}\Delta\mathbf{u} + \left(\frac{\partial \mathbf{A}}{\partial U} \mathbf{x} + \frac{\partial \mathbf{B}}{\partial U} \mathbf{u} \right) \Delta U \quad (3.112)$$

Here $\Delta\alpha_q$ is the local input. Note that the parameters for circulation lag and dynamic stall models are dependent on the resultant velocity, U and hence the derivative with respect to U in the linearization. The linearized equation can be rewritten by substituting for the derivatives [48].

$$\begin{aligned} \frac{d}{dt} \begin{bmatrix} \Delta\alpha \\ \Delta a_1 \\ \Delta a_2 \end{bmatrix} &= \begin{bmatrix} -\tau^{-1} & \tau^{-1}K_1 & \tau^{-1}K_2 \\ 0 & 0 & 1 \\ 0 & A_{32} & A_{33} \end{bmatrix} \begin{bmatrix} \Delta\alpha \\ \Delta a_1 \\ \Delta a_2 \end{bmatrix} + \begin{bmatrix} \tau^{-1}K_3 \\ 0 \\ 1 \end{bmatrix} \Delta\alpha_q + \\ &\left(\begin{bmatrix} -\frac{1}{4.3c} & \frac{K_1}{4.3c} + 8(A_1 + A_2)b_1b_2\frac{U}{\tau c^2} & \frac{K_2}{4.3c} + \frac{2(A_1b_1 + A_2b_2)}{\tau c} \\ 0 & 0 & 0 \\ 0 & -\frac{8b_1b_2U}{c^2} & -2\frac{b_1b_2U}{c^2} \end{bmatrix} \begin{bmatrix} \alpha \\ a_1 \\ a_2 \end{bmatrix} + \begin{bmatrix} \frac{K_3}{4.3c} \\ 0 \\ 0 \end{bmatrix} \alpha_q \right) \Delta U \end{aligned} \quad (3.113)$$

The parameters can again be found to be defined in Eqn. 2.27 & Eqn. 2.29.

Aerodynamic forces The dynamic lift coefficient is dependent on both α and α_q . Hence the linearization is [48],

$$\Delta C_l = \left[\frac{\partial C_l}{\partial \alpha} \left(1 + \frac{\alpha_q - \alpha}{\alpha - \alpha_z} \right) - \frac{C_l}{\alpha - \alpha_z} - C_l \frac{\alpha_q - \alpha}{(\alpha - \alpha_z)^2} \right] \Delta \alpha + \frac{C_l}{\alpha - \alpha_z} \Delta \alpha_q \quad (3.114)$$

The dynamic drag and moment coefficients are only dependent on α_q so the linearization is [48],

$$\Delta C_d = \frac{\partial C_d}{\partial \alpha} \Delta \alpha_q, \quad \Delta C_m = \frac{\partial C_m}{\partial \alpha} \Delta \alpha_q \quad (3.115)$$

Referring to the aerodynamic forces in airfoil coordinates in Eqn. 3.95 and linearizing gives [48],

$$\Delta \mathbf{F}_a = \frac{1}{2} \rho c L \left(2U \mathbf{T} \mathbf{C} \Delta U + U^2 \frac{\partial \mathbf{T}}{\partial \alpha} \mathbf{C} \Delta \alpha_q + U^2 \mathbf{T} \Delta \mathbf{C} \right) \quad (3.116)$$

For input to the structural model, aerodynamic forces must be in the pitch coordinate system so transforming from airfoil to pitch coordinates we get [48],

$$\mathbf{F}^p = \mathbf{T}_s^p \mathbf{T}_a^s \mathbf{F}^a \quad (3.117)$$

Linearizing above relation gives us [48],

$$\Delta \mathbf{F}^p = \mathbf{T}_s^p \mathbf{T}_a^s \Delta \mathbf{F}^a + \frac{\partial \mathbf{T}_s^p}{\partial q_i} \mathbf{T}_a^s \mathbf{F}^a \Delta q_i \quad (3.118)$$

Projection of blade element on rotor plane Now the global position of a node has been defined in the structural model in Eqn. 3.37 and is denoted as $\mathbf{r}_{n/g}^g$. Since the structural and aerodynamic elements are assumed to be the same, we can define a blade element's global position as [48]:

$$\mathbf{r}_{e/g}^g = \frac{1}{2} (\mathbf{r}_{n1/g}^g + \mathbf{r}_{n2/g}^g) \quad (3.119)$$

Defining the position of the hub center node as $\mathbf{r}_{h/g}^g$, we get the vector from the hub center to a blade node as [48]:

$$\mathbf{r}_{n1/r}^r = \mathbf{T}_g^r (\mathbf{r}_{n1/g}^g - \mathbf{r}_{h/g}^g) \quad (3.120)$$

Projecting this onto the rotor plane and defining the projected vector as $\tilde{\mathbf{r}}_{n1/r}^r$ the spanwise element length is found to be [48]:

$$\tilde{L} = |\tilde{\mathbf{r}}_{n2/r}^r - \tilde{\mathbf{r}}_{n1/r}^r| \quad (3.121)$$

$\tilde{\mathbf{r}}_{e/r}^r$ can be defined similarly. Linearizing the equations we get [48],

$$\begin{aligned}
\Delta \mathbf{r}_{n/g}^g &= \mathbf{A}_n \tilde{\mathbf{T}}_B^g \Delta \mathbf{q} + \mathbf{A}_n \frac{\partial \tilde{\mathbf{T}}_B^g}{\partial q_i} (\mathbf{q} + \mathbf{P}) \Delta q_i \\
\Delta \mathbf{r}_{n/g}^g &= \mathbf{T}_g^r (\Delta \mathbf{r}_{e/g}^g - \Delta \mathbf{r}_{h/g}^g) + \frac{\partial \mathbf{T}_g^r}{\partial q_i} (\mathbf{r}_{e/g}^g - \mathbf{r}_{h/g}^g) \Delta q_i \\
\Delta \tilde{L} &= \frac{1}{|\tilde{\mathbf{r}}_{n2/r}^r - \tilde{\mathbf{r}}_{n1/r}^r|} (\tilde{\mathbf{r}}_{n2/r}^r \Delta \tilde{\mathbf{r}}_{n2/r}^r - \tilde{\mathbf{r}}_{n1/r}^r \Delta \tilde{\mathbf{r}}_{n2/r}^r)
\end{aligned} \tag{3.122}$$

Prandtl factor The Prandtl tip loss factor given in Eqn. 2.20 is subsequently linearized but first it makes sense to write it in a simplified form [48].

$$f_{tip} = \frac{2}{\pi} \cos^{-1}(\exp(\alpha)) \tag{3.123}$$

Note that [48],

$$\begin{aligned}
\alpha &= \frac{k}{\sin \phi}, \quad k = \frac{B(r-R)}{2r} \\
\phi &= \tan^{-1} \frac{(U_{/r}^r)_z}{(U_{/r}^r)_t}
\end{aligned} \tag{3.124}$$

The linearization is given as follows [48]:

$$\begin{aligned}
\Delta f_{tip} &= -\left(\frac{2}{\pi}\right) \frac{\exp(\alpha)}{\sqrt{1-\exp(2\alpha)}} \Delta z \\
\Delta \kappa &= -\frac{k}{\sin \phi \tan \phi} \left(\frac{\partial \phi}{\partial (U_{/r}^r)_z} \Delta (U_{/r}^r)_z + \frac{\partial \phi}{\partial (U_{/r}^r)_t} \Delta (U_{/r}^r)_t \right)
\end{aligned} \tag{3.125}$$

where [48],

$$\frac{\partial \phi}{\partial (U_{/r}^r)_z} = \frac{(U_{/r}^r)_t}{(U_{/r}^r)_z^2 + (U_{/r}^r)_t^2}, \quad -\frac{\partial \phi}{\partial (U_{/r}^r)_t} = \frac{(U_{/r}^r)_z}{(U_{/r}^r)_z^2 + (U_{/r}^r)_t^2} \tag{3.126}$$

Flow velocity at the rotor plane Denoted as $\mathbf{V}_{/r}^r$, the flow velocity at the rotorplane is needed to calculate the resultant inflow velocity at the rotor plane, W . W in turn determines the air mass inflow at the rotor plane required to calculate the change in momentum of air at the rotor plane. It is assumed that the rotor plane is a flat circular disk which follows the translational motion of the nacelle and support structure. Then $\mathbf{V}_{/r}^r$ can be obtained by removing the rotational speed and induced velocity from $\mathbf{U}_{/r}^r$, leading to [48]:

$$\mathbf{V}_{/r}^r = \mathbf{U}_{/r}^r - \mathbf{V}_i^r + \begin{bmatrix} 0 \\ |\tilde{\mathbf{r}}_{e/r}^r| \Omega \\ 0 \end{bmatrix} \tag{3.127}$$

Linearizing component wise we end up with [48]:

$$\begin{aligned}
\Delta (V_{/r}^r)_z &= \Delta (U_{/r}^r)_z - \Delta (V_i^r)_z \\
\Delta (V_{/r}^r)_t &= \Delta (U_{/r}^r)_t - \Delta (V_i^r)_t + \frac{(\tilde{\mathbf{r}}_{e/r}^r)_x \Omega}{\sqrt{(\tilde{\mathbf{r}}_{e/r}^r)_x^2 + (\tilde{\mathbf{r}}_{e/r}^r)_y^2}} \Delta (\tilde{\mathbf{r}}_{e/r}^r)_x + \frac{(\tilde{\mathbf{r}}_{e/r}^r)_y \Omega}{\sqrt{(\tilde{\mathbf{r}}_{e/r}^r)_x^2 + (\tilde{\mathbf{r}}_{e/r}^r)_y^2}} \Delta (\tilde{\mathbf{r}}_{e/r}^r)_y + |\tilde{\mathbf{r}}_{e/r}^r| \Delta \Omega \\
\Delta (V_{/r}^r)_s &= \Delta (U_{/r}^r)_s
\end{aligned} \tag{3.128}$$

Aerodynamic forces in rotor plane coordinates The momentum equations require the aerodynamic forces to be expressed in the rotor plane coordinates. This can be simply done by the following transformation [48]:

$$\mathbf{F}^r = \mathbf{T}_a^r \mathbf{F}^a \quad (3.129)$$

Linearization yields [48],

$$\Delta \mathbf{F}^r = \mathbf{T}_a^r \Delta \mathbf{F}^a + \frac{\partial \mathbf{T}_a^r}{\partial q_i} \mathbf{F}^a \Delta q_i \quad (3.130)$$

Quasi-steady induced velocity $\mathbf{V}_{i,q}$ as obtained from Eqn. 3.96 is linearized as follows [48],

$$\Delta V_{i,q} = -\frac{1}{2\rho A f \tilde{W}} \Delta \mathbf{F}^r + \frac{4\pi\rho\mathbf{F}^r}{B(2\rho A f \tilde{W})^2} (\tilde{L} f_{tip} \tilde{W} \Delta \tilde{\mathbf{r}}_{elr}^r + \tilde{\mathbf{r}}_{elr}^r f_{tip} \tilde{W} \Delta \tilde{L} + \tilde{\mathbf{r}}_{elr}^r \tilde{L} \tilde{W} \Delta f_{tip} + \tilde{\mathbf{r}}_{elr}^r \tilde{L} f_{tip} \Delta \tilde{W}) \quad (3.131)$$

The first three linearization terms in the parentheses have been derived in already in this section. Coming to $\Delta \tilde{W}$, it is obtained simply as [48]:

$$\Delta \tilde{W} = \frac{[(V_{lr}^r)_z + f_{tip}(V_i^r)_z] [(\Delta V_{lr}^r)_z + (V_i^r)_z \Delta f_{tip} + f_{tip}(\Delta V_i^r)_z] + (V_{lr}^r)_t (\Delta V_{lr}^r)_t + (V_{lr}^r)_s (\Delta V_{lr}^r)_s}{\sqrt{[(V_{lr}^r)_z + f_{tip}(V_i^r)_z]^2 + (V_{lr}^r)_t^2 + (V_{lr}^r)_s^2}} \quad (3.132)$$

For heavily loaded rotors satisfying Eqn. 3.99 an alternative expression is specified for $(V_{i,q}^r)_z$ in Eqn. 3.100. It is first written down in a simplified form [48]:

$$(\mathbf{V}_{i,q}^r)_z = -\frac{(\mathbf{V}_{lr}^r)_z}{f} C \quad (3.133)$$

Linearizing the main equation [48],

$$(\Delta V_{i,q}^r)_z = -\frac{C}{f_{tip}} (\Delta V_{lr}^r)_z + \frac{C(V_{lr}^r)_z}{f_{tip}^2} \Delta f_{tip} - \frac{(V_{lr}^r)_z}{f_{tip}} \Delta C \quad (3.134)$$

The first two terms in this linearization have been derived already and for the third we proceed with the Taylor series expansion to yield [48]:

$$\Delta C = \left[\frac{1 - a_1}{0.5(C_{T1} - C_{T2})\rho A |\mathbf{V}_{lr}^r|^2} \right] (\Delta F^r)_z - \left[\frac{(1 - a_1)(F^r)_z}{[0.5(C_{T1} - C_{T2})\rho A |\mathbf{V}_{lr}^r|^2]^2} \right] (C_{T1} - C_{T2})\rho \frac{\pi}{B} \\ \times [\tilde{L} |\mathbf{V}_{lr}^r|^2 \Delta \tilde{\mathbf{r}}_{elr}^r + \tilde{\mathbf{r}}_{elr}^r |\mathbf{V}_{lr}^r|^2 \tilde{L} + 2\tilde{\mathbf{r}}_{elr}^r \tilde{L} ((V_{lr}^r)_z (\Delta V_{lr}^r)_z + (V_{lr}^r)_t (\Delta V_{lr}^r)_t + (V_{lr}^r)_s (\Delta V_{lr}^r)_s)] \quad (3.135)$$

$\mathbf{V}_{i,q}^r$ is further corrected for yaw in Eqn. 3.102. Writing Eqn. 3.102 in shorthand form as [48]:

$$\Delta \tilde{\mathbf{V}}_{i,q}^r = \kappa \mathbf{V}_{i,q}^r \quad (3.136)$$

Linearizing we get [48],

$$\Delta \tilde{\mathbf{V}}_{i,q}^r = \kappa \Delta \mathbf{V}_{i,q}^r + \mathbf{V}_{i,q}^r \left(\frac{\partial \kappa}{\partial (V_{i,r}^r)_z} (\Delta V_{i,r}^r)_z + \frac{\partial \kappa}{\partial (V_{i,r}^r)_t} (\Delta V_{i,r}^r)_t + \frac{\partial \kappa}{\partial (V_{i,r}^r)_s} (\Delta V_{i,r}^r)_s + \right. \\ \left. \frac{\partial \kappa}{\partial (V_i^r)_z} (\Delta V_i^r)_z + \frac{\partial \kappa}{\partial \tilde{W}} \Delta \tilde{W} + \frac{\partial \kappa}{\partial \tilde{\mathbf{r}}_{elr}^r} \Delta \tilde{\mathbf{r}}_{elr}^r + \frac{\partial \kappa}{\partial R} \Delta R \right) \quad (3.137)$$

The terms in the linearization are given below [48]:

$$\begin{aligned} \frac{\partial \kappa}{\partial (V_{i,r}^r)_z} &= -\frac{r}{R} \left(\frac{(V_{i,r}^r)_s}{\sqrt{(V_{i,r}^r)_t^2 + (V_{i,r}^r)_s^2}} \right) \frac{1}{\tilde{W}(z_i+1)\sqrt{1-z_i^2}} \\ \frac{\partial \kappa}{\partial (V_{i,r}^r)_t} &= -\frac{r}{R} \tan\left(\frac{1}{2} \cos^{-1} z_i\right) \frac{(V_{i,r}^r)_s (V_{i,r}^r)_t}{[(V_{i,r}^r)_t^2 + (V_{i,r}^r)_s^2]^{\frac{3}{2}}} \\ \frac{\partial \kappa}{\partial (V_{i,r}^r)_s} &= \frac{r}{R} \tan\left(\frac{1}{2} \cos^{-1} z_i\right) \frac{(V_{i,r}^r)_t^2}{[(V_{i,r}^r)_t^2 + (V_{i,r}^r)_s^2]^{\frac{3}{2}}} \\ \frac{\partial \kappa}{\partial (V_i^r)_z} &= f_{tip} \frac{\partial \kappa}{\partial (V_{i,r}^r)_z} \\ \frac{\partial \kappa}{\partial f_{tip}} &= (V_i^r)_z \frac{\partial \kappa}{\partial (V_i^r)_z} \\ \frac{\partial \kappa}{\partial \tilde{W}} &= \frac{r}{R} \left(\frac{(V_{i,r}^r)_s}{\sqrt{(V_{i,r}^r)_t^2 + (V_{i,r}^r)_s^2}} \right) \frac{z_i}{\tilde{W}(z_i+1)\sqrt{1-z_i^2}} \\ \frac{\partial \kappa}{\partial r} &= \frac{1}{R} \tan\left(\frac{1}{2} \cos^{-1} z_i\right) \left(\frac{(V_{i,r}^r)_s}{\sqrt{(V_{i,r}^r)_t^2 + (V_{i,r}^r)_s^2}} \right) \\ \frac{\partial \kappa}{\partial R} &= -\frac{r}{R^2} \tan\left(\frac{1}{2} \cos^{-1} z_i\right) \left(\frac{(V_{i,r}^r)_s}{\sqrt{(V_{i,r}^r)_t^2 + (V_{i,r}^r)_s^2}} \right) \end{aligned} \quad (3.138)$$

where z_i is taken to be [48],

$$z_i = \frac{(V_{i,r}^r)_z + f_{tip} (V_i^r)_z}{\tilde{W}} \quad (3.139)$$

Dynamic induced velocity Referring back to the dynamic inflow filter applied to the quasi-steady velocity induced by a blade \mathbf{V}_i^r in Eqn. 2.23, it is possible to write the relation in simplified form as follows [48]:

$$\frac{d}{dt} \begin{bmatrix} \hat{\mathbf{V}}_i \\ \mathbf{V}_i \end{bmatrix} = \mathbf{A}_\tau \begin{bmatrix} \hat{\mathbf{V}}_i \\ \mathbf{V}_i \end{bmatrix} + \mathbf{B}_\tau \mathbf{V}_{i,q} \quad (3.140)$$

Linearizing the above equation, we get [48]:

$$\frac{d}{dt} \begin{bmatrix} \Delta \hat{\mathbf{V}}_i \\ \Delta \mathbf{V}_i \end{bmatrix} = \mathbf{A}_\tau \begin{bmatrix} \Delta \hat{\mathbf{V}}_i \\ \Delta \mathbf{V}_i \end{bmatrix} + \mathbf{B}_\tau \Delta \mathbf{V}_{i,q} + \left(\frac{\partial \mathbf{A}_\tau}{\partial \tau_1} \Delta \tau_1 + \frac{\partial \mathbf{A}_\tau}{\partial \tau_2} \Delta \tau_2 \right) \begin{bmatrix} \hat{\mathbf{V}}_i \\ \mathbf{V}_i \end{bmatrix} + \left(\frac{\partial \mathbf{B}_\tau}{\partial \tau_1} \Delta \tau_1 + \frac{\partial \mathbf{B}_\tau}{\partial \tau_2} \Delta \tau_2 \right) \mathbf{V}_{i,q} \quad (3.141)$$

The time constants in turn are linearized as follows [48]:

$$\begin{aligned}\Delta\tau_1 &= \left(\frac{\partial\tau_1}{\partial|\mathbf{V}'_{/r}|} \Delta|\mathbf{V}'_{/r}| + \frac{\partial\tau_1}{\partial(V'_{/r})_z} (\Delta V'_{/r})_z + \frac{\partial\tau_1}{\partial(V'_i)_z} (\Delta V'_i)_z + \frac{\partial\tau_1}{\partial R} \Delta R \right) \\ \Delta\tau_2 &= \left[0.39 - 0.26 \left(\frac{r}{R} \right)^2 \right] \Delta\tau_1 - 0.26 \frac{2r}{R^2} \tau_1 \Delta \tilde{\mathbf{r}}_{e/r} + 0.26 \frac{r}{R^3} \tau_1 \Delta R\end{aligned}\quad (3.142)$$

where the partial derivatives of τ_1 are as follows [48]:

$$\begin{aligned}\frac{\partial\tau_1}{\partial|\mathbf{V}'_{/r}|} &= -\frac{1.1}{1-0.3a} \frac{R}{|\mathbf{V}'_{/r}|^2} \\ \frac{\partial\tau_1}{\partial(V'_{/r})_z} &= \frac{0.33}{(1-0.3a)^2} \frac{R}{|\mathbf{V}'_{/r}|} \frac{(V'_i)_z}{(V'_{/r})_z^2} \\ \frac{\partial\tau_1}{\partial(V'_i)_z} &= \frac{0.33}{(1-0.3a)^2} \frac{R}{|\mathbf{V}'_{/r}|} \frac{1}{(V'_{/r})_z} \\ \frac{\partial\tau_1}{\partial R} &= \frac{1.1}{1-0.3a} \frac{1}{V_\infty}\end{aligned}\quad (3.143)$$

$\Delta|\mathbf{V}'_{/r}|$ has not been derived yet. This linearization can be simply stated as:

$$\Delta|\mathbf{V}'_{/r}| = \frac{(V'_{/r})_z}{|\mathbf{V}'_{/r}|} (\Delta V'_{/r})_z + \frac{(V'_{/r})_t}{|\mathbf{V}'_{/r}|} (\Delta V'_{/r})_t + \frac{(V'_{/r})_s}{|\mathbf{V}'_{/r}|} (\Delta V'_{/r})_s \quad (3.144)$$

3.5.4. Modal reduction of aerodynamic states

Sønderby [62] has proposed a method for reduction of aerodynamic states by using as basis the slaves of structural mode shapes. In other words, the aerodynamic basis depicts the static aerodynamic response to a purely harmonic structural input with the structure oscillating at its fundamental modal frequency. In this model, the purely flapwise mode shapes have been used for reduction. The flapwise components are extracted from coupled blade modes, and these extracted shape functions form part of the basis function used to reduce the aerodynamic states.

3.5.5. Aerodynamic state space

The representation of linearized aerodynamic sub-modules has been shown in Eqn. 3.103. Manipulating Eqn. 3.103 we end up with a state space representation for the linearized aerodynamic module [48].

$$\begin{aligned}\mathbf{y}_a &= (\mathbf{I} - \mathbf{D}_{y,a})^{-1} \mathbf{C}_a \mathbf{x}_a + (\mathbf{I} - \mathbf{D}_{y,a})^{-1} \mathbf{D}_{u,a} \mathbf{u} \\ \frac{d\mathbf{x}_a}{dt} &= [\mathbf{A}_a + \mathbf{B}_{y,a} (\mathbf{I} - \mathbf{D}_{y,a})^{-1} \mathbf{C}_a] \mathbf{x}_a + [\mathbf{B}_{u,a} + \mathbf{B}_{y,a} (\mathbf{I} - \mathbf{D}_{y,a})^{-1} \mathbf{D}_{u,a}] \mathbf{u}\end{aligned}\quad (3.145)$$

3.6. Coupled aeroelastic equations

The final step in the derivation of the aeroelastic model is the coupling of the structural and aerodynamic models. The structural model defines the modal degrees of freedom and their first derivatives as the states of the system. The nodal aerodynamic forces in pitch coordinates are input from the aerodynamic model and represent the aeroelastic coupling. For the aerodynamic model, the induced velocity in axial and tangential direction, dynamic angle of attack and the circulation lag parameters for each element comprise the state vector. These may be further reduced as described in Section 3.5.4. The element-wise physical displacements and velocities of the structure are input from the structural dynamics model.

The non-linear model can be represented in state space as follows [48]:

$$\begin{bmatrix} \mathbf{N}_s & 0 \\ 0 & \mathbf{I} \end{bmatrix} \frac{d}{dt} \begin{bmatrix} \mathbf{x}_s \\ \mathbf{x}_a \end{bmatrix} = \begin{bmatrix} \mathbf{f}_s(\mathbf{x}_s, \mathbf{x}_a, \mathbf{u}) \\ \mathbf{f}_a(\mathbf{x}_s, \mathbf{x}_a, \mathbf{u}) \end{bmatrix} \quad (3.146)$$

where as mentioned earlier \mathbf{u} contains both the global inputs as well as the data exchanged between the aerodynamic and structural models.

Now referring to Eqn. 3.87 & Eqn. 3.145, the linear aeroelastic state space is constituted as [48]:

$$\begin{bmatrix} \mathbf{N}_s & 0 \\ 0 & \mathbf{I} \end{bmatrix} \frac{d}{dt} \begin{bmatrix} \Delta \mathbf{x}_s \\ \Delta \mathbf{x}_a \end{bmatrix} = \mathbf{A} \begin{bmatrix} \Delta \mathbf{x}_s \\ \Delta \mathbf{x}_a \end{bmatrix} + \mathbf{B} \Delta \mathbf{u} \quad (3.147)$$

The above equation represents the linearization about a steady state point. The state vector and the input vector are now expressed as small perturbations about the operating point.

4

Verification of linearization

This thesis project aims to present a highly accurate, precise linearization of a non-linear aeroelastic system for condition monitoring. To verify this linearization, a frequency domain study is performed. This chapter gives an overview of the methodology followed in frequency domain calculations. This is followed by a presentation of modal analysis results for different cases which sequentially build up to the full aeroelastic system. Starting with the cases of a parked wind turbine and wind turbine rotating in still air, we verify the performance of the structural model. Next, the aerodynamics is also included and we study the aeroelastic damping. Having verified the accuracy of the linear aeroelastic model, a modal reduction study is performed to look at the possibility of reducing the order of the aeroelastic system. Finally, the chapter concludes by applying the linearized model to the stability analysis of a wind turbine.

4.1. Methodology

The process of performing frequency domain analysis using a wind turbine aeroelastic model can be broadly divided into three main steps. Firstly, calculate the state of the wind turbine system when it is in equilibrium with its surroundings, that is, the steady state. The second step involves linearization of the non-linear aeroelastic equations about the steady state operating point. Now it is important to note here that it in general one can linearize about any operating point, even a non-equilibrium point if so desired. This means the first step is not strictly mandatory but it is the most common approach. Finally, one must perform eigenvalue analysis on the linearized state space to extract the eigenvectors and eigenvalues. All the necessary modal information including natural frequencies, damped frequencies, mode shapes, damping ratios, etc. can be obtained from the extracted eigenvectors and eigenvalues. These steps are explained below one by one.

4.1.1. Steady state point

The steady state point of operation is calculated using the Newton-Rhapson method. This is a very popular root finding numerical method for non-linear equations based on a single initial value guess.

We start by assuming an initial guess value for the states. The structural states are set to zero while the axial induction factor is taken to be $1/3$ at each section. At steady state, Eqn. 3.146 should be satisfied though the individual blades shall have finite accelerations and velocities. The dynamics have so far been expressed in rotating coordinates. Alternatively, we can choose to express the dynamics of rotating blades in terms of the Multi-blade coordinate (MBC) transforms. The advantage gained here is that derivatives of states corresponding to the rotating blades become zero at steady state.

The Multi-blade coordinate (MBC) transform has traditionally been used in the analysis of rotating structures such as helicopters and wind turbines for converting the dynamics of rotating structures from a rotating co-

ordinate system to a non-rotating, fixed coordinate system [6]. The dynamics of wind turbine blades are periodic in nature represented by terms containing cosine and sine functions of the blade azimuth angle Ψ in the equations of motion. MBC transformation eliminates this strong dependency on Ψ [6]. For inputs such as a wind gust, control input or tower-nacelle motion which apply to the rotor as a whole, MBC transformed states and outputs will present the integrated response of the blades [6]. This gives a useful physical interpretation because motion is now visualized in terms of rotor modes instead of individual blade modes. Similarly, the tower-nacelle sub-structure can now see the combined response of the blades instead of the individual blade response [6]. Bir [6] has pointed out that there is a common misconception that MBC is only applicable when the blades are identical. However, in the derivation done in [6] no such assumption was ever made, and in case the blades have different structural or aerodynamic properties then this should reflect in the system matrices [6]. The only assumption required for MBC is that the blades be spaced equally around the axis of rotation [6].

Consider a subspace of the system state \mathbf{x} comprising of a state associated with each blade. This is represented by the vector given as $[x_1^B \ x_2^B \ x_3^B]^T$, where the subscripts refer to the blade number. The MBC transform for the triplet of variables is represented as follows [46]:

$$\begin{bmatrix} x_1^B \\ x_2^B \\ x_3^B \end{bmatrix} = \mathbf{T}_\Psi^B \begin{bmatrix} x_0^\Psi \\ x_c^\Psi \\ x_s^\Psi \end{bmatrix} \quad (4.1)$$

Note that the superscript Ψ refers to the MBC transformed states. The subscripts 0 represents collective motion, c represents cosine component of rotor motion (along \mathbf{X}^T) and s represents sine component of rotor motion (along \mathbf{Y}^T) [46]. Accordingly \mathbf{T}_Ψ^B is given as [46]:

$$\mathbf{T}_\Psi^B = \begin{bmatrix} 1 & \cos \Psi & \sin \Psi \\ 1 & \cos(\Psi + 2\pi/3) & \sin(\Psi + 2\pi/3) \\ 1 & \cos(\Psi + 4\pi/3) & \sin(\Psi + 4\pi/3) \end{bmatrix} \quad (4.2)$$

The inverse transform, \mathbf{T}_B^Ψ is given as [46]:

$$\mathbf{T}_B^\Psi = \begin{bmatrix} \frac{1}{3} & \frac{1}{3} & \frac{1}{3} \\ \frac{2}{3} \cos \Psi & \frac{2}{3} \cos(\Psi + 2\pi/3) & \frac{2}{3} \cos(\Psi + 4\pi/3) \\ \frac{2}{3} \sin \Psi & \frac{2}{3} \sin(\Psi + 2\pi/3) & \frac{2}{3} \sin(\Psi + 4\pi/3) \end{bmatrix} \quad (4.3)$$

Note that any variable which has an association with each blade including blade motions, angle of attack, induced velocity, etc. can be transformed to non-rotating coordinates using MBC [6]. MBC is not applied to variables which do not have corresponding analogs for each blade.

Applying MBC to the full state vector and taking its derivative,

$$\begin{aligned} \mathbf{x}^B &= \mathbf{T}_{\Psi,x}^B \mathbf{x}^\Psi \\ \Rightarrow \frac{d\mathbf{x}^B}{dt} &= \Omega \frac{d\mathbf{T}_{\Psi,x}^B}{d\Psi} \mathbf{x}^\Psi + \mathbf{T}_{\Psi,x}^B \frac{d\mathbf{x}^\Psi}{dt} \end{aligned} \quad (4.4)$$

Note that $\mathbf{T}_{\Psi,x}^B$ represents the MBC transform for the full vector of states \mathbf{x} . This will transform rotating coordinates to non-rotating coordinates, and for states already in non-rotating coordinates it will simply multiply with the identity matrix. Substituting Eqn. 4.4 in Eqn. 3.146, and premultiplying with $\mathbf{T}_{B,x}^\Psi$ leads to [46]:

$$\mathbf{T}_{B,x}^\Psi \begin{bmatrix} \mathbf{N}_s & 0 \\ 0 & \mathbf{I} \end{bmatrix} \mathbf{T}_{\Psi,x}^B \frac{d\mathbf{x}^\Psi}{dt} = \mathbf{T}_{B,x}^\Psi \begin{bmatrix} \mathbf{f}_s(\mathbf{x}_s, \mathbf{x}_a, \mathbf{u}) \\ \mathbf{f}_a(\mathbf{x}_s, \mathbf{x}_a, \mathbf{u}) \end{bmatrix} - \Omega \mathbf{T}_{B,x}^\Psi \begin{bmatrix} \mathbf{N}_s & 0 \\ 0 & \mathbf{I} \end{bmatrix} \frac{d\mathbf{T}_{\Psi,x}^B}{d\Psi} \mathbf{x}^\Psi \quad (4.5)$$

At steady state, the derivatives of the states expressed in MBC become zero. Consequently, at steady state the RHS in Eqn. 4.5 must also reduce to zero. The solution is calculated iteratively using the following relation to update \mathbf{x} after each iteration [48].

$$\Delta \mathbf{x} = -\alpha_N \left(\frac{\partial \mathbf{f}}{\partial \mathbf{x}} \right)^{-1} \mathbf{f}(\mathbf{x}, \mathbf{u}) \quad (4.6)$$

where α_N is a scaling factor which ensures that the residual reduces after each iteration. Here the term $\left(\frac{\partial \mathbf{f}}{\partial \mathbf{x}} \right)$ is akin to matrix \mathbf{A} obtained from the linearization of the non-linear aeroelastic equations. It is chosen to calculate the residual as $\mathbf{f}^T \mathbf{f}$, and once this residual value falls below the user-specified convergence parameter the solution is said to be found. Note that despite its simplicity, the Newton-Rhapson method in practice only finds a local zero, not the global zeros of the non-linear system [16]. This essentially means that the solution is dependent on the initial condition specified.

4.1.2. Linearization

Once the steady state point has been obtained, it is possible to perform a linearization about that point as given in Eqn. 3.147. This linearization represents the change in the states and outputs of the system for small perturbations in inputs. The linearized state space is however not suitable for modal analysis as it contains periodic terms. Secondly, the state space matrices are not numerically well conditioned for modal analysis [6].

Here too, the MBC proves very useful. The MBC transform acts as a filter removing all periodic terms except those whose frequencies are $n\Omega$, where n is any positive integer [6]. Even those periodic terms which remain have relatively small magnitudes. Also, the MBC application renders the linear state space matrices numerically well conditioned [6].

Linearizing the expression in Eqn. 4.4, we get [46]:

$$\begin{aligned} \Delta \mathbf{x} &= \mathbf{T}_{\Psi,x}^B \Delta \mathbf{x}^\Psi \\ \frac{d\Delta \mathbf{x}}{dt} &= \Omega \frac{d\mathbf{T}_{\Psi,x}^B}{d\Psi} \Delta \mathbf{x}^\Psi + \mathbf{T}_{\Psi,x}^B \frac{d\Delta \mathbf{x}^\Psi}{dt} + \frac{d\mathbf{T}_{\Psi,x}^B}{d\Psi} \mathbf{x}^\Psi \frac{\partial \Omega}{\partial \mathbf{x}} \mathbf{T}_{\Psi,x}^B \Delta \mathbf{x}^\Psi \end{aligned} \quad (4.7)$$

Note that the last term arises because the rotor speed Ω is some function of the nodal orientations and their rates of change [48]. So,

$$\Omega = f_\Omega(\mathbf{x}) \Rightarrow \Delta \Omega = \frac{d\Omega}{d\mathbf{x}} \Delta \mathbf{x} \quad (4.8)$$

Substituting Eqn. 4.7 in Eqn. 3.147 we get,

$$\begin{aligned} \mathbf{T}_{B,x}^\Psi \begin{bmatrix} \mathbf{N}_s & 0 \\ 0 & \mathbf{I} \end{bmatrix} \mathbf{T}_{\Psi,x}^B \frac{d\Delta \mathbf{x}^\Psi}{dt} &= \left(\mathbf{T}_{B,x}^\Psi \mathbf{A} \mathbf{T}_{\Psi,x}^B - \Omega \mathbf{T}_{B,x}^\Psi \begin{bmatrix} \mathbf{N}_s & 0 \\ 0 & \mathbf{I} \end{bmatrix} \frac{d\mathbf{T}_{\Psi,x}^B}{d\Psi} - \mathbf{T}_{B,x}^\Psi \begin{bmatrix} \mathbf{N}_s & 0 \\ 0 & \mathbf{I} \end{bmatrix} \frac{d\mathbf{T}_{\Psi,x}^B}{d\Psi} \mathbf{x}^\Psi \frac{\partial \Omega}{\partial \mathbf{x}} \mathbf{T}_{\Psi,x}^B \right) \Delta \mathbf{x}^\Psi + \\ &\quad \mathbf{T}_{B,x}^\Psi \mathbf{B} \mathbf{T}_{\Psi,u}^B \Delta \mathbf{u}^\Psi \end{aligned} \quad (4.9)$$

Here, $\mathbf{T}_{B,x}^\Psi$ and $\mathbf{T}_{B,u}^\Psi$ are the MBC transformations for the state and input matrices respectively.

To further remove the azimuthal dependence in the state space, the linearization is performed for a number of different azimuthal angles and then the corresponding matrices are averaged.

4.1.3. Eigenvalue analysis

Having obtained a linearized state space representation for the aeroelastic system which is numerically well conditioned and free of all unnecessary periodicity, it is now possible to formulate a general eigenvalue problem for modal analysis. Let us represent Eqn. 4.9 in a simpler form as given below :

$$\mathbf{L}^\Psi \frac{d\Delta\mathbf{x}^\Psi}{dt} = \mathbf{A}^\Psi \Delta\mathbf{x}^\Psi + \mathbf{B}^\Psi \Delta\mathbf{u}^\Psi \quad (4.10)$$

Assume $\Delta\mathbf{x}^\Psi = c \exp(\mathbf{k}t)$, and substitute in the above equation. Ignoring the inputs for once, we get :

$$\mathbf{k}\Delta\mathbf{x}^\Psi = (\mathbf{L}^\Psi)^{-1} \mathbf{A}^\Psi \Delta\mathbf{x}^\Psi \quad (4.11)$$

This is the final form of the eigenvalue problem which is numerically solved to obtain the system aeroelastic frequencies, shape functions and damping. The system eigenvalues and eigenvectors are generally obtained in complex form. The three isolated blade modes will combine to give three rotor modes for the full wind turbine system. Considering the 1st blade edgewise modes, we get the collective edgewise mode in which all blades vibrate in unison. Then there are the two asymmetric modes, in which the blades vibrate within the plane of the rotor such that the center of mass of the rotor whirls either in the same or opposite direction to the rotor spin. These modes are respectively named as the forward whirl and backward whirl edgewise rotor modes. For an isolated three-bladed rotor in vacuum, the forward and backward whirl edgewise modes differ from the collective blade edgewise mode by Ω and $-\Omega$ respectively in terms of frequency. The 1st flapwise modes of the blades similarly decompose into three rotor modes, namely the collective, forward whirl and backward whirl flapwise rotor modes.

4.2. Parked wind turbine

In this section, the case of a parked wind turbine at standstill is analyzed primarily with the aim to verify the structural model. The NREL 5MW Baseline wind turbine as defined by Jonkman et al. [34] is the turbine chosen for analysis in this section as it is throughout this thesis. A modally reduced aeroelastic model is used for this analysis, as it is throughout this chapter, unless stated otherwise. The structure is expressed in terms of 10 modes for the foundation and tower each, 2 modes for the nacelle and driveshaft each and 16 modes per blade. The aerodynamic degrees of freedom are not reduced. Now it is imperative to mention here that STAS Aeroelastic is a general purpose tool which can be used for offshore turbines, and the foundation in that case would represent the offshore support structure as well as the soil damping and stiffness effects. To maintain that generality the tower for the onshore part is split into two equal halves with the foundation representing the lower half of the actual tower. The foundation-tower combine defined is identical to the the actual tower defined in [34], and the joint between them is modelled as completely rigid.

4.2.1. Body modes

To start with, an eigenvalue analysis is performed only on the structural model to determine the isolated modes for each sub-structure of the wind turbine. By the term isolated, it is meant that an eigenvalue problem is formulated only in terms of the structural degrees of freedom for a particular sub-structure of the wind turbine. These modes will be used later for modal reduction of the structure in the aeroelastic model.

Figs. 4.1 & 4.2, Figs. 4.3 & 4.4 show the mode shapes for the tower side-to-side and fore-aft motions of the NREL 5MW turbine respectively. Note that the mode shapes names are misleading to the extent that the depicted modes are coupled and also include other types of motion besides the dominant motion after which the mode is named.

Similarly, Figs. 4.5 & 4.6, Figs. 4.7 & 4.8, Fig. 4.9 show the mode shapes for the blade flapwise, edgewise and torsional modes respectively. Since the blades are assumed to be identical these modes will be the same for

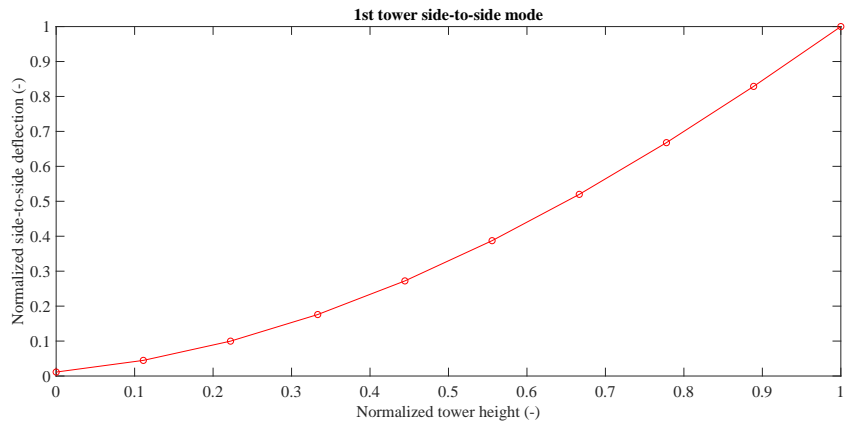


Figure 4.1: 1st tower side-to-side mode shape for NREL 5MW Baseline turbine

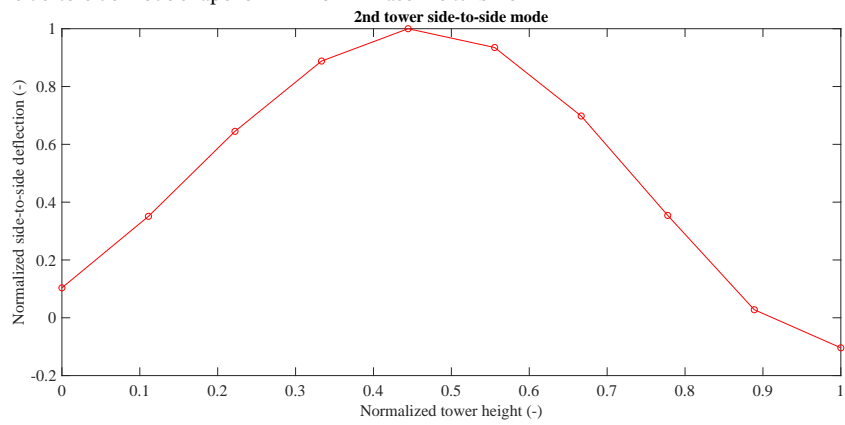


Figure 4.2: 2nd tower side-to-side mode shapes for NREL 5MW Baseline turbine

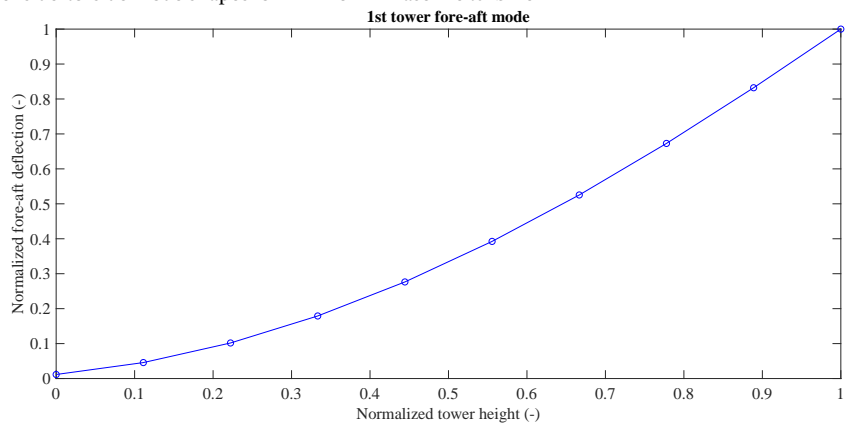


Figure 4.3: 1st fore-aft mode shape for NREL 5MW Baseline turbine

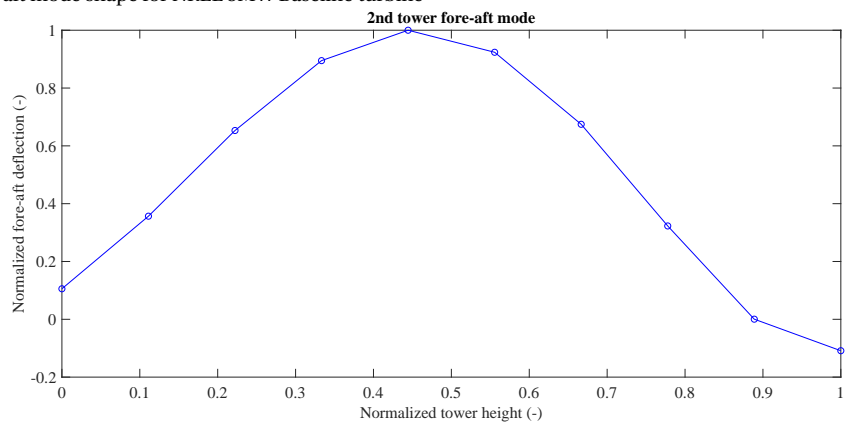


Figure 4.4: 2nd tower fore-aft mode shape for NREL 5MW Baseline turbine

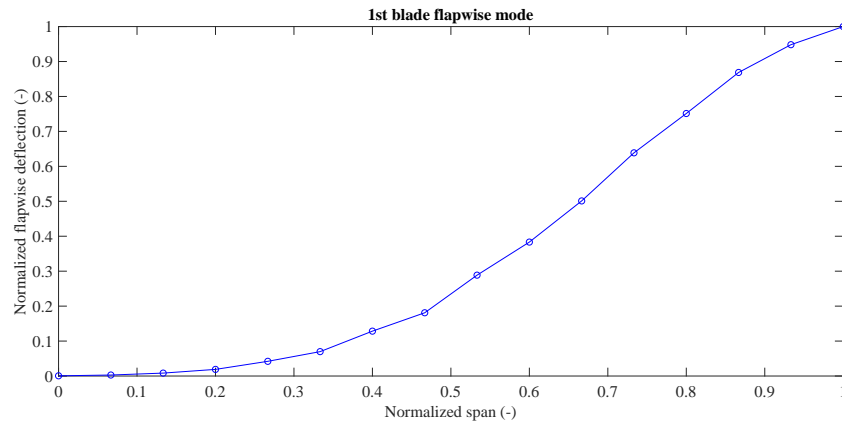


Figure 4.5: 1st blade flapwise mode shape for NREL 5MW Baseline turbine

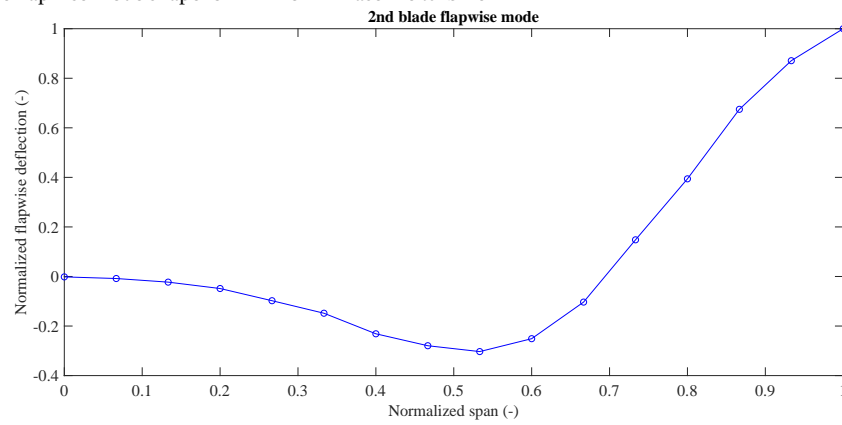


Figure 4.6: 2nd blade flapwise mode shape for NREL 5MW Baseline turbine

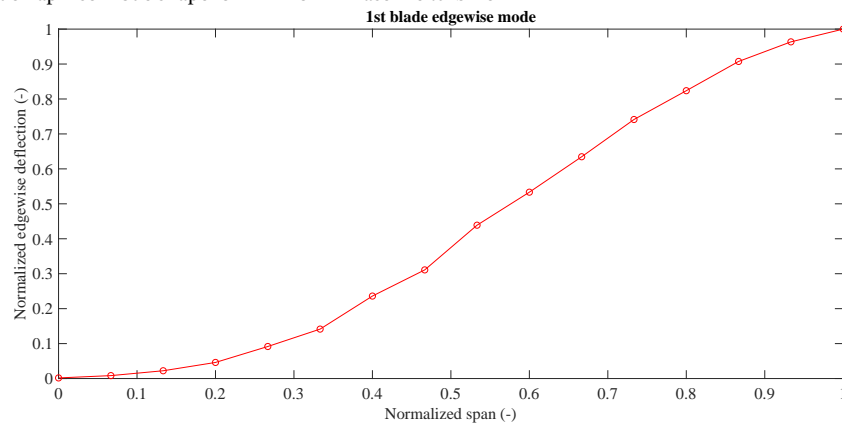


Figure 4.7: 1st blade edgewise mode shape for NREL 5MW Baseline turbine

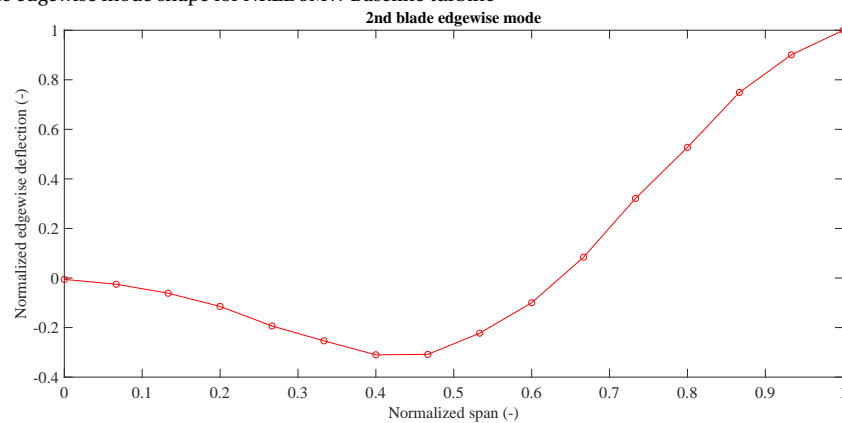


Figure 4.8: 2nd blade edgewise mode shape for NREL 5MW Baseline turbine

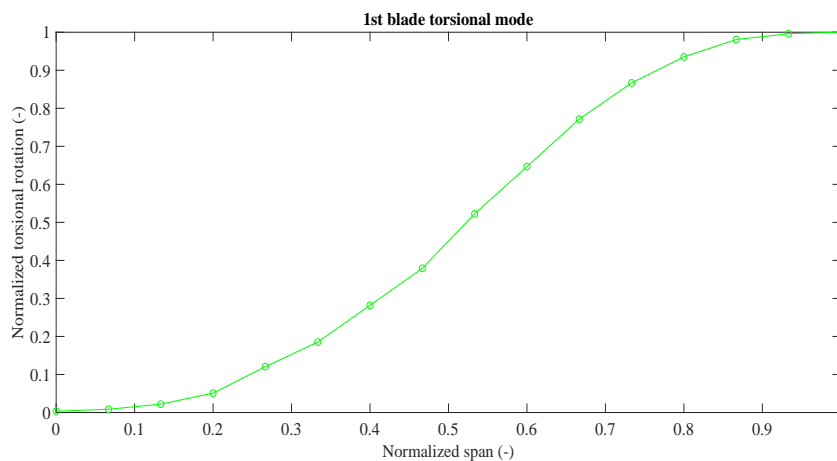


Figure 4.9: 1st blade torsional mode shape for NREL 5MW Baseline turbine

Table 4.1: Natural frequencies of body modes (in Hz)

Mode	STAS Aeroelastic	BModes
1st tower side-to-side	0.652	0.649
1st tower fore-aft	0.677	0.671
2nd tower side-to-side	2.988	3.041
2nd tower fore-aft	3.815	3.906
1st driveshaft torsion	0.702	-
1st blade flapwise	0.729	0.696
1st blade edgewise	1.114	1.175
2nd blade flapwise	2.113	1.960
2nd blade edgewise	4.222	4.047
1st blade torsion	11.412	-

each blade and hence it suffices to show them for one blade. The frequencies of the corresponding body modes are given in Table 4.1. These have been compared against the frequencies for NREL 5MW turbine's tower and blade obtained using BModes. BModes is a finite element code, developed at NREL, which outputs coupled modes for a wind turbine tower and blade.

In general, there is good agreement. The tower modes are well predicted but the blade flapwise modes differ somewhat with STAS Aeroelastic predicting a slightly higher value. This points to minor differences in the implementation of the beam model. Overall the stiffness and mass matrices corresponding to the tower and blades are verified to be correct.

4.2.2. Full system modes

Since the isolated tower and blade modes have been verified we can now derive the modes of a fully assembled wind turbine system. Considering the blades to be at standstill in vacuum gives the possibility to test the assembled structural model and the applied constraints. The blades are not rotating so the MBC transform is not applied before the eigenvalue analysis. The results obtained from the STAS Aeroelastic code are verified against results from FAST v8.16. A similar study was done by Merz [48]. Since the rotor is stationary, here it is imperative to point out that the two asymmetric rotor modes couple with the yaw and tilt motion of the tower respectively [44]. They are accordingly named as the blade flapwise (or edgewise) asymmetric tilt and blade flapwise (or edgewise) asymmetric yaw modes respectively. The comparison is shown in Table 4.2, which is similar to [48] with the addition that the 1st edgewise collective mode is also published.

Again, a reasonably good agreement is obtained suggesting that the assembled structural model is correct. There are however some small differences. STAS predicts the driveshaft torsion mode to be lower. This is

Table 4.2: Natural frequencies (in Hz) of full wind turbine model

Wind turbine mode	STAS Aeroelastic	FAST v8.16
	Nat. frequency (Hz)	Nat. frequency (Hz)
1st tower side-to-side	0.316	0.314
1st tower fore-aft	0.321	0.324
2nd tower side-to-side	3.031	2.954
2nd tower fore-aft	2.922	2.915
1st driveshaft torsion	0.561	0.620
1st blade asymmetric flapwise tilt	0.669	0.667
1st blade asymmetric flapwise yaw	0.679	0.675
1st blade collective flapwise	0.752	0.699
1st blade asymmetric edgewise tilt	1.106	1.081
1st blade asymmetric edgewise yaw	1.123	1.092
1st blade collective edgewise	3.844	3.682
2nd blade asymmetric flapwise tilt	1.797	1.911
2nd blade asymmetric flapwise yaw	1.860	1.984
2nd blade collective flapwise	2.138	2.007

because the drivetrain model used here is a direct drive one, whereas FAST uses a geared drivetrain for the NREL 5MW turbine. This difference in drivetrain modelling also influences the 1st blade edgewise collective mode which couples strongly with the drivetrain torsion mode. In general, the 1st blade flapwise collective mode tends to remain close to the 1st flapwise mode for the isolated blade. Here, STAS Aeroelastic predicts a higher value for the collective flapwise mode. Actually, this carries over from the isolated blade modes where too a larger frequency for the 1st blade flapwise mode was predicted. On closer analysis it was found that this difference in the collective flapwise modes is likely due to one inherent assumption in the beam model. FAST uses a 6th order polynomial as an assumed shape function for displacements while STAS uses a 3rd order shape function. When the order of the shape function in FAST is progressively reduced from six to four and then to three, it is found that the 1st collective flapwise frequency as well as the 1st edgewise rotor modes increase and become closer to those predicted by STAS. This verifies the assembled structural model for the wind turbine system and the connecting constraint equations.

4.3. Campbell diagram

A Campbell diagram, showing the variation of the modes of the full wind turbine system with rotational speed can also be plotted. Here the calculations for the Campbell diagram are made at zero wind speed, thus ignoring the aerodynamics. Two plots depicting the Campbell diagram for the NREL 5MW reference turbine made using STAS Aeroelastic and FAST are shown in Figs. 4.10 & 4.11 respectively.

In general, we can deduce two main things from the Campbell diagram. Firstly, the Campbell diagram should be able to tell us if the MBC transformation has been applied correctly. This we can deduce by looking at the backward and forward whirl rotor modes. Secondly, the Campbell diagram should also capture the centrifugal stiffening effect. Centrifugal stiffening effect is an effect observed in rotating blades wherein the centrifugal force acting on a blade has a component in the flapwise direction which opposes flapwise motion. The blade is said to have an extra stiffness in the flapwise direction, and the centrifugal stiffening effect on the natural frequency is proportional to $(1 + \Omega^2)^{1/2}$ [65].

Looking at the Campbell diagram in Fig. 4.10, we find the isolated blade modes split into the forward and backward whirl modes, as was to be expected. Moreover, the difference in frequency between the backward and forward whirl modes in the flapwise and edgewise directions is very close to 2Ω for all rotor speeds. This means that the MBC transformation has been applied correctly. The two whirl modes are however not located symmetrically about the collective blade modes. Bir et al. [7] have explained this happens because the different rotor modes interact differently with the nacelle-tower sub-assembly. Comparing the 1st & 2nd blade collective flapwise modes shown in Figs. 4.10 & 4.11, an estimate for the centrifugal stiffening effect

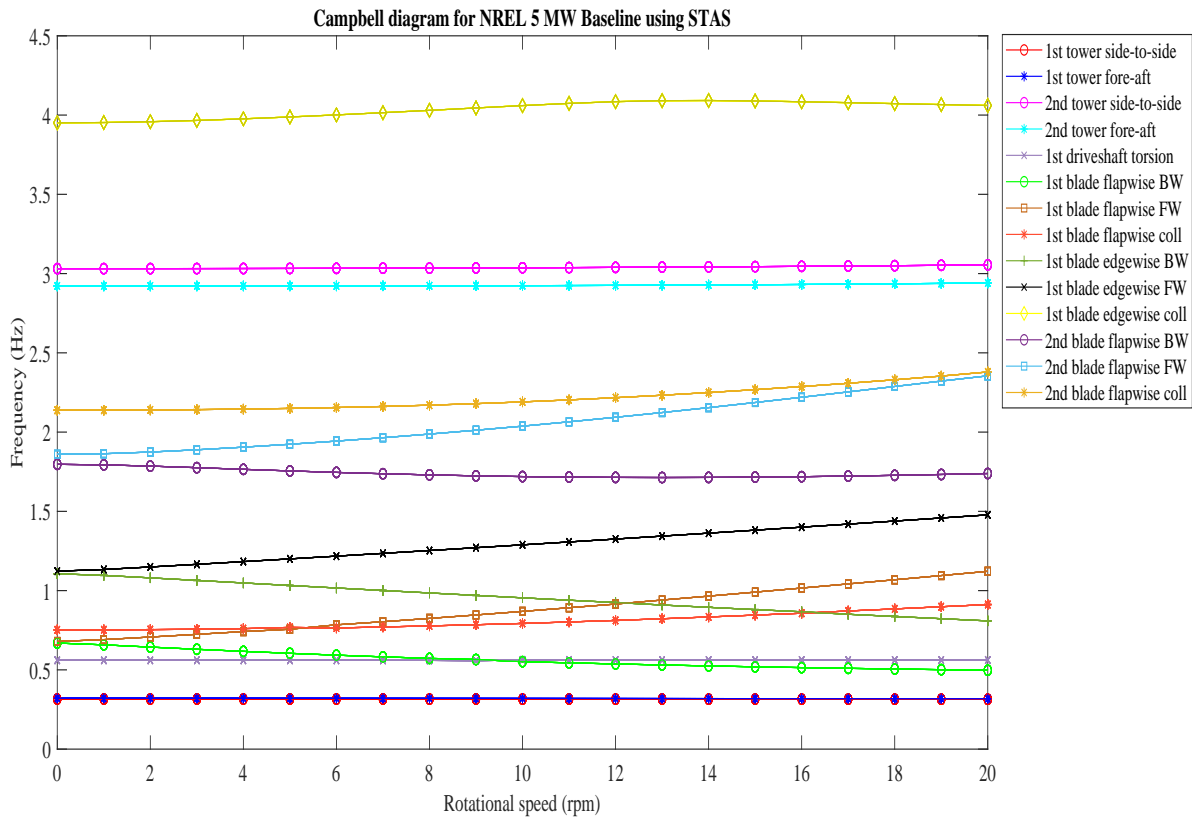


Figure 4.10: Campbell diagram for NREL 5MW turbine using STAS Aeroelastic

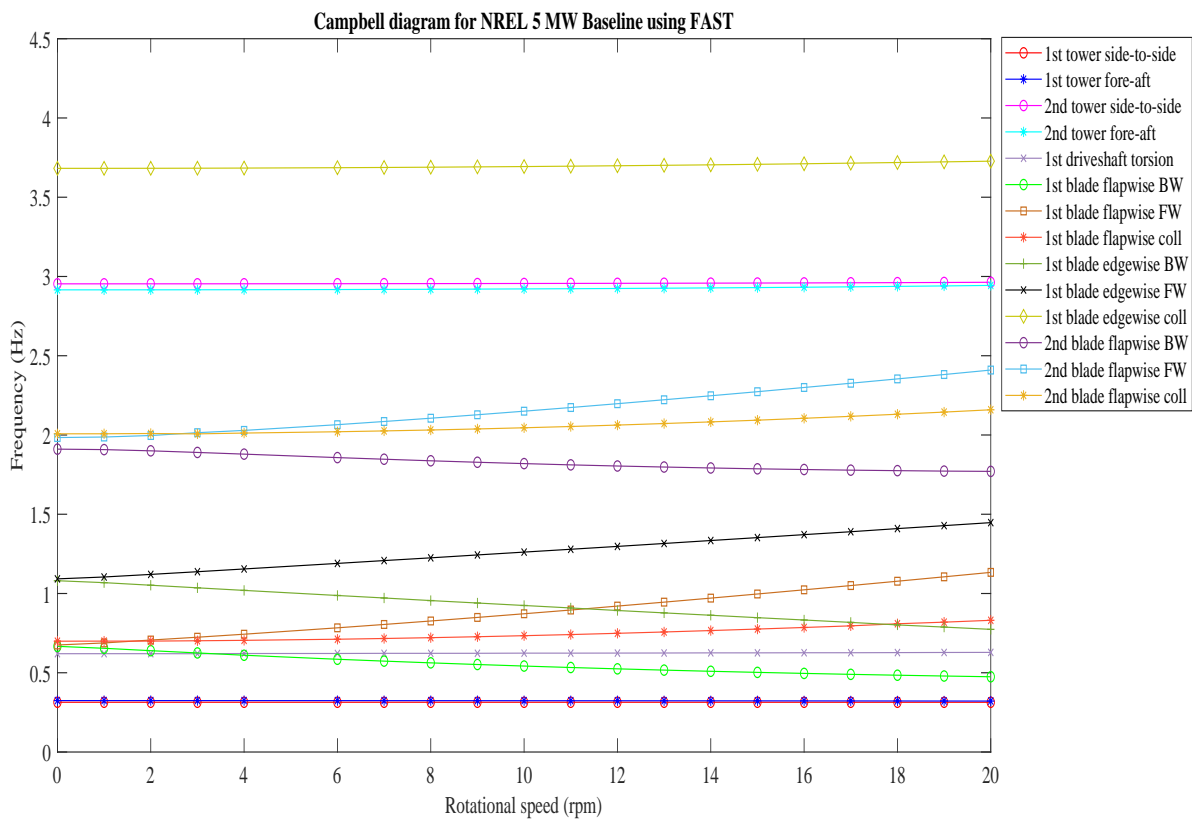


Figure 4.11: Campbell diagram for NREL 5MW turbine using FAST v8.16

Table 4.3: Comparison of centrifugal stiffening : Increase in natural frequency (Ω varies from 0 to 20 rpm).

Mode	% Increase for STAS Aeroelastic	%Increase for FAST v8.16
1st blade collective flapwise	21%	19%
2nd blade collective flapwise	11%	7.5%

is obtained. The percentage increase in the 1st & 2nd blade collective flapwise modes over the full range of the rotor speed is given in Table 4.3. The results compare very well, though STAS Aeroelastic predicts slightly greater centrifugal stiffening especially for the 2nd blade collective mode. However, this is deemed to be acceptable and hence the centrifugal stiffening effect in the linear model stands verified.

4.4. Aeroelastic damping

An important characteristic of any aeroelastic system is the aeroelastic damping of the various modes. Aeroelastic damping refers to the combination of pure structural damping and aerodynamic damping, that is, aerodynamic forces which depend on the structural velocity. For purposes of stability analysis, it is imperative that aeroelastic damping is accurately predicted.

A modal analysis is performed on the NREL 5MW Baseline wind turbine at steady state, operating at a uniform wind speed of 8 m/s, and the aeroelastic damping is extracted. But to gain insight into the individual contributions of the structure and aerodynamics to the damping, first we perform a modal analysis without the aerodynamics. The structural damping of a mode is dependent on the user specified value of ζ_d in Eqn. 3.85. To make the comparison of aerodynamic damping easier, ζ_d in STAS Aeroelastic is tuned for the various modes such that the structural damping matches as closely as possible to that predicted by FAST v8.16.

Merz [48] recommends to take a ζ_d value of 0.008 for all modes. Building on this, for this analysis we settle for a ζ_d value of 0.004, 0.015 & 0.005 for the tower, driveshaft and blade modes respectively. A comparison of the structural damping ratios for the various modes of a parked rotor is shown in Table 4.4. Note that damping ratios match well for the 1st modes but there is disparity in the damping ratios for the 2nd modes. Typically, higher modes also have higher structural damping ratios. However, the damping ratios for 1st and 2nd flapwise modes in FAST are not much different which is, qualitatively speaking, rather surprising. As was already explained when we looked at the full system modes of a parked wind turbine, the beam models for the tower and blade differ in terms of the assumed shape functions. This means that the elemental mass and stiffness matrices are not identical and when using Eqn. 3.85 differences are to be expected. Also, the 1st collective edgewise mode is known to couple strongly with the 1st drivetrain torsion mode however the extent of that coupling is also expected to be different considering the different drivetrain models in the two codes. This reflects somewhat in the damping ratios for this mode.

Subsequently, it is now possible to perform an eigenvalue analysis on the full aeroelastic system. A comparison of the mode natural frequencies and the corresponding aeroelastic damping values is given in Table 4.5 for the NREL 5MW wind turbine operating in normal power production mode at a uniform wind of 8 m/s. Quantitatively speaking, it is expected that getting a good match for the modal damping is rather difficult because generally speaking the matrices under consideration can still be described to be poorly conditioned numerically, though MBC application does improve this somewhat. It was found the eigenvalue analysis and especially the real part of the complex eigenvalues (which is much smaller than the imaginary part of the eigenvalues) is very sensitive to small changes in the model.

Instead, we choose to describe the results in a qualitative sense. The tower modes damping is explained in terms of the eigenvectors. The tower fore-aft modes have a significant amount of blade flapwise motion, and since flapwise motion has a large damping hence a much larger damping is predicted for tower fore-aft modes compared with side-to-side modes. The tower side-to-side modes do interact with the 1st collective edgewise mode but not to the same extent as the tower fore-aft mode does with 1st flapwise collective mode. Moreover, damping in edgewise direction is generally much lower than in flapwise direction. This trend is verified as the flapwise damping is greater than the edgewise damping by atleast a factor of 10. An increase in the aeroelastic natural frequencies for flapwise modes is observed. Hansen [26] observed a similar trend. Also Hansen [26]

Table 4.4: Structural damping ratio of system modes

Wind turbine mode	STAS Aeroelastic	FAST v8.16
	Damping ratio (-)	Damping ratio (-)
1st tower side-to-side	0.0034	0.0035
1st tower fore-aft	0.0033	0.0035
2nd tower side-to-side	0.0192	0.0100
2nd tower fore-aft	0.0150	0.0095
1st driveshaft torsion	0.0088	0.0094
1st blade asymmetric flapwise tilt	0.0050	0.0047
1st blade asymmetric flapwise yaw	0.0047	0.0047
1st blade collective flapwise	0.0057	0.0055
1st blade asymmetric edgewise tilt	0.0057	0.0047
1st blade asymmetric edgewise yaw	0.0058	0.0048
1st blade collective edgewise	0.0109	0.0393
2nd blade asymmetric flapwise tilt	0.0081	0.0049
2nd blade asymmetric flapwise yaw	0.0061	0.0049
2nd blade collective flapwise	0.0065	0.0050

Table 4.5: Aeroelastic damping ratio of system modes

Wind turbine mode	STAS Aeroelastic		FASTv8.16	
	Nat. frequency (Hz)	Damping ratio (-)	Nat. frequency (Hz)	Damping ratio (-)
1st tower side-to-side	0.3249	0.0104	0.3139	0.0610
1st tower fore-aft	0.3283	0.0760	0.3342	0.0658
2nd tower side-to-side	2.9870	0.0287	2.9551	0.0104
2nd tower fore-aft	2.9129	0.1406	2.9140	0.0173
1st driveshaft torsion	0.7720	0.8850	0.6262	0.0267
1st blade asymmetric flapwise BW	0.6786	0.4571	0.5802	0.6576
1st blade asymmetric flapwise FW	0.9410	0.4467	0.8451	0.4543
1st blade collective flapwise	0.8765	0.2646	0.7195	0.522
1st blade asymmetric edgewise BW	0.9909	0.0054	0.9328	0.0166
1st blade asymmetric edgewise FW	1.3168	0.0112	1.2535	0.0121
1st blade collective edgewise	3.9861	0.0172	3.6939	0.0403
2nd blade asymmetric flapwise BW	2.2518	0.1090	1.8035	0.1433
2nd blade asymmetric flapwise FW	2.5199	0.1120	2.1134	0.1218
2nd blade collective flapwise	2.4767	0.0645	2.0178	0.1294

states that the blade edgewise forward whirl is typically more damped than the backward whirl mode. This is borne out by the STAS Aeroelastic tool results.

The most obvious difference between the codes is the damping of the 1st driveshaft torsion mode. STAS seems to predict an abnormally high value. This can be explained in terms of the torque controller. While STAS does not have a real torque controller or generator model, it simulates the generator torque by applying a counter-torque on a node of the driveshaft. Jonkman et al. [35] provide the following equation of generator torque (low speed shaft side) in the variable speed region for the NREL 5MW turbine:

$$Q_{gen} = 0.0255764 \times (\text{Gearbox ratio})^3 \left(\frac{60\Omega}{2\pi} \right)^2 \quad (4.12)$$

It makes sense to model the same equation in STAS. However, convergence issues were encountered in the steady state solver when using the relation in Eqn. 4.12. Instead, an approximate relation proportional to Ω was compiled as given below.

$$Q_{gen} = 5 \times 10^7 (\Omega_{measured} - \Omega_{target}) \quad (4.13)$$

By tuning the value of Ω_{target} the steady state points of NREL 5MW turbine in power production mode were replicated. Inadvertently, the usage of Eqn. 4.13 leads to the STAS model having a torsional damping approximately 10 times higher than the values in FAST.

4.5. Modal reduction study

It is preferable to reduce the number of modes used to represent the aeroelastic system for the purpose of simplified frequency domain analysis and faster time marching simulations. This, however, is not straightforward because the full system modes of an aeroelastic system contain varying contributions from body modes of all the different sub-structures. Theoretically, excluding a tower mode may affect a blade mode and vice versa. High frequency modes are known to be highly damped in comparison to low frequency modes, and thus contribute less to the overall motion. This begs the question as to how many modes are sufficient to capture the important dynamics of the system.

A convergency study is performed to look at the effect of reduction in number of structural modes on damped frequency. The damped frequencies and the corresponding mode shapes capture in a nutshell the coupling of different structural motions in a mode. Coupling with a particular structural motion may increase or decrease the stiffness and damping of a mode thereby affecting the mode shape and the damped frequency.

Since the idea is to reduce the structural modes first, we looked at the case of the NREL 5MW reference wind turbine parked in still air. Starting with the unreduced aeroelastic model, the model is subsequently reduced in terms of the body modes. Taking any sub-structure, say the blades for example, the number of modes are gradually reduced and for each instance a modal analysis is performed to capture the effect on the damped frequencies of the main modes of the system. This analysis is performed for one sub-structure at a time meanwhile keeping the number of modes for the other sub-structures as fixed.

The results of the convergency analysis are presented for the blade in Table 4.6. A full unreduced blade contains 16 elements per blade. This corresponds to 17 nodes and 102 degrees of freedom per blade. The modal reduction step slightly modifies the asymmetric flapwise modes such that the 2nd blade asymmetric flapwise yaw mode increases by 6.7%. The damped frequencies remain stable as the number of modes is further decreased. As we reduce from 5 to 4 modes per blade the collective edgewise mode shoots up by 10.9%.

At this point the question arises whether the collective edgewise mode can be neglected altogether for purposes of aeroelastic stability analysis. It is often seen that the 1st collective edgewise blade mode couples strongly with the 1st driveshaft torsion mode and hence is considerably well damped in comparison to the asymmetric edgewise modes. However, Vatne's [64] work on studying instabilities in a 10 MW turbine has

Table 4.6: Convergency analysis for blade structural modes

Wind turbine mode	Damped frequency (in Hz)				
	No reduction	16 modes/blade	10 modes/blade	5 modes/blade	4 modes/blade
1st tower side-to-side	0.3157	0.3159	0.3159	0.3159	0.3159
1st tower fore-aft	0.3204	0.3206	0.3206	0.3206	0.3206
2nd tower side-to-side	3.0143	3.0311	3.0313	3.0331	3.0374
2nd tower fore-aft	2.9196	2.9218	2.9221	2.9249	2.9401
1st driveshaft torsion	0.5599	0.5607	0.5607	0.5607	0.5607
1st blade asymmetric flapwise tilt	0.6279	0.6691	0.6691	0.6691	0.6691
1st blade asymmetric flapwise yaw	0.6525	0.6791	0.6791	0.6791	0.6791
1st blade collective flapwise	0.7515	0.7522	0.7522	0.7522	0.7522
1st blade asymmetric edgewise tilt	1.1003	1.1063	1.1063	1.1063	1.1063
1st blade asymmetric edgewise yaw	1.1177	1.1227	1.227	1.1227	1.1227
1st blade collective edgewise	3.8007	3.8442	3.8453	3.8628	4.2800
2nd blade asymmetric flapwise tilt	1.6955	1.7966	1.7966	1.7971	1.7997
2nd blade asymmetric flapwise yaw	1.7416	1.8596	1.8596	1.8600	1.8620
2nd blade collective flapwise	2.1346	2.1379	2.1379	2.1379	2.1380

Table 4.7: Overview of reduced model

Body	Number of modes/DOFs		
	Full unreduced model	Reduced state 1	Reduced state 2
Foundation	126	10	5
Tower	66	10	5
Nacelle	54	2	2
Driveshaft	60	2	2
Blade	102	16	5
Joints	6	6	6
Total DOFs/modes after eliminating constraints	579	72	29

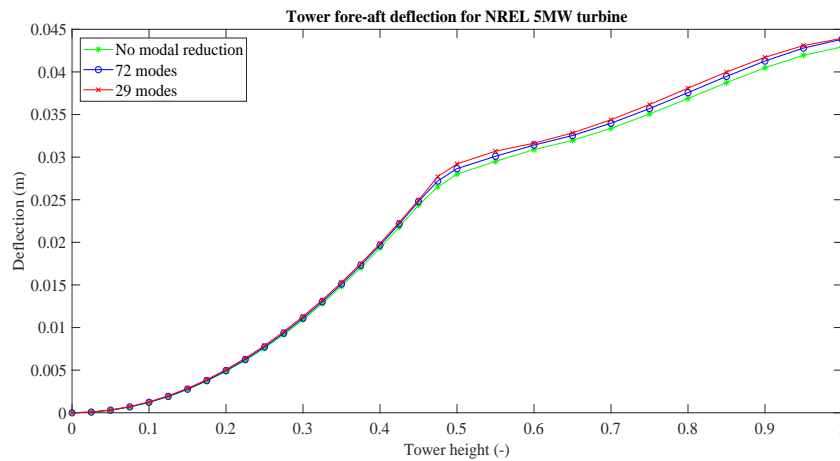


Figure 4.12: Tower fore-aft deflection for NREL 5MW Baseline turbine at 8m/s

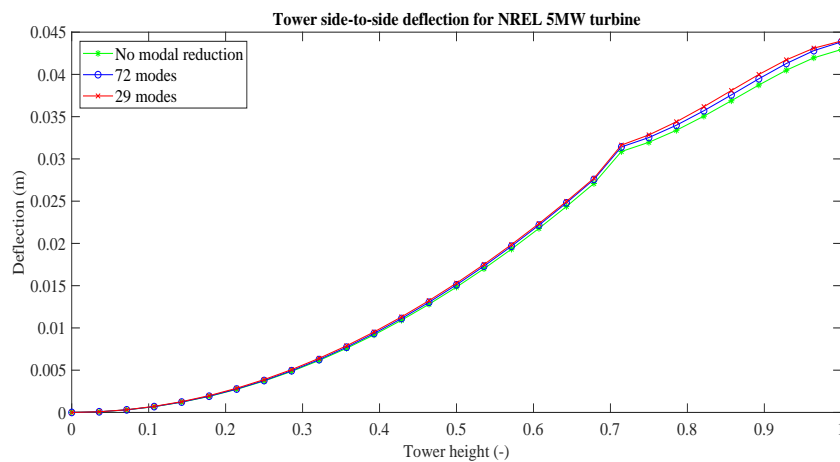


Figure 4.13: Tower lateral deflections for NREL 5MW Baseline turbine at 8m/s

shown that the 1st collective edgewise blade mode can become unstable for operation at high tip speed ratios so we will retain this mode. In case, it becomes poorly damped its contribution to edgewise deflections may be significant for such cases. Also for purposes of an aeroelastic stability analysis tool it makes sense to retain the 1st collective edgewise blade mode and to predict it accurately. Thus the modal reduction for the blade is terminated at 5 modes per blade.

A similar modal reduction study was performed for the other wind turbine sub-structures, namely, the foundation, tower, nacelle and driveshaft. The foundation and tower can be represented by 5 structural modes each. All modal frequencies, except the 2nd tower fore-aft mode, remain unchanged on further reducing the number of foundation and tower modes. The driveshaft and nacelle can be reduced to 2 modes each. Further reduction causes a jump in the 1st & 2nd asymmetric flapwise tilt blade mode. An overview of the reduced model is given in Table 4.7.

Furthermore, to verify if the proposed reduction in terms of convergence of the damped frequency is indeed feasible the steady state deflections were calculated separately for the three models shown in Table 4.7. For this purpose, the NREL 5MW turbine is assumed to be in normal power production mode at a uniform wind velocity of 8m/s. The tower fore-aft and lateral deflections are shown in Figs. 4.12 & 4.13 respectively. The tower deflections match excellently for the full unreduced model and the two reduced models. Similarly, the blade flapwise and edgewise deflections are given in Figures 4.14 & 4.15. Again the steady state deflections match very well especially upto the mid-span point. Beyond that "Reduced state 2" slightly underpredicts tip flapwise and edgewise deflections by 5.4% and 7.2% respectively. There is hardly any difference in deflections between "Reduced state 1" and "Reduced state 2" though. For the purposes of the study in this thesis, the

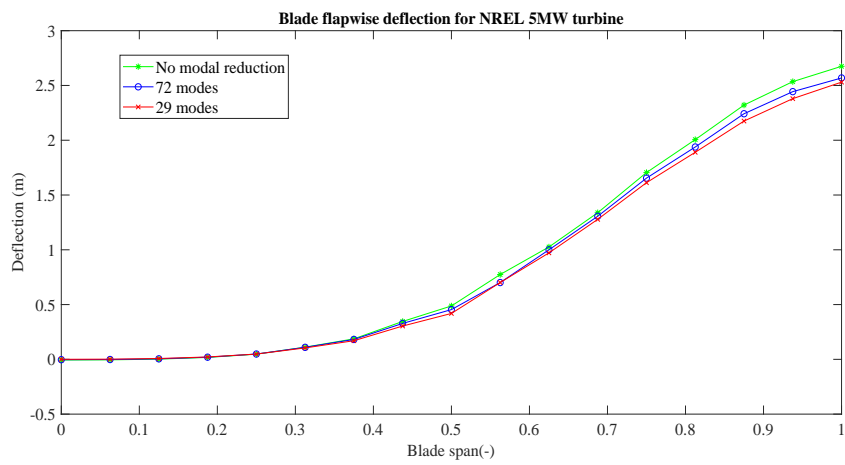


Figure 4.14: Blade flapwise deflections for NREL 5MW Baseline turbine at 8m/s

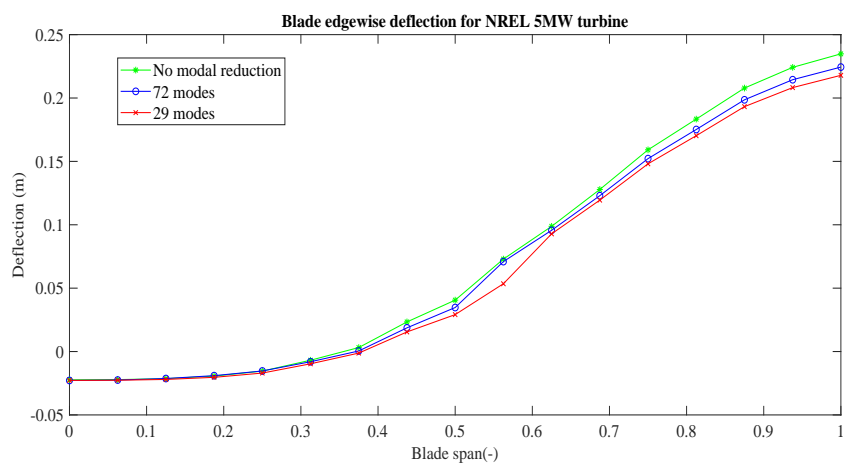


Figure 4.15: Blade edgewise deflections for NREL 5MW Baseline turbine at 8m/s

Table 4.8: Operating points for instability analysis [38]

Rotor speed (rad/s)	Wind speed (m/s)
1.0	3.8674
1.1	4.2541
1.2	4.6409
1.3	5.0276
1.4	5.4144
1.5	5.8011
1.6	6.1878
1.7	6.5746
1.8	6.9613
1.9	7.3481
2.0	7.7348
2.1	8.1215
2.2	8.5083
2.3	8.8950
2.4	9.2818
2.5	9.6685

difference in deflections is deemed acceptable and hence "Reduced state 2" with 29 structural modes can be used for future frequency domain analysis and time marching simulations.

4.6. Stability analysis

To demonstrate the capability of the linearized STAS Aeroelastic tool, a stability analysis study is performed on the NREL 5MW Baseline turbine. The idea is to see if the turbine is prone to flutter and at what operating conditions. The test for the tool is to predict the point of instability fairly accurately such that it can be useful to both wind turbine designers and operators.

Flutter is an aeroelastic instability describing self-sustained oscillations of a structure which grow without bound [32]. The point at which a damped oscillation transitions to one growing without bound is known as the flutter point [32]. In practice, the oscillations may not grow in bound and become limit cycle oscillations due to non-linearities in the structure and/or aerodynamics.

At certain conditions the phase difference between the motions of the structure and the aerodynamic forces becomes unfavourable such that net energy is being added to the structure over a cycle of oscillation. When the underlying mechanism of such an aeroelastic instability involves significant coupling of torsional and flapwise deflections then it is known as classical flutter. Vatne [64] has given the conditions under which classical flutter is likely to occur. First, the flow must be attached such that nose-up torsion leads to increased lift [64]. This would require relatively low angle of attack operation. Secondly, it is observed that for unfavourable phase difference between structural motion and aerodynamic forces to occur the center of mass of blade sections should generally be located aft of the aerodynamic center [64]. Thirdly, the blade should be sufficiently flexible in torsional direction for there to be significant coupling between blade torsional and flapwise deflections which are responsible for classical flutter [64].

Kallesøe et al. [38] studied the effect of large steady deformations on flutter stability. They concluded that steady state deformations do not have a significant influence on flutter limit. The flutter limit was found by performing modal analysis at a set of chosen operating points and looking out for negatively damped modes. The operating points given in Table 4.8 are chosen such that a constant angle of attack is maintained throughout while at the same time progressively increasing the rotor speed. For the analysis in STAS Aeroelastic, 10 blade modes are retained in the linear model to specifically include the blade torsional mode. In order to simplify the identification of modes, the foundation, tower, nacelle and driveshaft are assumed rigid and hence the modes representing these sub-structures are removed from the analysis. Also, we assume oscillations about the zero deflection point.

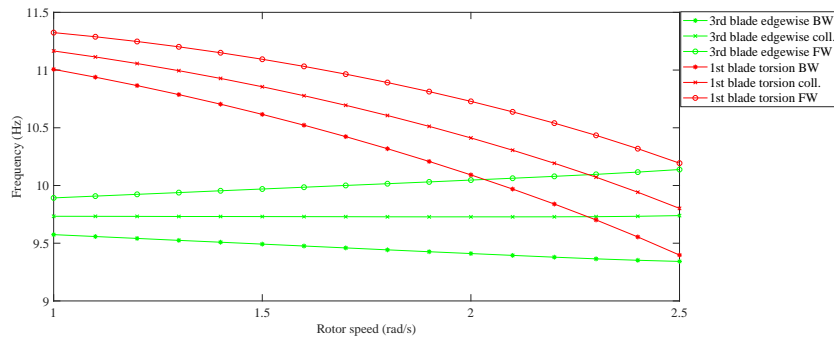


Figure 4.16: Natural frequency of modes relevant for stability analysis of NREL 5MW Baseline wind turbine

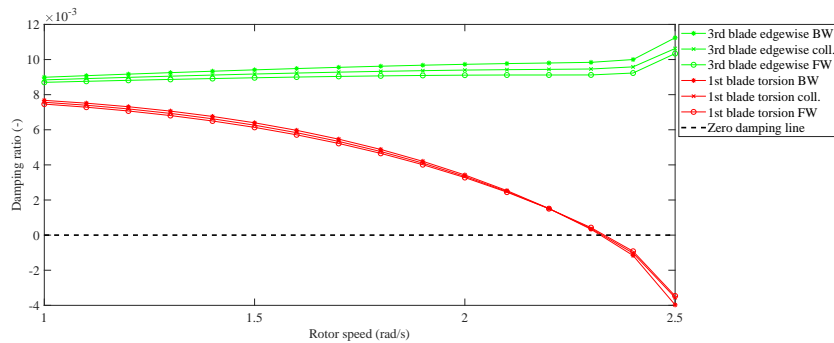


Figure 4.17: Damping ratio of modes relevant for stability analysis of NREL 5MW Baseline wind turbine

The results for the stability analysis are presented in Figs. 4.16 & 4.17. The rotor speed for flutter is predicted to be close to 2.35 rad/s. This matches exactly with the value obtained by Kallesøe et al. using HAWC2 [38]. Kallesøe et al. predict the 3rd flapwise mode to be the flutter mode, but in this study it is the 1st blade torsional mode which in fact becomes the flutter mode. The 1st blade torsional mode couples strongly with the 3rd blade edgewise mode. It contains significant torsional and flapwise motion. Even the edgewise mode contains significant flapwise motion. This is likely to be a case of classical flutter. It has also been pointed in field studies that another kind of instability due to coupling of blade torsional and edgewise modes may also occur [39]. This however is most likely under large steady state flapwise deflections which is not the case here.

Overall, the instability limit is predicted very accurately. This proves that the linearization is accurate. This also suggests that the aeroelastic damping values of modes are also accurate in a quantitative sense.

5

Time marching simulation tool

One of the goals in developing a reduced-order aeroelastic model, particularly relevant to condition monitoring and lifetime prediction, is to develop a time domain aeroelastic tool which can run simulations in real time. For a model-based condition monitoring system, this essentially means that such a tool can be used for comparing the critical outputs with data obtained from a condition monitoring system installed on an operational wind turbine for purposes of condition monitoring and fault detection. STAS Aeroelastic was originally developed as a highly precise linear aeroelastic model, but this tool is not optimized for running time marching simulations. This chapter describes the strategy used to implement a time marching simulation tool for the STAS Aeroelastic tool. The numerical integration is subsequently verified against results from test cases in FAST v8.16.

5.1. Introduction

In Chapter 3, the non-linear structural and aerodynamic models were developed independently. We know that these two models are strongly coupled together through the structural displacements and velocities of the blades as well as tower, and the aerodynamic forces acting on the blades. This translates into two different forms of representation relevant to numerical integration. In the monolithic representation, the aeroelastic system can be represented as a single set of differential equations, and these equations are integrated in time as one single entity [23]. Alternatively, in the partitioned representation the aeroelastic system can be represented separately in terms of the equations of its constituting subsystems or modules, namely the aerodynamic and structural models [23]. The two sets of differential equations are integrated separately over time and the coupling terms are transferred between the modules at each time step. The subsystems or modules are said to be loosely coupled [23]. The aerodynamics are represented by first order differential equations while the structure is represented in terms of second order differential equations. A partitioned approach makes it possible to apply different numerical integration schemes, time step sizes and space discretization for these two disparate modules [23].

Broadly speaking, all numerical integration schemes can be classified as either explicit or implicit. For an explicit scheme, the unknowns can be determined completely in terms of known quantities. This means that for a time integration the unknowns can be determined in terms of the values at the previous time step [18]. An implicit scheme is used when there exists a coupling between the various differential equations of a system such that the value of an unknown at the current time step is dependent on values of that variable at both previous and future time steps [18]. Implicit integration involves solving systems in terms of matrices or using iterative procedures. Explicit integration methods have a limitation on the maximum time step size [18]. Implicit integration methods on the other can be unconditionally stable and in practice allow much larger time step sizes [18].

The loosely coupled partitioned system can be coupled either explicitly or implicitly [23]. An explicit coupling

will advance the solution in time based on shared information at previous time step. It is simple to implement however tends to suffer from numerical instabilities [23]. For an implicit loosely coupled partitioned system, the problem is formulated such that atleast one of the partitions requires information from a future time step. This method tends to be more numerically stable [23].

5.2. Methodology

Two main approaches were considered for implementation. The first is integrating the monolithic representation of the non-linear aeroelastic model. This is simple to implement as it only requires formulation of the aeroelastic model in terms of the combined non-linear state space. The modules are inherently coupled so there is no requirement to specify a mechanism for transfer of coupling terms between modules. Both explicit and implicit integration schemes can be used. The second is a more novel approach based on the Newton-Rhapson steady state solver and the partitioned linear aeroelastic model. The idea is to calculate the steady state of the non-linear aeroelastic system using the Newton-Rhapson method, and to linearize about this steady state. The linearized model is loosely partitioned and can be integrated over time for perturbations in wind velocity due to turbulence or changes in pitch angle.

The monolithic non-linear aeroelastic model was integrated first using the in-built ODE solver functions in Matlab. ODE45, a fifth-order Runge Kutta explicit scheme, which allows for variable time step size was implemented [53]. This method starts off with very small step sizes of the range of 10^{-6} seconds, and eventually jumps up to time steps of the order of 10^{-5} seconds. Another medium to low accuracy Matlab explicit solver, specifically developed for stiff systems, ODE15s [52] was used next for numerical integration. This method performs better than ODE45 with time steps in the range of 10^{-5} s but is still very slow. ODE15i, a fully implicit ODE solver was tried next to allow for a larger time step, but this method is strictly applicable to problems which can be stated in a fully implicit form, that is, a system which cannot be written in explicit form [52]. This is not true for the system which is in fact stated explicitly.

Finally, an alternative way to advance the system in time is by using multistep methods. These methods make use of solution values and their derivatives from previous time steps to define a polynomial function to represent the solution [16]. In contrast, Runge-Kutta methods are one-step methods based on solution values from the last time step [16]. An algorithm for a third order predictor-corrector type method known as the Adam-Bashforth-Moulton method is shown in Algorithm 1 for a constant time step. A constant time step of 5×10^{-3} seconds was achieved with this method.

Algorithm 1 Adam Bashforth Moulton method - 3rd order [16]

```

1:  $\dot{x} = f(t, x)$ ,  $x(t_0) = x_0$ 
2: Predict:  $x_{n+1}^p = x_n + h(\frac{23}{12}f_n - \frac{16}{12}f_{n-1} + \frac{5}{12}f_{n-2})$ 
3:  $m \leftarrow 1$ 
4: residual  $\leftarrow 1$ 
5: while  $m \leq 20$  || residual  $> 10^{-4}$  do
6:   Evaluate:  $\dot{x}_{n+1} = f(t_{n+1}, x_{n+1}^p)$ 
7:   Correct:  $x_{n+1} = x_{n+1}^p + h(\frac{9}{24}f_{n+1} + \frac{19}{24}f_n - \frac{5}{24}f_{n-1} + \frac{1}{24}f_{n-2})$ 
8:   residual =  $x_{n+1} - x_{n+1}^p$ 
9: end
10: Evaluate:  $\dot{x}_{n+1} = f(t_{n+1}, x_{n+1})$ 

```

The second approach in terms of the linear aeroelastic model involves first partitioning the aeroelastic system of equations developed in Eqn. 3.147 into the constituents given in Eqn. 3.145 & Eqn. 3.86. The main problem encountered in performing numerical integration is the size of $(\mathbf{I} - \mathbf{D}_{y,a})$ in Eqn. 3.145, whose inverse calculation at every time step is computationally very expensive. An attempt was made to reduce the size of $\mathbf{D}_{y,a}$ matrix in STAS Aeroelastic by eliminating intermediate aerodynamic output variables. For instance, the linearized aerodynamic module uses the perturbation in structural velocity vector for each node expressed in the airfoil coordinate system. However, the structural model only outputs the perturbation in structural velocity vector for each node expressed in the global coordinate system. The transformation takes place inside the aerodynamic state space, and entails an additional six variables for every node of the blades. In the

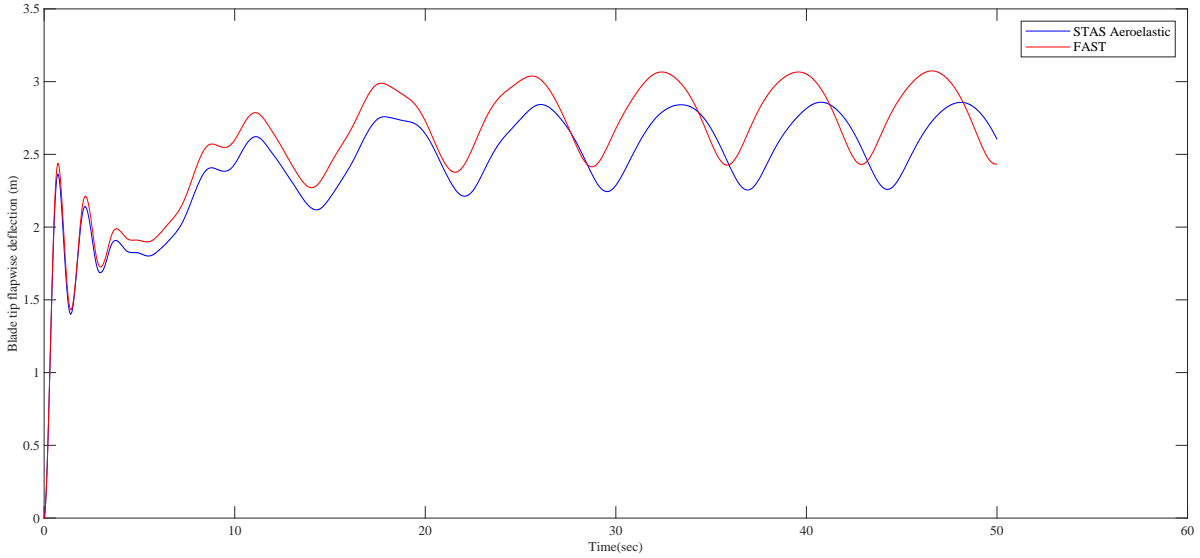


Figure 5.1: Comparison of time series for blade tip deflection in flapwise direction of NREL 5MW Baseline wind turbine at $V_\infty = 8\text{m/s}$.

modified code, such a transformation is applied inside the structural state space itself such that the perturbation in the structural velocity for each node is now only expressed in the airfoil coordinates. Similar to this case, many intermediate transformations yielding redundant output variables were all clubbed into a single transformation step to reduce the size of matrix $\mathbf{D}_{y,a}$.

The two partitions in the implicit loosely coupled aeroelastic linear system so obtained are integrated separately using the Adam-Bashforth-Moulton method described in Algorithm 1. The scheme can be broken down into three main steps [23].

1. Predict the structural state at t_{n+1} starting with past information using Adam-Bashforth-Moulton method.
2. Transfer predicted values to aerodynamic system, and solve for aerodynamic states at t_{n+1} using Adam-Bashforth-Moulton method.
3. Correct the structural state prediction using the predicted values for aerodynamic state at t_{n+1} . Multiple correction steps can be applied wherein steps 1 and 2 will also be repeated.

This integration scheme was implemented for the linear aeroelastic model for small perturbations in input velocity. However, problems were encountered in getting the solution to converge. Multiple correction steps were implemented and even the convergence criteria was relaxed, however convergence could not be achieved. It suffices here to say that numerical instability in loosely coupled systems can be expected since while transferring the coupling terms errors also tend to get propagated from one partition to the other. Further analysis is needed to pinpoint with certainty if this numerical error blow up is due to inherent problems with this coupling approach or implementation issues specific to this aeroelastic model. Such a study is however beyond the scope of this thesis.

5.3. Verification of time marching tool

The monolithic representation of the non-linear aeroelastic model, described in the previous section, is now verified against time marching results obtained from the non-linear aeroelastic model in FAST v8.16. Normal power production cases for the NREL 5MW Baseline turbine at uniform wind speeds of 8 m/s and 11.4 m/s were simulated until steady state is reached. This corresponds to a simulation time between 30 and 40 seconds for both STAS Aeroelastic and FAST. The turbine rotor is initially assumed to be spinning at 5 rpm with zero pitch. For STAS Aeroelastic there is no controller but the analytical torque speed relation for operation

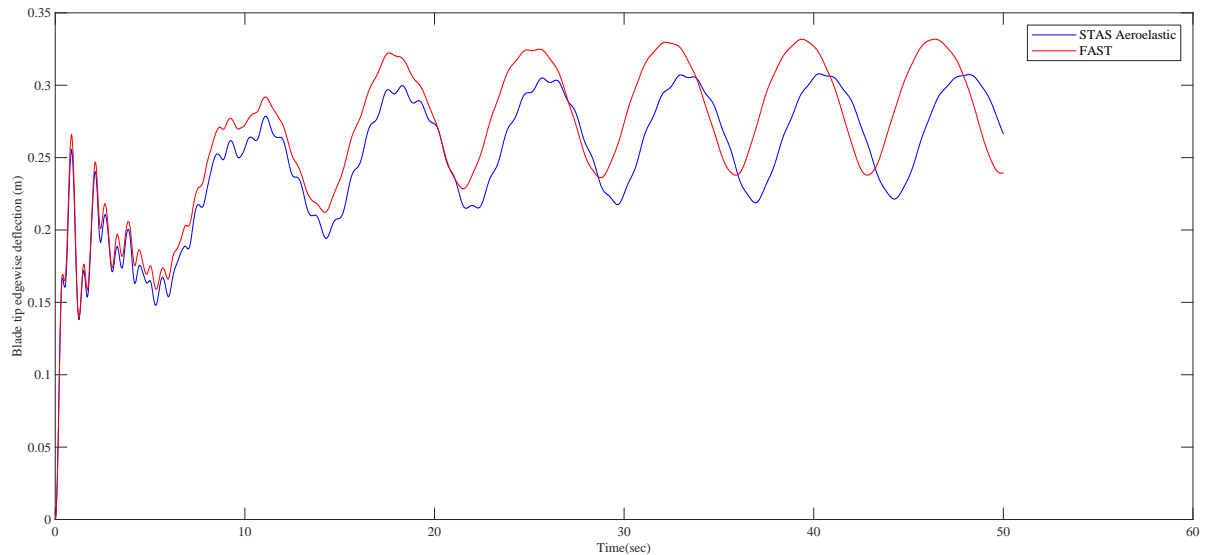


Figure 5.2: Comparison of time series for blade tip deflection in edgewise direction of NREL 5MW Baseline wind turbine at $V_{\infty} = 8\text{m/s}$.

Table 5.1: Comparison of time marching results

	STAS Aeroelastic		FASTv8.16	
	$V_{\infty} = 8\text{m/s}$	$V_{\infty} = 11.4\text{m/s}$	$V_{\infty} = 8\text{m/s}$	$V_{\infty} = 11.4\text{m/s}$
Rotor rotational speed (rpm)	9.09	12.15	9.14	12.05
Generator torque (Nm)	1.89×10^6	3.45×10^6	1.95×10^6	3.99×10^6
Rotor Power (W)	1.80×10^6	4.39×10^6	1.87×10^6	5.03×10^6
Rotor Thrust (N)	3.78×10^5	7.25×10^5	3.91×10^5	7.86×10^5
Blade out of plane tip deflection (m)	2.54	4.57	2.69	5.32
Blade in-plane tip deflection (m)	0.26	0.43	0.28	0.48
Blade root moment - in plane (Nm)	4.33×10^5	9.62×10^5	4.47×10^5	9.94×10^5
Blade root moment - out of plane (Nm)	4.10×10^6	7.60×10^6	4.55×10^6	8.50×10^6

region 2 of NREL 5MW turbine, given in Eqn. 4.12, is implemented. In FAST, the variable speed controller of the NREL 5MW Baseline turbine is switched on.

A summary of the results is presented in Table 5.1. The time series comparisons for STAS Aeroelastic and FAST are shown for blade tip deflections in flapwise and edgewise directions in Fig. 5.1 & Fig. 5.2 respectively. For a uniform wind speed of 8 m/s, the rotational speeds stabilize at the same value. The generator torque which is same as the aerodynamic torque at steady state only differs because of the marginal difference in rotor speed between the two models. The aerodynamic loads are slightly underpredicted, and this should also correspond to lower tip deflections. The tip deflections are certainly lower but there may be additional factors at work here. These can be explained looking back at the modal analysis results from Chapter 4. As was borne out in Section 4.2.2, STAS Aeroelastic predicts comparatively higher natural frequencies for the blade flapwise modes. Higher natural frequency implies higher stiffness in flapwise direction and this should contribute in some part to lower blade tip deflections in flapwise direction. In addition, the centrifugal stiffening effect studied in Chapter 4 was also found to be more pronounced for STAS Aeroelastic.

The results for wind speed of 11.4 m/s are interesting. FAST predicts a lower rotor speed but a considerably higher torque. The rotor power predicted by FAST is 13% greater than the power predicted with STAS Aeroelastic. This anomaly is easily explainable in terms of a change in operation of the default variable speed controller for the NREL 5 MW Baseline turbine. Near the rated speed the torque controller deviates from the expression in Eqn. 4.12 to limit the tip speed. The generator torque versus generator speed expression becomes linear with a very high slope. Indeed, if the generator torque control was identical then STAS Aeroelastic too would predict higher aerodynamic loads than seen here and the difference in flapwise deflections would be smaller. These residual differences in flapwise tip deflection are explained in the same ways as for

the lower wind speed case of 8 m/s. However as rotor speed increases the difference in centrifugal stiffening predicted by the two codes increases further. The blade flapwise deflection results predicted by the two models can thus be expected to be even more apart.

Despite the small differences which we have noted here, the predictions given by STAS Aeroelastic are in reasonable agreement with FAST. It demonstrates that the numerical integration scheme applied here works reasonably well while at the same time reinforcing the validity of the non-linear aeroelastic model in STAS Aeroelastic. This should form the basis of studies with more complex load cases where unsteady aerodynamic effects are encountered to further test the time marching tool developed here.

While the time marching tool maybe accurate, it is still far away from being computationally time efficient. The tool developed here takes roughly fifty minutes to run one second of simulation time. FAST on the other hand would take roughly two minutes for each second of simulation time when using the BeamDyn structural model for a similar level of modal reduction. This despite the fact that the time step used with the time marching tool in STAS ($5 \times 10^{-3} s$) is two times the time step used in FAST ($2 \times 10^{-3} s$). There is a possibility to apply modal reduction to the aerodynamic states and further increase the time step size. However, the difference in speed is mostly down to factors related to the coding environment and structure of the code. As mentioned earlier, the STAS Aeroelastic code structure is not optimized for time marching simulations. The code structure is inefficient and there exists a large-scale possibility to cut unnecessary function calls and parallelize iterative loops such that multiple processing cores can be utilized. Lastly, it is also to be taken into account that codes involving a large amount of data are likely to run much faster in a low-level programming language such as C/C++ than in Matlab [4].

6

Conclusions & Recommendations

In this thesis project a reduced-order aeroelastic model was developed using the STAS Aeroelastic module for application to condition monitoring and fault detection. The linearized aeroelastic model in STAS was first verified against FAST, subsequently reduced and then tested in a stability analysis study. A time marching simulation tool was developed wherein the modally reduced non-linear aeroelastic model was numerically integrated. This chapter summarizes the main conclusions from this report. This is followed by a critical evaluation of the current work seeking opportunities for improvements and possible recommendations.

6.1. Conclusion

A review of the state-of-the-art aeroelastic tools was done to bring forth their limitations. These limitations included the small deformations assumption, lack of framework for updating aerodynamic coordinate systems as structure deforms and non-inclusion of anisotropic material couplings in the beam models. The state-of-the-art aeroelastic module in STAS WPP (State Space Analysis of Wind Power Plants) which overcomes the aforementioned limitations was chosen to implement the order reduction strategies.

The accuracy of the linearized aeroelastic model in STAS was verified through various case studies on the NREL 5MW Baseline wind turbine. First the structural model was tested. The finite element beam model of the sub-structures was found to be accurate by verifying the body modes. The structural model assembly and constraint equations were tested through a modal analysis of the full system and it was concluded that frequencies of the full wind turbine modes match well against FAST. Furthermore the non-linear centrifugal stiffening effect was also verified to have been captured reasonably well in the linear structural model. The structural model was reduced in terms of the structural modes of the isolated sub-structures to achieve a reduced-order model. Beginning with 72 structural modes, it was concluded that the steady state deflections could be accurately represented by using only 29 structural modes for the complete wind turbine. This reduction of the model had no significant effect on the prediction of steady state deflections. Also, a case study was performed wherein the flutter limit of the NREL 5MW Baseline wind turbine was sought to be predicted. The predictions of the linear model were compared against results from Kallesøe's [38] work and it was found that the linear model predicted the flutter limit with high accuracy.

Furthermore, two approaches for developing a time marching integration tool based on different coupling and numerical integration schemes were proposed. The first involves time marching of the monolithic, strongly coupled non-linear aeroelastic model using a multistep predictor-corrector integration scheme. In the second approach, a partitioned, loosely coupled version of the linear aeroelastic model is implicitly integrated over time.

A time marching aeroelastic simulation tool based on the Adam-Bashforth-Moulton predictor-corrector method was implemented. This tool numerically integrates the modally reduced, monolithic non-linear aeroelastic

model in STAS. The time integration tool was verified for a limited number of simple power production test cases. It was found for these test cases that the predictions match reasonably well with FAST. It was possible to achieve a maximum time step size for numerical integration of the same order as used in FAST. However, the simulations were still very slow and still far away from running in real time as was envisaged for application to condition monitoring and fault detection.

6.2. Recommendations

Only the structural part of the aeroelastic model has been reduced in terms of modes. There is also a possibility to reduce the aerodynamic states in terms of some variation of the blade structural modes as proposed by [62]. This, however, is complicated as the accuracy of the model depends on choosing the right blade modes to represent the aerodynamic states. A greater understanding on how to select modes which can represent the aerodynamic states is certainly needed. This would also offer the possibility of further modal reduction of the aeroelastic model, and a further increase in time step size for explicit integration schemes.

The time marching tool developed here has been verified for simple power production cases. It needs to be verified for more complex operational conditions including turbulent inflow cases. Also, its application to condition monitoring needs to be demonstrated through case studies such as those based on pitch or yaw misalignment of the rotor. The time marching method based on partitioning of the aeroelastic system and then implicitly integrating the loosely coupled aeroelastic linear system needs to be further studied. It remains unclear if this method is inherently unstable or if there were implementation issues which lead to convergence problems as described in Chapter 5.

Finally, both the non-linear and linear codes in STAS Aeroelastic need major restructuring to make them more computationally efficient. This could also involve parallelization of iterative loops. It may also be useful in terms of computational speed, though extremely tedious, to re-work the STAS code in C++ and integrate with Matlab using a MEX-file. The MEX-file is a tool which allows users to take advantage of the graphical user interface of Matlab while still coding in a low-level programming language such as C/C++ [4].

Bibliography

- [1] *Unsteady wake effects caused by pitch-angle changes.*, 1986.
- [2] M.B. Ageze, Y. Hu, and H. Wu. Wind Turbine Aeroelastic Modeling: Basics and Cutting Edge Trends. *International Journal of Aerospace Engineering*, 2017, 2017. ISSN 1687-5974. doi: 10.1155/2017/5263897.
- [3] J.D. Anderson Jr. *Fundamentals of Aerodynamics*. McGraw-Hill, 3 edition, jul . ISBN 0-07-237335-0. doi: 10.1371/journal.pcbi.1000716. URL <http://www.ncbi.nlm.nih.gov/pubmed/166738><http://www.pubmedcentral.nih.gov/articlerender.fcgi?artid=PMC1277458>.
- [4] T. Andrews. Computation Time Comparison Between Matlab and C++ Using Launch Windows. *Aerospace Engineering*, pages 1–6, 2012.
- [5] K.J. Astrom and R.M. Murray. *Feedbaack systems : an introduction for scientists and engineers*. Princeton University Press, v2.11b edition, 2012. ISBN 9780198722595.
- [6] G. Bir. Multi-Blade Coordinate Transformation and its Application to Wind Turbine Analysis. *46th AIAA Aerospace Sciences Meeting and Exhibit*, pages 1–15, 2008. ISSN 0114-5916. doi: 10.2514/6.2008-1300.
- [7] G. Bir and J. Jonkman. Aeroelastic instabilities of large offshore and onshore wind turbines. *Journal of Physics: Conference Series*, 75(1), 2007. ISSN 1742-6596. doi: 10.1088/1742-6596/75/1/012069.
- [8] M.L. Buhl Jr. A New Empirical Relationship between Thrust Coefficient and Induction Factor for the Turbulent Windmill State. Technical report, 2005.
- [9] M.L. Buhl Jr. and A. Manjock. A Comparison of Wind Turbine Aeroelastic Codes Used for Certification-Conference Paper NREL/CP-500-39113 January 2006. *AIAA Aerospace Sciences*, pages 1–17, 2006. URL <papers2://publication/uuid/64E86FCD-EF97-4CE3-A0F1-8F97E65D0C2F>.
- [10] T. Burton, N. Jenkins, D. Sharpe, and E. Bossanyi. *Wind Energy Handbook*. John Wiley & Sons, Ltd, Chichester, UK, may 2011. ISBN 9781119992714. doi: 10.1002/9781119992714.
- [11] E. Cheever. State Space Representations of Linear Physical Systems. URL <http://lpsa.swarthmore.edu/Representations/SysRepSS.html>.
- [12] Wikipedia Contributors. Lagrangian mechanics, 2019. URL https://en.wikipedia.org/wiki/Lagrangian_mechanics.
- [13] D. Coronado and K. Fischer. Condition Monitoring of Wind Turbines: State of the Art, User Experience and Recommendations. Technical report, 2015.
- [14] P. Cross and X. Ma. Model-based and fuzzy logic approaches to condition monitoring of operational wind turbines. *International Journal of Automation and Computing*, 12(1):25–34, 2015. ISSN 1751-8520. doi: 10.1007/s11633-014-0863-9.
- [15] N. Dantam. Quaternion Computation. Technical report, Atlanta, 2014.
- [16] Edda Eich-Soellner and Claus Führer. *Numerical Methods in Multibody Dynamics*. B.G. Teubner Stuttgart, 1998. ISBN 3-519-02601-5.
- [17] C.A. Felippa and B. Haugen. A unified formulation of small-strain corotational finite elements: I. Theory. *Computer Methods in Applied Mechanics and Engineering*, 194(21-24 SPEC. ISS.):2285–2335, 2005. ISSN 0045-7825. doi: 10.1016/j.cma.2004.07.035.

- [18] Flow-3D. Implicit vs. Explicit Numerical Methods. URL <https://www.flow3d.com/resources/cfd-101/numerical-issues/implicit-versus-explicit-numerical-methods/>.
- [19] D. Fransos and L. Bruno. Determination of the aeroelastic transfer functions for streamlined bodies by means of a Navier-Stokes solver. *Mathematical and Computer Modelling*, 43(5-6):506–529, 2006. ISSN 0895-7177. doi: 10.1016/j.mcm.2005.10.002.
- [20] Y.C. Fung. *An Introduction to the Theory of Aeroelasticity*. John Wiley & Sons, Ltd, 1955.
- [21] G. Gallego and A. Yezzi. A Compact Formula for the Derivative of a 3-D Rotation in Exponential Coordinates. *Journal of Mathematical Imaging and Vision*, 51(3):378–384, 2015. ISSN 0924-9907. doi: 10.1007/s10851-014-0528-x.
- [22] F.P. García Márquez, A.M. Tobias, J.M. Pinar Pérez, and M. Papaalias. Condition monitoring of wind turbines: Techniques and methods. *Renewable Energy*, 46:169–178, 2012. ISSN 0960-1481. doi: 10.1016/j.renene.2012.03.003.
- [23] A. Gasmi, M.A. Sprague, J.M. Jonkman, and W.B. Jones. Numerical Stability and Accuracy of Temporally Coupled Multi-Physics Modules in Wind-Turbine CAE Tools. In *51st AIAA Aerospace Sciences Meeting*, pages 1–16.
- [24] E.S. Grassia. Practical Parameterization of Rotations Using the Exponential Map. *The Journal of Graphics Tools*, 3.3:1–13, 1998. ISSN 1086-7651. doi: 10.1007/s00442-009-1277-1.
- [25] GWEC. GWEC produces graphs showing the exciting growth of the wind power industry around the world. URL <http://gwec.net/global-figures/graphs/>.
- [26] M.H. Hansen. Aeroelastic stability analysis of wind turbines using an eigenvalue approach. *Wind Energy*, 7(2):133–143, 2004. ISSN 1095-4244. doi: 10.1002/we.116.
- [27] M.O.L. Hansen. Aeroelastic properties of backward swept blades. *49th AIAA Aerospace Sciences Meeting including the New Horizons Forum and Aerospace Exposition*, pages 1–19, 2011. doi: 10.2514/6.2011-260.
- [28] M.O.L. Hansen. *Aerodynamics of Wind turbines*. Earthscan, 2 edition, 2017. ISBN 9781844074389.
- [29] M.O.L. Hansen, J.N. Sørensen, S. Voutsinas, N. Sørensen, and H.A. Madsen. State of the art in wind turbine aerodynamics and aeroelasticity. *Progress in Aerospace Sciences*, 42(4):285–330, 2006. ISSN 0376-0421. doi: 10.1016/j.paerosci.2006.10.002.
- [30] Holierhoek, J.G. *Lecture notes in wind turbine aeroelasticity*. Delft University of Technology, 2017.
- [31] D. How. *Lecture 7: Lagrange's Equations*. Massachusetts Institute of Technology, 2003.
- [32] S.J. Hulshoff. Aeroelasticity. Technical Report November, 2011.
- [33] L. Jespersen and M.W. Krogen. *Model Predictive LIDAR Control of Wind Turbines for Load Mitigation*. PhD thesis, Aalborg University, 2011.
- [34] J. Jonkman, S. Butterfield, W. Musial, and G. Scott. Definition of a 5-MW Reference Wind Turbine for Offshore System Development. Technical report, 2009. URL <http://www.osti.gov/servlets/purl/947422-nhrlni/>.
- [35] J.M. Jonkman and M.L. Buhl Jr. FAST User's Guide - Updated August 2005. Technical report, Golden, CO, oct 2005. URL <http://www.osti.gov/servlets/purl/15020796-vtWx3/>.
- [36] J.M. Jonkman, G.J. Hayman, B.J. Jonkman, and R.R. Damiani. AeroDyn v15 User's Guide and Theory Manual. Technical report, 2015.
- [37] M. Ø Jørgensen, A. Overgaard, and H. Steffensen. *Inclusion of Dynamic Inflow in Model Predictive Control of Wind Turbines*. PhD thesis, Aalborg University, 2014.
- [38] B.S. Kallestøe and M.H. Hansen. Effects of Large Bending Deflection on Blade Flutter Limits, Upwind deliverable D2.3. 2008.

- [39] B.S. Kallesøe and K.A. Kragh. Field Validation of the Stability Limit of a Multi MW Turbine. *Journal of Physics: Conference Series* 753, 2016. doi: 10.1088/1742-6596/753/4/042005.
- [40] J. Katz and A. Plotkin. *Low speed aerodynamics*. Cambridge University Press, 13 edition, 2001.
- [41] J.G. Leishman and K.Q. Nguyen. State-space representation of unsteady airfoil behavior. *AIAA Journal*, 28(5):836–844, 1990. ISSN 0001-1452. doi: 10.2514/3.25127.
- [42] C. Lindenburg. BLADMODE : Program for Rotor Blade Mode Analysis. Technical Report July, 2003.
- [43] C. Lindenburg. PHATAS Release "NOV-2003" and "APR-2005" USER'S MANUAL : Program for Horizontal Axis wind Turbine Analysis and Simulation. Technical Report May, 2005.
- [44] H.A. Madsen and V.A. Riziotis. Aeroelasticity and structural dynamics of wind turbines. In *Wind energy systems: Optimising design and construction for safe and reliable operation*, pages 46–111. Woodhead Publishing Limited, 2010.
- [45] K.O. Merz. *Conceptual Design of a Stall-Regulated Rotor for a Deepwater Offshore Wind Turbine*. PhD thesis, NTNU, 2011.
- [46] K.O. Merz. A Linear State-Space Model of an Offshore Wind Turbine, Implemented in the STAS Wind Power Plant Analysis Program. Technical Report TR A7474, 2015.
- [47] K.O. Merz. Enhanced finite beam elements for wind turbine blades. Technical Report 1, 2016.
- [48] K.O. Merz. STAS Aeroelastic 1.0 – Theory Manual. Technical report, 2018.
- [49] D.P. Molenaar. *Cost-effective design and operation of variable speed wind turbines*. PhD thesis, 2003. URL <http://www.narcis.nl/publication/RecordID/oai:tudelft.nl:uuid:f1d1bec2-1064-4ab6-87b4-fc78779d6404>.
- [50] B. Morton. Understanding Wind Turbine Condition Monitoring Systems. Technical report. URL <http://www.renewablenrgsystems.com/>.
- [51] A. Ning, G. Hayman, R. Damiani, and J.M. Jonkman. Development and Validation of a New Blade Element Momentum Skewed-Wake Model within AeroDyn. *33rd Wind Energy Symposium*, (December 2014), 2015. doi: 10.2514/6.2015-0215.
- [52] ode15i. MATLAB Documentation : ode15i. URL https://nl.mathworks.com/help/matlab/ref/ode15i.html?searchHighlight=ode15i&s{_}tid=doc{_}srchttitle{#}References.
- [53] ode45. MATLAB Documentation : ode45. URL <https://nl.mathworks.com/help/matlab/ref/ode45.html>.
- [54] OpenFast. OpenFAST Documentation. URL <https://openfast.readthedocs.io/en/master/>.
- [55] S. Øye. Dynamic stall simulated as time lag of separation. In *Proceedings of the 4th IEA Symposium on the Aerodynamics of Wind Turbines*, Rome, 1991.
- [56] S.R.J. Powles. The effects of tower shadow on the dynamics of a horizontal-axis wind turbine. *Wind Engineering*, pages 26–42, 1983.
- [57] F. Rasmussen, M.H. Hansen, K. Thomsen, T.J. Larsen, F. Bertagnolio, J. Johansen, H.A. Madsen, C. Bak, and A.M. Hansen. Present status of aeroelasticity of wind turbines. *Wind Energy*, 6(3):213–228, 2003. ISSN 1095-4244. doi: 10.1002/we.98.
- [58] Shabana, A.A. *Dynamics of Multibody Systems*. Cambridge University Press, 3rd edition.
- [59] H. Snel and J.G. Schepers. Engineering Models for Dynamic Inflow Phenomena. In *EWEC*, number October, pages 14–18, Amsterdam, 1991.
- [60] H. Snel and J.G. Schepers. Investigation and modelling of dynamic inflow effects. In *ECWEC '93 Conference*, 1993. URL <ftp://ftp.ecn.nl/pub/www/library/report/1993/rx93029.pdf> {%}0Aftp://question.ecn.nl/pub/www/library/report/1993/rx93029.pdf {%}5Cnpapers3://publication/uuid/B431F9AD-74D4-44AE-B87B-F5BD750673FF.

-
- [61] H. Snell. Heuristic modelling of dynamic stall characteristics. *EWEC-Conference- Bookshop for Scientific Publications*, 1997.
- [62] I.B. Sønderby. Low-order aeroelastic models of wind turbines for controller design. 2013.
- [63] P.J. Tavner, F. Spinato, G.J.W. van Bussel, and E Koutoulakos. Reliability of Different Wind Turbine Concepts with Relevance to Offshore Application. In *European Wind Energy Conference*, number April, Brussels, 2008. ISBN 9781615671151.
- [64] S.R. Vatne. *Aeroelastic Instability and Flutter for a 10 MW Wind Turbine*. PhD thesis, Norwegian University of Science and Technology, 2011.
- [65] A. Viré. Lecture notes on "Dynamics of wind turbines". Technical report, 2016.
- [66] WMC. FOCUS6 - The integrated wind turbine design suite. Technical report, 2014.
- [67] J.T. Young. Primer on the Craig-Bampton Method. Technical report, 2000.